Probing the Electronic and Magnetic Properties of Transparent Semiconductor Nanowires using X-ray Absorption Spectroscopic Methods

by

Manu Hegde

A thesis
presented to the University of Waterloo
in fulfillment of the
thesis requirement for the degree of
Doctor of Philosophy
in
Chemistry

Waterloo, Ontario, Canada, 2015

AUTHOR'S DECLARATION

I hereby declare that I am the sole author of this thesis. This is a true copy of the thesis, including any required final revisions, as accepted by my examiners.

I understand that my thesis may be made electronically available to the public.

Statement of Contributions

My doctoral work was carried out under the guidance of Dr. Pavle V. Radovanovic. My research is extensively focused on X-ray absorption spectroscopy measurements and simulation of experimental data in semiconductor nanowires. These nanowires were synthesized and characterized by my co-workers Dr. Ian D. Hosein and Dr. Shokouh S. Farvid. The magneto-transport studies were performed in collaboration with Dr. Jonathan Baugh of Institute of Quantum Computation, University of Waterloo. The mathematical model to understand the photoluminescence decay dynamics in gallium oxide nanocrystals was developed in collaboration with Dr. Zoran L. Miscovic of Appied Mathematics, University of Waterloo.

The work presented in Chapters 3 and 4 involve $Ga_{1-x}Mn_xN$ nanowire synthesis, characterization and X-ray absorption spectroscopic measurements. I have performed manganese L-edge X-ray absorption and X-ray magnetic circular dichroism experiments using scanning transmission X-ray microscopy, followed by data analysis, multiplet calculations, sum rule analysis and interpretation of results. Synthesis, structural characterization Chapter 3 and manganese K-edge analysis of the nanowires in Appendix E was performed by Dr. Shokouh S. Farvid.

The work presented in Chapter 5 involve gallium oxide nanowire growth, morphology evolution and understanding the origin of orbital anisotropy. Nanowire synthesis, morphology evolution and transmission electron microscopy analysis was performed by Dr. Ian D. Hosein. I have performed X-ray absorption spectroscopy spectroscopy measurements using linearly polarized X-rays, followed by data analysis, calculations of oxygen K-edge using FDMNES code and data interpretation.

All the results presented in Chapters 3 to 5, which involve my direct contribution and published in various journals and conference proceedings. In addition, I have also involved partially/fully to the following work which involve, X-ray measurements, simulations and mathematical modeling. These results were published in various journals and shown in Appendix from I to M.

Abstract

Control of electron spins in individual magnetically doped semiconductor nanostructures has considerable potential for quantum information processing and storage. The manipulations of dilute magnetic interactions have largely been restricted to low temperatures, limiting their potential technological applications. Among the systems predicted to be ferromagnetic above room temperature, Mn-doped GaN has attracted particular attention, due to its attractive optical and electrical properties. However, the experimental data have been inconsistent, and the origin of the magnetic interactions remains unclear. Furthermore, there has been no demonstration of tuning the dopant exchange interactions within a single nanostructure, which is necessary for the design of nanoscale spin-electronic (spintronic) devices.

This work demonstrates for the first time intrinsic magnetization of manganese dopants in individual gallium nitride nanowires (NWs) at room temperature, which were synthesised using the chemical vapor deposition method. The results of single nanowire XANES studies using scanning transmission X-ray microscopy along with atomic multiplet calculations confirm that Mn adopts tetrahedral coordination in GaN nanowires and has mixed oxidation state (Mn^{2+}/Mn^{3+}), with Mn^{2+} being in relative majority. Using high-resolution circularly polarized X-ray microscopy imaging, the dependence of the manganese exchange interactions on the NW orientation with respect to the external magnetic field was studied. This study also focused on the importance of X-ray studies on individual nanowires, as in ensemble measurements contribution come from the co-deposition of Mn secondary phases alongside nanowires. This was further confirmed by bulk magnetization measurements, which has shown only residual magnetization. Single nanowire X-ray magnetic circular dichroism indicates intrinsic magnetic ordering of Mn dopants at 300 K. The crystalline anisotropy allows for the control of dilute magnetization in a single NW and the application of bottom-up approaches, such as *in situ* nanowire growth control or targeted positioning of individual NWs, for the design of energy efficient spin-electronic devices.

The second part of the thesis focuses on the growth mechanism and origin of orbital anisotropy in β-Ga_2O_3 nanowires. Gallium oxide nanostructures with high aspect ratio and variable faceting were synthesized by the chemical vapor deposition method via vaporsolid growth mechanism. Systematic investigation of the growth conditions revealed that the nanowires can be produced under the conditions of high temperature and low precursor flow. The nanowires crystalize as the β-phase Ga_2O_3, which has the monoclinic crystal structure. Preferred growth was along the [010] direction, as corroborated with lattice-resolved imaging and crystal plane models. The high degree of faceting is discussed in terms of the evolution

of the nanowire cross-section morphology, based on the growth rate of the facet boundaries relative to the nanowire surface planes.

The origin of anisotropy at the molecular and electronic structure levels in individual β-Ga_2O_3 nanowires grown along the crystallographic b direction was studied using linearly polarized X-ray absorption imaging at both gallium L_3 and oxygen K edges. The O K-edge spectrum shows significant linear dichroism for the electric field vector of the X-rays oriented parallel and perpendicular to the nanowire long axis. The contributions from the three nonequivalent oxygen sites to the observed spectral anisotropy were elucidated using FDMNES calculations in the framework of the multiple scattering theory. The role of relevant O and Ga orbitals in the linearly polarized O K-edge absorption was determined based on the point group symmetry arguments. The results of this work suggest mixed covalent and ionic character of the Ga-O bond in individual nanowires, with the dominant contribution of O $2p_z$ orbitals to the absorption spectrum for the electric field vector oriented perpendicular, and O $2p_{x,y}$ orbitals for the electric field vector oriented parallel to the nanowire long axis. Gallium $4p$ and d orbitals were found to contribute mostly to the antibonding states. These results improve the understanding of the origin of anisotropy in complex transparent metal oxide nanostructures, and could lead to the prediction of physical properties for different nanowire growth directions.

The understanding of growth mechanism, dopant distribution and electronic origin of crystalline anisotropy within individual semiconductor nanowires is of fundamental importance. It is these structural parameters can dramatically change electronic, magnetic, and optoelectronic properties of the nanowires, and could be building blocks for the future nanodevices.

Acknowledgements

First, I thank my supervisor Dr. Pavle V. Radovanovic for providing me an opportunity to pursue a doctoral degree under his guidance. His passion towards science and emphasis on independent thinking in solving research problems always motivated me to become a better researcher during past few years.

I thank my committee members, Dr. Jonathan Baugh, Dr. Eric Prouzet, and Dr. Daniel Thomas (University of Guelph), for their time and valuable feedback on my research during past few years. I am grateful to Dr. Zoran Miskovic for a very fruitful collaboration and guidance in developing DAP modeling. I am thankful to Dr. Jalil Assoud for his patience and time to have useful discussions on several aspects of crystallography and inorganic chemistry. I had an opportunity to do teaching assistantships with Howard, Jake, and Sue during my PhD, and I learnt many basic aspects of chemistry from them.

This thesis would not have been possible unless I mention Dr. Jian Wang at the Canadian Light Source. His technical skills on operating STXM machine always helped me to obtain good quality data. Again, I must acknowledge him for teaching basics of Axis-2000 data analysis software. I also thank other beam line scientists, Dr. James Dynes, Dr. Ning Chen, and Dr. Tom Regier, at various beamlines for their assistance in taking measurements, and valuable discussions in understanding XAS concepts. I also acknowledge Canadian Light Source for their graduate student travel support award. I thank Dr. Carmen Andrei for her assistance in TEM measurements at CCEM.

I thank all of the present and past group members for their assistance in the lab. In particular, Dr. Ian D. Hosien for his guidance and positive approach towards solving difficult research problems at the early stages of my work were invaluable. I am truly thankful to Vadim, Lisa, Vahid, Terry and Natalie for their tremendous support and enthusiasm.

I thank my friends Dr. Kalikinkar Mandal and Dr. Andree Susanto for introducing me to Linux operating system and later I found it is really useful for some of my theoretical calculations. I thank my friend Dr. Puneet Sharma for his useful and resourceful advice whenever I am in trouble. I would like to mention some of my friends Avisek, Pradeep, Hiren, Somit, Gaurav, Mike, and Shivang, who made my stay at Waterloo more enjoyable.

And last but not least, I thank my parents for their continues support and encouragement. Finally, I thank my wife Divya for her love and care.

Dedication

This thesis is dedicated to my parents Yashoda and Ramchandra Hegde for their blessings and constant support.

Table of Contents

List of Tables

List of Figures

List of Abbreviations

CLS	Canadian Light Source Inc.
CVD	Chemical vapor deposition
DMSs	Diluted magnetic semiconductors
DFT	Density functional theory
DOS	Density of states
EDS	Energy dispersive X-ray spectroscopy
GMR	Gaint magneto resistance
$\mathbf{Ga_{1-x}Mn_xN}$	Manganese doped gallium nitride
HAADF	High-angle annular dark field
LCP	Left circularly polarized light
MRAM	Magnetoresistive random-access memory
MT	Muffin tin
MS	Multiple scattering
NWs	Nanowires
PDOS	Projected density of states
PPMS	Physical properties measurement system
RKKY	Ruderman-Kittel-Kasuya-Yosida
RCP	Right circularly polarized light
SFET	Spin-field effect transistor
SEM	Scanning electron microscopy
STEM	Scanning transmission electron microscopy

STXM	Scanning transmission X-ray microscopy
TEM	Transmission electron microscopy
TM	Transition metal
TMOs	Transparent metal oxides
VLS	Vapor-liquid-solid
VS	Vapor-solid
XRD	X-ray diffraction
XAS	X-ray absorption spectroscopy
XANES	X-ray absorption near edge structure
XMCD	X-ray magnetic circular dichroism

Chapter 1

Introduction*

1.1 Basic Principles and Applications of Spintronics

The interlinking of electron spin with its charge degrees of freedom is the basis for spintronics. The addition of electron spin to the traditional charge based semiconductor can drastically increase the device performance in terms of processing speeds, non-volatile electronics and lower electrical power consumption. The concept of electron spin explained through quantum mechanics, and the studies involving the spin interaction between particles and its solid-state environment are essential to develop novel spintronic devices.[1–4]

Both experimentalists and theoreticians are intensively addressing the following major challenges in the field of spintronics: (i) Effective way of aligning or polarizing a spin system

*This thesis is written based on following four papers:

at room temperature; (ii) achieving longer spin life-time in a particular logic state; (iii) effective transport and detection of spin state in a solid-state environment.[1] Traditionally, spin polarization can be achieved by optical techniques in which circularly polarized light can couple with the spin of an electron, however for devices, electrical spin injection is required. The electrical spin injection, transport and detection could be made possible by connecting a magnetic electrode to the sample. Moreover, recent experimental results confirm that a longer coherence time can be achieved by integrating nuclear spin with electron spin.[5]

1.2 Spin Based Devices

Research and development in the field of spintronics rapidly increased with the discovery of giant magnetoresistance (GMR) in 1988.[6,7] GMR was observed in thin film structures consisting of alternate conductive ferromagnetic and nonmagnetic layers. The electrical resistance of the layered structure was low when magnetic moments of the ferromagnetic films were aligned in parallel and maximum when they were antiparallel. The direction of magnetization was controlled by applying an external magnetic field. The GMR effect has important applications in magnetic field sensors, read heads for hard discs, galvanic insulators, and magnetoresistive random-access memory (MRAM).

A GMR based MRAM is shown in Figure 1.1. MRAM is made up of pillars of magnetic layers, in which each pillar consists of two magnetic layers separated by a non-magnetic layer. If the magnetic layers align ferromagnetically, then information is stored as binary code 1; information is stored as 0 if they are aligned antiferromagnetically. The information stored (0 or 1) is read by measuring the resulting current, the resistance from any particular pillar, and this gives the magnetization polarity of the writable pillar. If the pillars have the same polarity, this results in lower resistance (1), and higher resistance (0) if they have opposite polarity. The information is written by changing the coupling between two magnetic layers within a given pillar, either parallel or antiparallel or vice versa, and coupling can be interchanged by generating an Oersted field when current flows through the leads connecting each pillar.

A second example of a prototype spintronic device is the Datta-Das spin-field effect transistor (SFET) (Figure 1.2).[9] SFET has a similar structure to a conventional field effect

[‡]Reprinted with permission from (K. Sato, L. Bergqvist, J. Kudrnovský, P. H. Dederichs, O. Eriksson, I. Turek, B. Sanyal, G. Bouzerar, H. Katayama−Yoshida, V. A. Dinh, T. Fukushima, H. Kizaki and R. Zeller, Rev. Mod. Phys., 2010, 82, 1633; http://dx.doi.org/10.1103/RevModPhys.82.1633). Copyright (2010) by the American Physical Society.

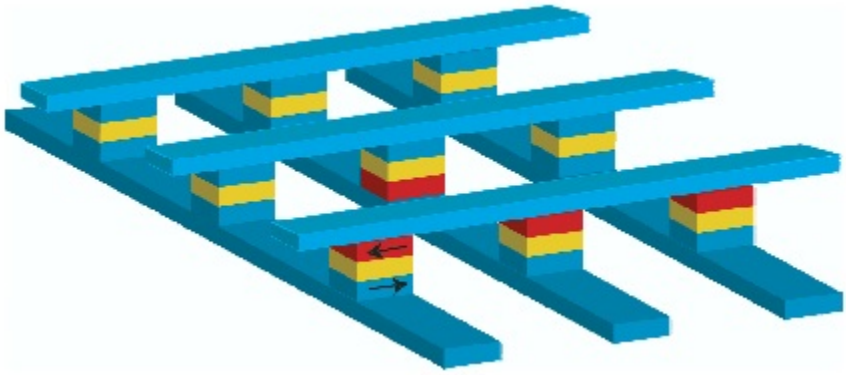

Figure 1.1: Schematic of a magnetoresistive random-access memory (MRAM) device. Each pillar consist of two magnetic layers separated by a nonmagnetic layer. MRAM utilizes hysteresis (due to ferromagnetic coupling between the layers) to store data and magnetoresistance to read data.[8‡]

transistor (FET) with a source, drain, narrow channel and gate to control the current. The function of a gate is to allow the flow of current (acts like a switch), while the narrow channel controls the flow of charge current. The difference is controlling the current by utilizing the spin degree of freedom. In Datta-Das SFET, the source acts as a spin injector and the drain detects the electron spin and both are made up of ferromagnetic elements. The electrons will be transported ballistically through the narrow channel and will be detected by drain. If the spin direction of the arriving electron is the same as the drain spin, the device will be in the ON state. If it is aligned in the opposite direction as that of the drain spin, then the device will be in the OFF state. The function of the gate is to generate an effective magnetic field and originates from the spin-orbit coupling in the substrate material. The strength of the magnetic field depends on the confinement geometry of the current channel and the electrostatic potential of the gate. The electron spin will precess due to the presence of an effective magnetic field and by modifying the voltage one can manipulate the precession, whether it is aligned parallel or antiparallel to the drain spin.

The Datta-Das SFET has been realized theoretically in metal-semiconductor interface, where ferromagnetic metal acts as a spin injector and align the spin of non-magnetic semiconductor. However, the conductivity mismatch at the metal-semiconductor makes this configuration is complex, and the spin transport across the interface is not well understood. In order to avoid conductivity mismatch, magnetic semiconductors have been used as spin injectors but it worked at low temperature. Due to all these difficulties Datta-Das SFET

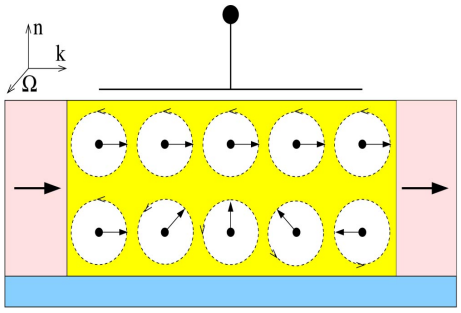

Figure 1.2: Schematic of Datta-Das spin-field effect transistor (SFET), where **k** is the wave vector of the electron injected from the source and will travel ballistically in a plane normal (**n**) to the narrow channel. The Ω is the electron precession vector due to the spin-orbit coupling. The magnitude of Ω can be controlled by the gate voltage from the top of the channel. Depending on the orientation of the incoming electron at the drain, the change in the current is observed.[1]¶

not yet been realized experimentally.[10]

The semiconducting microprocessors, which are used for information technology, operate in the following two steps: (a) The logic operations and information processing are performed using the electronic charge; (b) information is stored in the magnetic hard disc made up of ferromagnetic elements (spin degrees of freedom). Hence, there is no synergy between magnetism and semiconducting properties. Therefore, there is a need for novel multifunctional materials which can operate at room temperature by making use of both logic and storage operations on a single chip.[11] During the past several years, the scientific community has been actively seeking semiconductors which show room temperature ferromagnetism. Such materials are known as diluted magnetic semiconductors (DMSs), and they can retain both conductivity and ferromagnetism at room temperature, which are essential for many practical applications.[11]

1.3 Diluted Magnetic Semiconductors

Diluted magnetic semiconductors have small portions of cations of the non-magnetic semiconductors replaced by magnetic ions of the *d*-block transition metal (TM) elements.

¶Reprinted with permission from (Igor Žutić, Jaroslav Fabian and S. Das Sarma, Rev. Mod. Phys., 2004, 76, 323; http://dx.doi.org/10.1103/RevModPhys.76.323). Copyright (2004) by the American Physical Society.

The localized magnetic moment of d-electrons is expected to influence the s or p electrons of the host lattice, making them ferromagnetic semiconductors. Such a manipulation of magnetic properties of the existing semiconductor electronics leads to the development of the emerging field of magnetoelectric devices and technology.

In order to utilize DMS materials for technological applications, they have to exhibit ferromagnetic ordering at the critical temperature, i.e., Curie temperature (T_C) above room temperature. The TM doped II-VI compounds such as $Cd_{1-x}Mn_xTe$ were the most widely studied DMSs during the early stages of this field. The most widely used III-V semiconductors (such as InAs and GaAs) for high speed electronic and optoelectronic industry have shown significant increase in T_C ($\sim$30-150 K) when doped with 5% Mn.[12,13] The observed high T_C in $Ga_{1-x}Mn_xAs$ is due to the the long range coupling between Mn atoms mediated by holes in the valence band. This discovery of carrier-mediated ferromagnetism in $Ga_{1-x}Mn_xAs$ laid down the foundation for semiconductor spintronics. However, T_C for observed ferromagnetism in epilayers of $Ga_{1-x}Mn_xAs$ is still low (185 K) for practical applications.

In 2000, Dietl *et al.*[14] came up with a simple theoretical model to calculate T_C in DMSs and predicted room temperature ferromagnetism in wide-band gap semiconductors such as GaN and ZnO doped with a few percent of manganese. In support of the theory, there are several experimental results demonstrating high T_C in wide band gap materials. Sonada *et al.*[15] reported high Curie temperature ($T_C = 940$ K) ferromagnetism in GaN with less than 10% Mn doping concentration, which were grown using a molecular beam epitaxy method on a [001] oriented sapphire substrate. Similarly, Ueda *et al.*[16] observed high temperature ferromagnetism in cobalt (Co) doped ZnO thin films, which were grown using a pulsed laser deposition technique. In the search for high T_C ferromagnetic semiconductors, studies have been extended to wide band gap insulators such as TiO_2, which has shown room temperature ferromagnetism when doped with 1-8% Co.[17] Surprisingly, another insulating oxide HfO_2 has shown intrinsic ferromagnetism without doping any transition metal elements.[18]

1.4 Semiconducting Group-V Nitrides

The wide band gap semiconductor nitrides such as InN, GaN, and AlN have significant applications in optoelectronics such as, blue\green\UV light-emitting diodes,[19] laser diodes,[20] solar-bind UV detectors,[21] and high temperature electronics.[22] Attempts have been made to grow group-III nitrides on various substrates, including sapphire, SiC, Si and various oxides. Electron microscopy measurements confirmed high density of dislocations in thin films of nitrides, which tend to result in high leakage current in devices.[23] Despite these

limitations, nitrides can be utilized for high density data storage systems, visible displays, and in white light-emitting applications (combination of red, green, and blue output or by exciting the appropriate phosphor with blue GaN light-emitting diodes).[23]

Among different nitrides, GaN has shown high hole concentration when doped with 5% Mg, and at room temperature the hole concentration is typically $10^{17}\,\mathrm{cm}^{-3}$.[23] The hole concentration in DMS can be increased by codoping acceptors, which can reduce the self compensation effect.[24] C-doped AlN could be a p-type, but it has an ionization energy of $\sim$500 meV,[25] and therefore is not a suitable material for practical applications. InN is an n-type semiconductor, as it contains native anion defects. There are no reports on p-type doping in InN.[23]

Room temperature ferromagnetism in $Ga_{1-x}Mn_xN$ is carrier induced[14] and the ability to make GaN p-type renders this lattice a good candidate for achieving p-type meditated dilute ferromagnetism at room temperature in III-V semiconductors. However, the type mechanism of magnetic ordering in DMSs is still a matter of discussion. Even today there is no universal theory that can describe possible origins of magnetic ordering in DMSs. Hence, better understanding of underlying mechanisms of magnetic ordering will assist in designing materials for next generation spin-based devices. The next section will review various exchange interactions in magnetic semiconductors.

1.5 Exchange Mechanisms in Magnetic Semiconductors

Direct exchange. The direct exchange mechanism is due to coupling between the spins of highly localized electrons in solids. It is often called Heisenberg direct exchange, because this approach assumes that a single $3d$ electron is localized on each atom and each pair of atoms is treated as a simple hydrogen molecule. The interaction takes place between neighbouring $3d$ electrons and the type of interaction is described by the exchange integral parameter (see Appendix A for details). If the sign of the integral is positive favours the parallel coupling between the electron spin, leading to ferromagnetism. They exhibit antiferromagnetism if the sign of the integral is negative (electron spins of the neighbouring atoms are antiparallel). The strength of the direct exchange interaction falls off drastically with distance between the neighbours.[26]

Superexchange. Magnetic exchange interactions between localized $3d$ electrons of the transition metal ions are mediated by nonmagnetic anions with completely filled electronic shells. The superexchange mechanism is generally antiferromagnetic. It can be explained

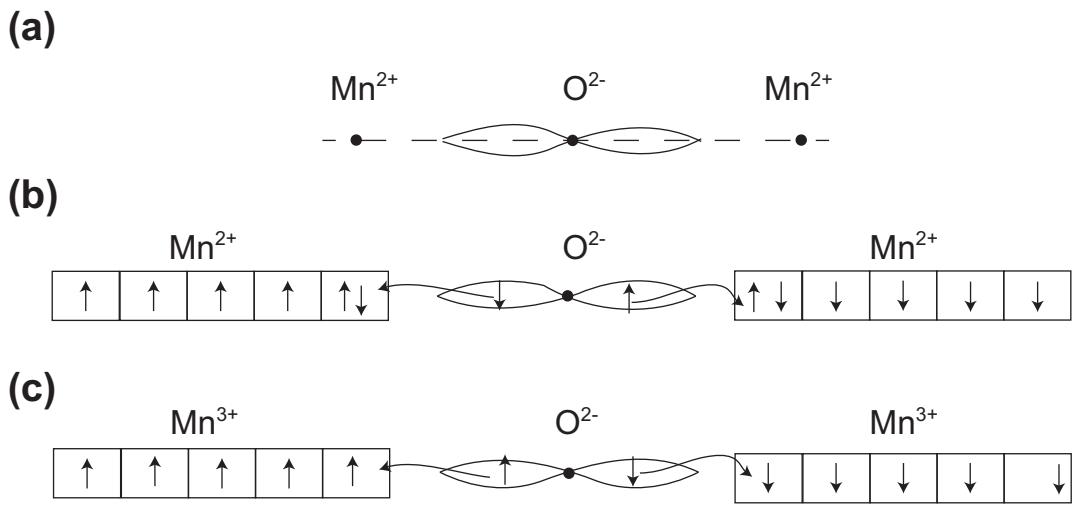

Figure 1.3: Schematics of the superexchange mechanism. (a) Linear chain arrangement Mn-O-Mn atoms in rock salt crystal structure of MnO. (b) Superexchange mechanism in MnO by forming the covalent bond between Mn^{2+} and O^{2-} ions. (c) Superexchange between two empty Mn $3d$ orbitals, leading to antiferromagnetic coupling of the Mn magnetic moments.

by considering the example of MnO. The MnO has a rock salt crystal structure (bonding is largely ionic), and linear chains of Mn^{2+} and O^{2-} running through the crystal structure. The $2p$ orbital of O^{2-} is completely occupied along each chain direction and oriented along the Mn-O-Mn axis (Figure 1.3a). The Mn^{2+} has five $3d$ electrons and follows Hund's rule to occupy the $3d$ orbitals. As the $2p$ orbitals of oxygen are completely filled, they can donate electrons to the partially filed 3d electrons of the Mn^{2+} ion ($2p$-$3d$ hybridization). By making an assumption that the left-most Mn orbitals has all spin-up electrons, as shown in Figure 1.3b, covalent bonding can occur between Mn^{2+} and O^{2-} ions, if the electron of the neighbouring oxygen atom is spin-down. This leaves only a spin-up electron in the oxygen $2p$ orbital, and it can donate it to the next Mn^{2+} orbitals with spin-down configuration. This oxygen-mediated exchange interaction results in overall antiferromagnetic coupling between the Mn^{2+} ions.[27]

The exchange interaction between the empty $3d$ states mediated by completely filled O p orbitals also leads to antiferromagnetism. In this case, the electron density of ligands (oxygen) overlap with the partially filled $3d$ orbitals. According to Hund's rule, the spin of the donated electron from the ligand and the metal atom should be the same spin (Figure 1.3c).[26]

Indirect exchange. The direct exchange interaction between the magnetic ions will

induce the spin polarization of conduction electrons in its vicinity, which in turn align the magnetic moments of other magnetic ions within range, leading to an indirect coupling (this is also called Ruderman-Kittel-Kasuya-Yosida (RKKY) interaction).[28]

Zener's double exchange model. It is essentially a modified form of superexchange interactions, the difference being that electrons actually move between the cation sites via intermediate ligands. In order to maximise the probability of hopping electrons in outer shells of both ions, they must have the same spin. Then, the wave function of the hopping electron extends in space between the two ions and dominates the direct superexchange interaction between d electrons of magnetic ions. As a consequence, kinetic energy of the system is reduced and enhances ferromagnetic interactions. Essentially, it depends on p-d orbital hybridization, which increases from antimonides to nitrides. Therefore, it was successful in explaining the origin of ferromagnetism in wide band gap semiconductors such as TM doped GaN and ZnO.[29]

This thesis deals with understanding of electronic and magnetic properties of manganese doped gallium nitride ($Ga_{1-x}Mn_xN$) nanowires. The initial theoretical results suggested RKKY type interaction more likely in ($Ga_{1-x}Mn_xN$), but calculations based on first principle approach, *ab initio* based calculations and mean field Zener approach support carrier mediated magnetic ordering. Similarly, experimental studies give the contradictory conclusions. The magneto-optical studies does not support the hole mediated ferromagnetism agreeing with DFT based calculations, whereas X-ray spectroscopic studies confirm the co-existence of Mn^{2+} and Mn^{3+} in $Ga_{1-x}Mn_xN$ system, indicating carrier mediated double exchange mechanism more likely. In general, no theoretical calculations or experimental methodologies do not give explanation for magnetic interactions in wide class of DMS materials. The next section will discuss some of the important reported theoretical results about the origin of magnetic ordering in the $Ga_{1-x}Mn_xN$ system.

1.6 Theoretical Results on Origin of Ferromagnetism in $Ga_{1-x}Mn_xN$ System

The work of Dietl *et al.*[14] estimated high T_C in certain DMS materials such as TM doped GaN or ZnO assuming Zener model description or p-d hybridization along with mean field approximation. According to mean field theory, the ferromagnetic interaction occurs through free holes along with localized magnetic moments, and the spin-spin interaction is assumed to be long range. The estimated Curie temperature (T_C) for different semiconducting materials using mean field Zener model, assuming 5% transition metal dopant and hole

concentration above $10^{20}\,\mathrm{cm}^{-3}$ is shown in Figure 1.4. Another important aspect of this model is that consideration of the magnetocrystalline anisotropy, which arises due to the spin-orbit coupling in the host material. Moreover, it is determined that the spin-orbit coupling in the valence band can influence the easy axis of magnetization and magnitude of the T_C in p-type ferromagnetic semiconductors. The above modified Zener model has predicted higher T_C without considering either thermal fluctuations or disorder effects in the system.

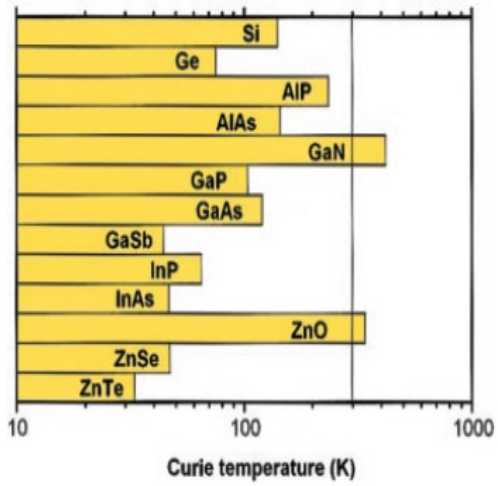

Figure 1.4: Predicted Curie temperatures for different semiconductor materials using mean field Zener double exchange model. According to the model, both Mn doped GaN and ZnO exhibit room temperature ferromagnetism.[14]††

Sato *et al.*[30] calculated magnetic ordering in GaX (X = P, Sb, N, As) with Mn dopants using first principles within the mean field approximation and predicted T_C with varying the carrier concentration. For GaN, Mn doping concentration of about 4% has shown the maximum T_C, and above which T_C started to diminish.

Litvinov and Dugaev[31] proposed an alternate model to describe the ferromagnetism in wide band gap semiconductors when doped with Mn or Fe. The localized moment in the crystal lattice virtually excites band electrons due to s-p or p-d exchange interactions and strength of the indirect exchange interaction depends on doping concentration (or location of the Fermi level). The results of this theory were based on virtual excitation between the

††From [T. Dietl, H. Ohno, F.Matsukura, J. Cibert and D. Ferrand, Science, 2000, 287, 1019-1022; http://dx.doi.org/10.1126/science.287.5455.1019]. Reprinted with permission from AAAS.

Mn acceptor level and the valence band. This model also accounts for the defects, which increase in number beyond 5% doping concentration. The increase in defect concentration will shift the Fermi level towards the conduction band compensating Mn acceptor levels. Finally, the Fermi level will be located in between the conduction band and the Mn acceptor level. This process will decrease the energy gap between the acceptor level and the edge of the conduction band. If the gap increases then the activation energy required to excite band electrons will be large, lowering the T_C. Results for the $Ga_{1-x}Mn_xN$ with different doping concentrations (Figure 1.5) clearly predict that for higher activation energy, T_C is lowered for all the Mn concentrations.

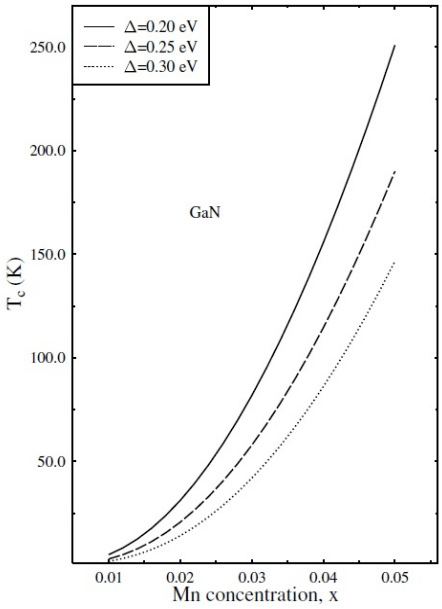

Figure 1.5: Dependence of T_C on activation energy ($\triangle$) in the case of $Ga_{1-x}Mn_xN$.[31‡‡]

The first principle total energy calculations performed by Mahadevan and Zunger[32] on various Mn doped III−V GaX (X = N, P, As, and Sb) semiconductors contradict the mean field Zener model description, so a unique model was devised to describe the ferromagnetism for the entire GaX series. They have predicted the following reasons for the stabilization of ferromagnetic energy in wide band gap $Ga_{1-x}Mn_xN$ semiconductors: (a) The holes are highly localized and in a deep acceptor state. The ferromagnetic energy is large even for

‡‡Reprinted with permission from (V. I. Litvinov and V. K. Dugaev, Phys. Rev. Lett., 2001, 86, 5593; http://dx.doi.org/10.1103/PhysRevLett.86.5593). Copyright (2001) by the American Physical Society.

farthest neighbour (Figure 1.6), therefore indirect or RKKY exchange mechanism dominates; (b) it also confirms the stabilization energy is large along certain crystallographic directions, for e.g., $Ga_{1-x}Mn_xN$ $\langle 110 \rangle$ direction has the largest stabilization energy, whereas $\langle 001 \rangle$ has the weakest energy; (c) the $p-$type dangling bonds of Ga vacancy sites hybridize with Mn d states, localizing p-d hybrids on Mn and its neighbours. The interaction between such half-filled spin-up channels with different Mn sites stabilises the ferromagnetism.

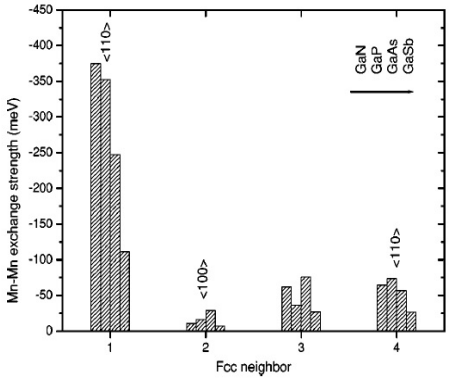

Figure 1.6: First principle calculation results for the exchange interaction strength between nearest neighbour Mn atoms in GaN, GaP, GaAs and GaSb respectively. It is clearly evident that Mn atoms interaction is stronger even in the fourth neighbour along $\langle 110 \rangle$ directions in $Ga_{1-x}Mn_xN$.[32]¶¶

Virot *et al.*[33] studied magnetic interactions in $Ga_{1-x}Mn_xN$ using local spin density approximation with Hubbard correction (LSDA+U) method and their results question the hole mediated ferromagnetism in DMSs. In addition to LSDA+U, they have also used a ligand field approach to support their hypothesis. The Jahn-Teller effect leads to insulating behaviour of $Ga_{1-x}Mn_xN$ (both zinc blende and wurtzite crystal structures), stabilizing Mn^{3+} in the system. There are no carriers to mediate the magnetism. The holes in the system could be retained in the system by means of co-doping and will enhance the hole mediated ferromagnetism. To support their hypothesis of a non-hole mediated mechanism, the same group studied optical properties of $Ga_{1-x}Mn_xN$ constructing the supercell of 64 atoms using a full-potential linearized augmented plane wave method (FPLAPW). The calculated absorption coefficients in comparison with experiment correspond to Mn^{3+} peaks, which is explained based on the ligand field theory disagreeing with the hole mediated ferromagnetism.[34]

¶¶Reprinted with permission from (Appl. Phys. Lett., 2004, 95, 2860; http://dx.doi.org/10.1063/1.1799245). Copyright (2004), AIP Publishing LLC.

Van Schilfgaarde and Mryasov[35] performed local-density functional theory calculations to understand the magnetic exchange interactions between host III-V semiconductors and various TM dopants such as Cr, Mn, and Fe (1 to 5% doping concentrations). The calculated results strongly contradict the simple exchange models. They concluded that a possible reason for observed anomalous behaviour is due to the formation of small nanoclusters of a few magnetic atoms resulting in ferromagnetism.

Popovic *et al.*[36] studied the exchange interaction by assuming both interstitial and substitutional doping of Mn (3%) in GaN. The interstitial Mn (Mn_I) site acts as a donor, whereas substitutional (Mn_{Ga}) acts as an acceptor and they form Coulomb stabilized complexes such as $Mn_{Ga}Mn_IMn_{Ga}$. The substitutional Mn sites passivated by interstitial Mn might be a reason for observed carrier doping deficiency in $Ga_{1-x}Mn_xN$ systems. Their band structure calculations confirm the location of the Mn impurity level away from the valence band edge, but their wave function spreads far away from the impurity centre and preserves the long-range interactions. This results in p-d hybridization with nitrogen atoms and thereby transferring the magnetic moment to band electrons. The idea of substitutional versus interstitial Mn doping in GaN was further supported by extensive density functional theory (DFT) calculations.[37] However, the results of extensive DFT calculations favour the substitutional doping of Mn in GaN replacing the cation sites and stabilizing the ferromagnetic ordering.

Calculations based on the Monte Carlo method contradict the direct relationship between hole density and high T_C ferromagnetism.[38,39] The mean field Zener model over estimated the stability of ordered phases and predicted the high T_C in set of DMS materials. The kinetic-exchange model considers long wavelength collective spin-wave oscillations which limit high T_C in Mn doped III-V semiconductors proposed by mean field theory neglecting the spin oscillations.[40–42] Both mean field theory and kinetic-exchange model have been successfully applied to a number of phenomena in magnetic semiconductors, such as quantum wells,[43] interlayer coupling in superlattices,[42] temperature dependence of magnetization and heat capacity,[41] magnetic domain characteristics,[44] magnetic anisotropy,[45] and long-wavelength magnetic properties.[46]

None of the above described models are conclusive about the origin of magnetic ordering in DMSs and their results do not agree well. Similarly, there are several experimental results which predict the origin of magnetic ordering in wide band gap semiconductors based on optical,[47] magnetization hysteresis,[48–50] and element specific X-ray absorption studies.[51] The experimental studies have also revealed that magnetic properties in DMSs depend on synthetic or growth conditions. The next section will discuss the experimental results on magnetism in $Ga_{1-x}Mn_xN$, and possible origin of exchange interaction.

1.7 Experimental Studies on $Ga_{1-x}Mn_xN$ System

Earlier work on this system has been done via synthesizing micro-crystals of GaN by nitridization of pure metallic Ga in supercritical ammonia, or bulk crystals grown by reacting Ga/Mn alloys or GaN/Mn mixtures with ammonia at ∼1200 °C. As synthesised samples show ferromagnetism over a wide range of Mn doping concentrations.[48–50] The high quality $Ga_{1-x}Mn_xN$ thin films grown by an epitaxial method without any secondary phase below Mn concentration of ∼10% showed T_C at ∼750 °C.[52–54] The material showed room temperature ferromagnetism with a Mn doping concentration of ∼3-9% and antiferromagnetism above 9%. There are several reports on room temperature ferromagnetism in epitaxially grown $Ga_{1-x}Mn_xN$ thin films and with T_C between 20-940 K.[51,55,56] The origin of ferromagnetism is still unclear and the growth conditions play a vital role in variation of T_C and formation of other phases is likely during the incorporation of Mn dopant.

All the above mentioned studies demonstrated room temperature magnetic ordering based on magnetization measurements or hysteresis, however this method alone is not sufficient to predict ferromagnetism and could be misleading. Moreover, magnetic measurements do not give any information about structural properties. Therefore detailed characterization of as synthesised samples is necessary before coming to the conclusion based on magnetization studies. On that note, Zajac *et al.*[57] synthesized GaN with 5% Mn doping concentration using ammonothermal method and characterized samples using various techniques such as X-ray diffraction (XRD) and Raman spectroscopy. Their XRD peaks confirm the clear presence of hexagonal $Ga_{1-x}Mn_xN$ phase along with small secondary Mn_3N_2 phase. The Raman spectroscopy studies clearly exhibit characteristic hexagonal GaN modes along with associated Mn-induced lattice disorder. Electron spin resonance and magnetization measurements studies confirm Mn is in +2 oxidation state and support the hole mediated ferromagnetism. However, a small contribution from the precipitated secondary phase during the synthesis cannot be ruled out.

The optical spectroscopy studies on $Ga_{1-x}Mn_xN$ contradict the carrier mediated ferromagnetism. Before discussing optical properties, it is essential to understand the electronic structure of Mn in GaN. In the wurtzite crystal lattice, Ga is quasi-tetrahedrally coordinated with N atoms and has an oxidation state of +3 (sp^3 hybridization). The doping of Mn will replace the Ga sites, and Mn having a +3 oxidation state will be in a neutral configuration (d^4). However, depending on the position of the Fermi level, which is closer to the conduction band in GaN, another electron may be obtained from the donor site, leaving no holes near the valence band with larger binding energy. Therefore, there is a possibility of coexistence of both Mn^{2+} and Mn^{3+} in GaN.[27]

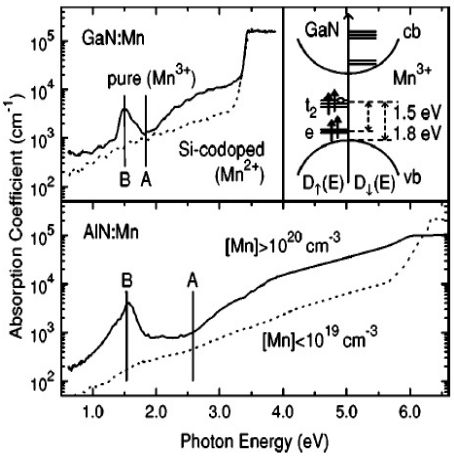

Figure 1.7: Optical absorption spectra of Mn doped GaN and Si codoped $Ga_{1-x}Mn_xN$. Peak A corresponds to the position of acceptor levels to the valence band. Broad peak B is the spin allowed transition of the neutral Mn^{3+}. The side panel is a schematic of the spin-split density of states (DOS) and position of Mn acceptor level with respect to valence band maxima. Bottom panel is absorption spectrum of Mn doped AlN.[47]†††

Graf *et al.*[47] studied optical absorption spectra of $Ga_{1-x}Mn_xN$ and codoped $Ga_{1-x}Mn_xN$ with Si (rich in Mn^{2+}) films, which were grown on sapphire substrates by plasma induced molecular beam epitaxy with Mn concentrations of about $10^{20}\,cm^{-3}$ and thickness of about 1 µm. The majority of the Mn is in +3 oxidation state in pure $Ga_{1-x}Mn_xN$ as confirmed from electron spin resonance and magnetization measurements. Their absorption spectra confirm the presence of Mn acceptor level in the middle of the gap, about 1.8 eV from the valence band. They have observed two main peaks in the optical absorption spectra. The transition corresponding to 1.8 eV is the direct transition of holes to the valence band from Mn^{3+} acceptor. The peak at 1.5 eV is assigned to a transition corresponding to spin forbidden ${}^4T_1 \rightarrow {}^6A_1$ in tetrahedral Mn^{2+} and the same peak is not observed in Si codoped $Ga_{1-x}Mn_xN$ which is rich in Mn^{2+}(Figure 1.7). Therefore, it corresponds to the spin allowed ${}^5E \rightarrow {}^5T$ transition of the deep neutral Mn^{3+} state. On the same note, magneto-optical experiments predicted non-hole mediated magnetic ordering in $Ga_{1-x}Mn_xN$. These results are consistent with DFT results, which predicted the deep $Mn^{2+/3+}$ acceptor levels in GaN and contradict the hole mediated ferromagnetism.

Element specific X-ray absorption can be a powerful tool to understand the nature of

†††Reprinted with permission from (Appl. Phys. Lett., 2002, 81, 5159; http://dx.doi.org/10.1063/1.1530374). Copyright (2002), AIP Publishing LLC.

Mn ion in GaN. Mn $L_{2,3}$-edge X-ray absorption near edge structure (XANES) can directly probe the $3d$ empty states and is sensitive to changing oxidation states of the absorbing atom. The L-edge multiplet features confirm that Mn is in +2 oxidation state in the case of $Ga_{1-x}Mn_xN$ thin films.[58] The extended X-ray absorption fine structure (EXAFS) confirm substitutional incorporation of Mn on Ga sites.[51] All the experimental results on thin films predict different Curie temperatures ranging between 10-945 K. Such a variation is due to sample preparation conditions, structural defects and secondary phases.

The bottom-up approach to rationally control key parameters in nanostructured materials such as chemical composition, structure, size, morphology, and incorporation of dopants significantly change the electrical and optical properties of the materials. Among various nanostructures, including nanocrystals and nanotubes, nanowires (NWs) have emerged as ideal candidates to control and manipulate growth parameters. The controlled growth, smaller diameter, larger surface area and smooth surface make NWs suitable building blocks in electronics,[59–69] photonics,[70–82] solar-cell applications,[83–87] batteries,[88–92] nanogenerators,[93,94] and biological/chemical sensors.[95–102] Moreover, controlled growth of NWs enable the development of a biosensor with integrated detectors and electrodes, in a single nanowire during the growth.[103–105] In addition, several theoretical and experimental studies have shown that III-V-based DMS NW systems exhibit different magnetic properties compared to bulk or thin films.[106,107] Therefore, NWs can replace traditional thin film or wafer based technology in terms of cost effectiveness, miniaturization in size, and fabricability.

In order to synthesize one-dimensional nanostructures of desired material, morphology, and size, it is essential to understand the growth mechanism within purview of thermodynamics and kinetics rationale.

1.8 Growth Mechanism of Nanowires

One dimensional nanostructures were grown using the vapor-liquid-solid (VLS) mechanism[108] and this method was successful in producing high quality single crystalline NWs with larger yield. The VLS mechanism was successfully employed in the synthesis of 10 nm length scale NWs in the late 1990s.[109] Earlier, VLS mechanism was applied explicitly in the laser ablation process of producing NWs and high energy lasers were used to generate the vapor phase of a metal source. The single crystalline Si and Ge NWs were synthesised using laser ablation and VLS mechanism.[109]

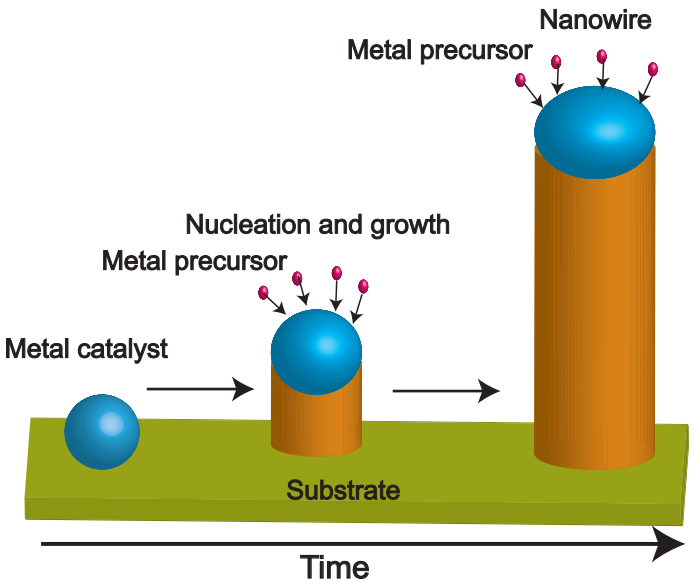

Figure 1.8: Schematics of the VLS mechanism. The first step is to heat the metal catalyst above the eutectic temperature to form a metal-semiconductor alloy. The reaction time is continued to feed the semiconductor vapors into the liquid droplets until the liquid alloy supersaturates leading to nucleation and uniaxial nanowire growth.

In a typical VLS process, the vapor phase of the metal precursor is first achieved, followed by the second step in which gaseous reactants are diffused into nano-sized catalyst liquid droplets. The third step is nucleation and growth of single crystalline rods and finally wires.[110] Essentially, catalyst droplets initiate and guide the one dimensional growth. The size of the liquid catalyst droplets determine the diameter of the NWs and catalyst size remains unchanged during growth. The choice of metal catalyst for NW synthesis is also important for the successful growth of the NWs, and can be chosen using a phase diagram. Each liquid droplet serves as a virtual template and avoids lateral growth of the individual nanowire.[105] Nanowire length can be controlled by modifying the reaction time, longer wires being obtained by increasing the reaction time (Figure 1.8). Nanowire growth is primarily driven by thermodynamics and as a result the preferred growth direction is the one which minimizes the total free energy of the system.[103] However, kinetic effects also play a very important role in various stages of growth and deciding overall quality of NWs. The VLS mechanism can be used to grow NWs via molecular beam epitaxy (MBE) and laser ablation methods, but chemical vapor deposition (CVD) has been most widely used because of its flexibility, simpler instrumentation and excellent control over growth parameters.[104]

Another possible mechanism is the vapor-solid (VS) growth mechanism. The NWs can be grown based on the following process considering both thermodynamic and kinetic parameters: (a) An anisotropic growth process of NWs, essentially preferential reactivity and binding of gas phase reactants along the specific crystal orientation to minimize the free energy, favouring one dimensional growth; (b) Frank's screw dislocation mechanism; (c) formation of defects during the growth; (d) self-catalytic VLS mechanism, involving the growth of NWs without the use of a catalyst. In both (b) and (c), the defect sites are known to have larger reactivity as they have larger sticking coefficients for gaseous phase metal precursors, thus allowing enhanced reactivity and deposition of gas phase reactants at these defect sites. However, the VS mechanism is difficult to predict as it lacks the thermodynamic and kinetic descriptions.[103]

1.9 Doping Mechanism in Nanowires

The ability to incorporate dopants during nanowire growth is important and such a process will significantly enhance the optical and electrical properties of the NWs, which is essential for device applications. The dopant impurities are incorporated into NWs using dopant precursor in the gaseous state during synthesis; metal dopants are frequently used in the process.[111] Studies on dopant incorporation mechanism in nanostructures are few in number. Tutuc *et al.*[112] studied the dopant incorporation mechanism in phosphorous (P) doped germanium (Ge) NWs through electrical measurements. They observed the change in the device characteristics by changing the growth sequence and concluded that dopants predominately incorporate by binding onto the nanowire surface. Similar arguments were made by Stamplecoskie *et al.*[113] in various TM doped GaN NWs. However, there are no specific studies to quantify the dilute dopant incorporation at the single nanowire level.

In that regard, Perea *et al.*[114] have studied the dopant distribution efficiency and incorporation rate using pulsed laser atom probe tomography in individual phosphorus doped germanium NWs. In this technique, the tip of a single nanowire is evaporated by focussing 10 ps laser pulses having a wavelength of 532 nm. The evaporated positive ion was detected by a 2-D position sensitive detector. The type of atom evaporated can be determined from mass to charge ratio, which is calculated based on the time delay between sending the laser pulse and the detection of the ion; the chemical identity of the ion is determined by analysing the peak position of the resulting mass spectrum. This technique allows one to construct well defined 3-D composition maps at the sub-nanometer resolution obtained in the evaporation, detection, and reconstruction process.[115,116] This study confirmed that there are two possibilities by which dopants incorporate into NWs.

Firstly, dopant is dissolved in a liquid catalyst and migrates towards liquid-solid interface to be deposited into the nanowire core. In a second option, dopant may be incorporated directly from the vapor to solid along the surface of the wire (Figure 1.9).

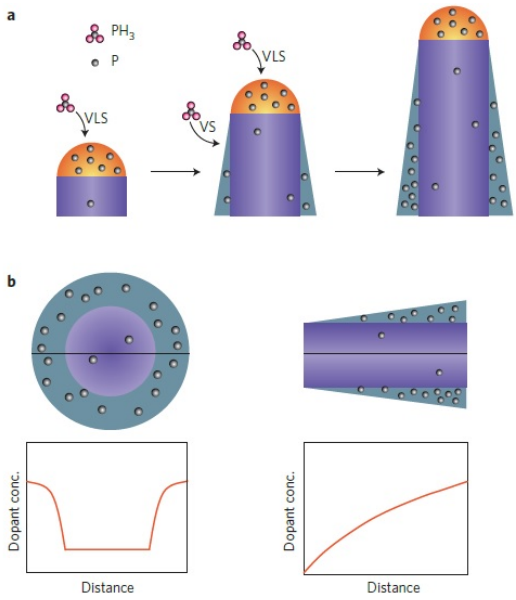

Figure 1.9: Mechanism of phosphorus incorporation into germanium NWs. (a) Ge NWs were grown form GeH_4 precursors using a gold catalyst via VLS mechanism. The phosphorus dopants (grey) incorporate through VLS (tip) and VS (surface) processes, resulting in a heavily doped outer layer and an undoped core. (b) Radial (left) and longitudinal (right) view of the nanowire and plot of dopant distribution, respectively. [111]§§§

They have additionally modelled the discrepancy in dopant concentrations along the surface and core quantitatively. The surface accumulation of dopants is high because phosphor precursors readily undergo thermally active decomposition on the surface more than germanium precursors and VS growth dominates. The same argument was applied to catalyst mediated VLS growth when the catalyst induces decomposition of germanium at the nanowire tip and the rate of decomposition of phosphorous is very low.

§§§Reprinted by permission from Macmillan Publishers Ltd: [Nature Nanotechnology](Nat. Nanotechnol., 2009, 4, 282-283; http://dx.doi.org/10.1038/nnano.2009.104), copyright(2009).

1.10 Anisotropy and Magnetization Studies in Nanowires

Nanowires have high aspect ratios due to their cylindrical shape and strong confinement of electrons along the radial direction. Therefore, one could expect significant change in electrical and optical properties between the long and short axes of the NWs. It was first observed in the case of free standing individual InP NWs using polarization dependent photoluminescence (PL) spectroscopy.[72] The large difference in PL spectra is observed for polarization parallel and perpendicular to the long axis of the nanowire. This giant shape dependent polarization anisotropy observed in NWs makes them useful in developing photodetectors, optically gated switches, and light sources.

Magnetic properties of solids depend on several factors in nanostructures, including the influence of surfaces, carrier confinement and reduction in size, which lead to formation of a single magnetic domain. Zero dimensional materials have shown weak structural anisotropy due to their smaller size and formation of a single domain. In one dimensional magnetic nanostructures, magnetic domains are formed in the vicinity of the nanowire and play a very important role in spin dependent transport phenomena or in spintronics based devices. Magnetic anisotropy in NWs can be of two possible origins, shape anisotropy and magnetocrystalline anisotropy.

Shape anisotropy usually occurs in polycrystalline samples in which there is no preferred crystal orientation and will have no overall crystalline anisotropy. If the sample is not spherical, then the long axis will be the easy axis of magnetization.

Magnetocrystalline anisotropy phenomenon is distinct and it depends on the crystallographic growth direction. Magnetization occurs in a preferred crystallographic direction. For example, in a hexagonal crystal structure it is found that, along the c-axis magnetization saturation occurs more rapidly than others, hence the c-axis is an easy axis of magnetization. The magnetocrystalline anisotropy energy is the energy difference per unit volume between samples magnetized along easy and hard directions (see Appendix B for details). Strength of the magnetocrystalline anisotropy depends on spin-orbit coupling.[26]

Wang *et al.*[106] have studied the origin of ferromagnetism in wurtzite Mn in GaN NWs using DFT calculations. Their results show that due to the distinct topology of the nanowire surface and the radial confinement of electrons, the Mn atoms tend to couple ferromagnetically, while in the case of thin films antiferromagnetic ordering is preferred. They have also observed change in magnitude of the magnetic moment by varying the thickness of the NWs, and the double exchange mechanism was responsible for the observed magnetic ordering. Furthermore, calculations on the anisotropic energy confirm that the

magnetic moment orients preferably along the $\langle 10\bar{1}0 \rangle$ direction and the wire axis is oriented along the $\langle 0001 \rangle$ direction.

Fundamental understanding of magnetic ordering in the $Ga_{1-x}Mn_xN$ nanowire system is essential for the development of low dimensional based spintronic devices. For example, dopant incorporation and distribution, quantification of oxidation state of Mn, whether it is Mn^{2+} or Mn^{3+}, and the type of anisotropy are responsible for magnetic ordering. The knowledge from such studies could help to understand the origin of magnetic ordering and the possibility of spin manipulation at the nanoscale.

Another important material that has shown significant anisotropy along the crystallographic *b*-axis is gallium oxide (Ga_2O_3) and is confirmed through various experimental and theoretical results.

1.11 Transparent Metal Oxides

Wide band gap transparent metal oxides (TMOs) have attracted ever increasing attention over the past few decades because of their structural versatility and phase-dependent properties,[117–120] as well as the ability to combine transparency and conductivity.[121,122] In addition, they exhibit polymorphism, giving different functional properties depending on the phase. In TMOs, oxygen defects have a significant role in controlling optical and electrical properties.[120,123,124] Owing to these properties, TMOs have found applications in photovoltaics, smart energy-efficient windows, transparent electrodes, high-definition flat panel displays, touch screen devices, and sensors.[125–128]

1.12 Gallium Oxide and its Electronic Properties

Gallium oxide (Ga_2O_3) is a polymorphic material, which could exist in five different crystalline phases (α, β, γ, δ and ϵ), out of which β-Ga_2O_3 with a monoclinic crystal structure is thermodynamically stable at room temperature.[129] The β-Ga_2O_3 is classified as an n-type semiconductor with the band gap of 4.9 eV.[130–132] The semiconducting properties are enabled due to the presence of oxygen vacancies forming shallow donor states.[131–133] Depending on the preparation conditions, β-Ga_2O_3 can also emit light over a wide range, from infrared (IR) to ultraviolet.[131,134–136] The observed emissions arise from the presence of various defects, and the most prominent emission in the blue spectral region is associated with defect-based donor-acceptor pair recombination.[131] These unique properties make

β-Ga_2O_3 suitable for developing gas sensors, phosphors, catalysts, and optoelectronic devices.[134,136–138]

In contrast to other semiconducting TMOs, β-Ga_2O_3 single crystals have shown unique optical, electrical, and magnetic properties along the crystallographic b-direction.[139,140] The band structure calculations based on extended Hückel approximation have suggested that such anomalous behavior could be due to delocalization of the conduction band electrons along doubly connected rutile GaO_6 octahedral chains in the b-direction.[139] It is therefore essential to understand the origin of anisotropic behavior at the molecular level and the correlation between the anisotropy and electronic structure of Ga_2O_3.

Previous experimental work on anisotropic behavior of single crystalline β-Ga_2O_3 was based on optical and electrical measurements at room temperature.[140] The optical transmission spectra collected using linearly polarized light revealed the band edge absorption at 4.79 eV and 4.52 eV for the electric field vector (E) parallel to the crystallographic b and c axis, respectively, which has been associated with different valence band electronic structure for these two directions.[140] Similarly, electrical and Hall measurements showed an order of magnitude higher conductivity and carrier mobility along the b axes rather than c axis.[140] These differences have been attributed to a larger curvature of the bottom of the conduction band along the b axis, and associated with the crystal structure of the rutile chains in this direction.

Recently, attention has turned to β-Ga_2O_3 NWs as building blocks for nanodevices. As described previously, due to the controlled oriented single crystalline growth of the NWs by changing the growth parameters using the CVD method, this is a model system for studying the anisotropic behaviour experimentally. There has been less effort made to understand electronic structure of β-Ga_2O_3 NWs. In contrast to optical absorption, X-ray absorption is an element specific spectroscopic technique and can serve as a local molecular-level probe of the electronic structure. Zhou *et al.*[141] have performed conventional Ga L-edge and O K-edge X-ray XANES analysis in combination with time-resolved X-ray excited optical luminescence (XEOL) on β-Ga_2O_3 NW ensemble, focusing on the origin of various PL transitions in Ga_2O_3 NWs.

1.13 Purpose and Scope of the Thesis

The first part of the thesis is focused on synthesis and characterization of Mn doped GaN NWs using the CVD method. Crystal structure, morphology, growth mechanism and dopant incorporation of as synthesized NWs were systematically studied using X-ray diffraction (XRD), scanning electron microscopy (SEM) and transmission electron microscopy

(TEM) techniques, respectively. This study is essential to understand crystallinity, dopant distribution, and the formation of secondary phases.

The aim of the second part is to understand the electronic structure of Mn in GaN at the single nanowire level using X-ray spectro-microscopy techniques. To date, most of the reported studies on $Ga_{1-x}Mn_xN$ NWs were done using ensemble measurement techniques, such as X-ray photoelectron spectroscopy (XPS),[142] electron energy loss spectroscopy (EELS),[107] photoluminescence (PL),[143] and X-ray absorption spectroscopy (XAS).[142,144] Although all of the above mentioned methods are robust in determining the electronic structure of Mn in GaN, the presence of co-deposited dopant precursors and other dopant-based secondary phases during NW growth is a possibility, thereby rendering the results insufficiently specific. The X-ray spectro-microscopy techniques such as scanning transmission X-ray microscopy (STXM) using a synchrotron source provide excellent sensitivity, elemental specificity, and high spatial resolution to detect Mn speciation and magnetization at the single NW level. XANES spectro−microscopic methods were used together with structural and theoretical investigations to study the electronic structure and magnetic properties of single $Ga_{1-x}Mn_xN$ NWs grown by CVD. By analysing Mn L-edge experimental data along with crystal field multiplet calculations, the oxidation state of Mn (+2/+3) was determined quantitatively in individual GaN NWs. The speciation of Mn is essential to predict the carrier or non-carrier mediated magnetic ordering, which is an important matter of debate in wide band gap DMSs.

The third part deals with understanding the atomic origin of magnetic ordering using X-ray magnetic circular dichroism (XMCD) spectroscopy of $Ga_{1-x}Mn_xN$ NWs. The spin and angular momentum can be quantified using the XMCD sum rule in a single nanowire. The magnetic moment calculated in individual NWs was compared with bulk magnetization measurements using a physical properties measurement system (PPMS). This study is important in order to predict the orientation or anisotropic nature of the NWs. Anisotropic behaviour can be controlled by changing the growth conditions during the synthesis. These results open the possibility for designing spintronic devices based on DMS NWs.

Finally, this thesis discusses synthesis, growth mechanism and origin of anisotropy in individual β-Ga_2O_3 NWs. The understanding of growth mechanisms and formation of facets is essential to tune the optical properties in these quasi-1D Ga_2O_3 nanostructures synthesized via VS mechanism. The origin of anisotropy in individual β-Ga_2O_3 NWs was studied by linearly polarized XANES imaging, using STXM. The polarized XANES spectroscopy is a powerful tool to study the electronic structure of the element of interest along different crystallographic directions, providing the information about the bond character (i.e., covalency), orbital orientation, and orbital contribution to the electronic band states, which are directly related to the anisotropic behavior. This study particularly

focusses on polarized O K-edge (anion) absorption measurements using linearly polarized X-rays parallel and perpendicular to the NW growth axis. The experimental results were compared with calculated XANES spectra and the orbital angular momentum projected density of states (PDOS) for different crystallographic directions. This study helped to understand the electronic origin of anisotropy at the molecular level. The tuning of electronic properties of NWs during growth is quintessential for nanowire based devices.

Chapter 2

Experimental Methods and Computational Details

2.1 Materials

All the chemicals purchased from the manufacturers were used as received without any further purification. Gallium (Ga; 99.99% pure) metal ingots and manganese chloride ($MnCl_2$) were purchased from Strem Chemicals Inc. High purity (grade 5) carrier gases, ammonia (NH_3), hydrogen (H_2), oxygen (O_2), and argon (Ar) were purchased from Praxair Inc.

2.2 Growth Procedure

2.2.1 Synthesis of Manganese Doped Gallium Nitride NWs

Manganese doped gallium nitride NWs were grown by the CVD method using Ga metal, $MnCl_2$ as Mn precursor, and ultrapure NH_3 and H_2 gases. The reactions were performed in a two-inch three-temperature-zone tube furnace using Ni nanoparticles as a catalyst.[113,145] The catalyst particles were generated *in situ* from $Ni(NO_3)_2$ and deposited on a Si(111) growth substrate. The substrate was placed about 2 mm downstream from the reaction material. First, the tube was evacuated to 0.1 Torr and purged with argon gas to remove atmospheric oxygen. This process was repeated several times before proceeding to the NW growth. The reaction was carried out at the temperature of 950 °C under 50 sccm flow of

NH_3 and H_2 at the pressure of 200 Torr for two hours. Finally, the tube was allowed to cool down to room temperature in the presence of argon.

2.2.2 Synthesis of Gallium Oxide NWs

Gallium oxide NWs were grown by the CVD method using elemental Ga as the precursor. These NWs were grown on silicon (Si) substrates in a two inch diameter quartz tube. The tube was inserted in a three-zone tube furnace. Prior to synthesis, the Si (111) substrates were washed in distilled water and ethanol, and completely dried under Ar flow. The growth substrate of size 1 cm^2 along with ~50 mg of Ga metal on a mica sheet (Ted Pella Inc.) was placed on a quartz boat. The growth substrate was placed ~2 cm away from the metal precursor and inserted at the centre of the tube furnace. The growth substrate was placed downstream of the carrier gas. The tube was evacuated to 0.1 Torr and purged with argon 2-3 times to clear the residual atmospheric oxygen, and finally the temperature of the furnace was raised to the desired growth temperature (700-1050 °C). A mixture of oxygen gas (1.5-6 sccm) and argon (100-400 sccm) was introduced after reaching the reaction temperature. The Ga_2O_3 NWs were grown under constant temperature. Once the specified reaction time was completed, the tube was allowed to cool down to room temperature under argon flow.[138]

2.3 Structural Characterization Techniques

2.3.1 X-ray Diffraction Measurements

The preliminary crystal structure of as-synthesised $Ga_{1-x}Mn_xN$ and Ga_2O_3 NWs was determined by powder XRD, using an INEL XRG 3000 diffractometer equipped with a Cu Kα_1 radiation source ($\lambda = 1.540\,598$ Å), germanium crystal monochromator, and an INEL CPS 120 curved position sensitive detector. For XRD measurements, the growth substrate was mounted on an aluminum sample holder and irradiated with finely focused monochromatic Cu Kα_1 radiation.

2.3.2 Scanning Electron Microscopy

Field emission scanning electron microscopy (SEM; LEO 1530) measurements were done on as-synthesised NWs to obtain information about yield, overall morphology, length and

elemental composition, using energy dispersive X-ray spectroscopy (EDS) measurements. The SEM operating voltage was 10 kV and all the images were collected in secondary electron (SE2) mode.

2.3.3 Transmission Electron Microscopy

The morphology, crystallinity, and lattice orientation of single NWs were further analyzed using high resolution transmission electron microscopy (HRTEM) and selected area electron diffraction (SAED) with a JEOL 2010F microscope operating at 200 kV. For TEM measurements, the NWs were dispersed in ethanol by sonicating the growth substrate for 3-5 s. The NWs dispersed in ethanol were then deposited using a micropipette on a TEM copper grid coated with lacey Formvar/carbon support film manufactured by Ted Pella Inc.

Z-contrast scanning transmission electron microscopy (STEM) experiments were performed with the FEI Titan 80-300 cubed electron microscope at the Canadian Centre for Electron Microscopy (CCEM). The microscope is equipped with a hexapole-based aberration corrector for the image forming lens (which forms the high annular dark-field image) and a corrector for the probe forming lens. The instrument can achieve subangstrom resolution for phase contrast imaging and STEM.

2.4 X-ray Absorption Spectroscopy

X-ray absorption spectroscopy (XAS) is a unique tool used to probe the local structure around the element of interest within a material. It can be used to study wide range of materials, from crystalline to amorphous materials. XAS essentially measures the absorption coefficient ($\mu(E)$) as a function of X-ray energy E where $\mu(E)$ decreases as X-ray energy increases. However, there is a steep increase in the absorption coefficient at a particular energy, which is characteristic of the atom being probed. This process can occur only when the incident X-ray photon has enough energy to eject electrons from the low-energy bound states in the atom and is called an absorption edge. The narrow domain containing fine structures within a few eVs near the absorption edge is called the X-ray absorption near edge structure (XANES) or near edge X-ray absorption fine structure (NEXAFS).[146]

2.4.1 Synchrotron Radiation

To perform XAS measurements, one needs X-ray beams of tunable energy and this is made possible using synchrotron radiation. It is possible to generate the electromagnetic radiation by accelerating charged particles at a relativistic speed. Synchrotron radiation is generated by accelerating electrons near the speed of light in the presence of an oscillating strong magnetic field. The total number of photons/s in a beam is called the "flux" and the number of photons/s/area which is incident on a target is called the "intensity". The term "brilliance" is that used to describe the X-ray sources and optics and has dimension photons/s/(source area mm^2)/(source angular divergence $mrad^2$). The advantage of using a high brilliance is, it can reduce the spatial size by increasing the angular divergence or vice versa, but not together at once. Figure of merit of a synchrotron radiation is measured by brilliance, and synchrotron radiation has a brilliance many orders of magnitude higher than X-ray tubes.[146,147]

A brilliant source means one which can emit many photons per second, with a small source size, and a small angular divergence. The smaller angular divergence makes it possible for X-ray optics, such as mirrors and monochromators, of reasonable size to collect photons. Earlier, synchrotron radiation was generated as electrons energy loss in electron storage rings. The newest synchrotron sources (third generation facilities) are composed of several components such as, the electron gun, linear accelerator, booster ring, and storage ring and are specifically optimized to produce the brightest possible light by the use of undulators and wigglers. The process of producing synchrotron radiation begins at the electron gun, where the cathode heated through application of high voltage produces pulses of electrons. The heated cathode is made up of a tungsten-oxide disk and high voltage provides enough energy to get some electrons from the surface. The high voltage repels electrons, accelerating them toward the linear accelerator (LINAC). LINAC consist of a series of radio frequency cavities in which radio frequency standing electromagnetic field was maintained. The bunch of electrons "surf" through the oscillating wave field, pushing the electrons forward. At this stage, electrons gain the energy of 250 MeV and are travel at the relativistic field (99.9998% of the speed of light).

The electron energy is further increased by circulation in booster rings, and transfer to "storage rings". These consist of evacuated pipes under ultra-high (10^{-12} Torr) vacuum through which relativistic electrons travel in a straight path until they experience a strong magnetic field in the vertical direction which is produced by bend magnets. The electrons in magnetic field experience a force that causes them to move in a single curved trajectory with a radius of curvature extending up to the order of several meters; later they continue down another straight section. This process will continue until making their path look like

a polygon rather than a circle. The recirculation of the same electron continues for hours or days by generating X-rays. As electrons revolve around their path, radiation is emitted in a fan of order $\frac{1}{\gamma}$ (radians) in angular width, where $\gamma = {}^{E}/_{mc^2}$ (E is electron energy and mc^2 is its rest mass). Nowadays, magnetic field is produced by a special collection of magnets called insertion devices and can be inserted into the straight section between bend magnets, which will increase brightness of the beam (third generation). These are called undulators/wigglers and have a great advantage in producing radiation, which is tuned to experimental needs.

The arrangements of magnets in undulators and wigglers are the same, the exception being that they are operated under different conditions. The undulator radiation is generated when a highly relativistic electron experiences a weak periodic magnetic field. Due to the relatively weak magnetic field, angular deflection of the electrons is smaller than angular width ${}^{1}/_{\gamma}$. The wiggler radiation is generated in a similar way, but in stronger magnetic field with a larger deflection.

In this thesis, all the experiments were performed at the spectro-microscopy (SM) beamline, at the Canadian Light Source. An APPLE-II undulator was used to produce an intense beam with user defined polarizations. Therefore, the next section will discuss briefly about undulator radiation and obtaining different polarizations.

2.4.2 Undulators

Specialised magnetic structures were made to generate light of various polarizations to study magnetic materials, helical structures and bonding properties. Therefore, it is essential to have a light source with the greatest freedom of both adjustable polarization and wavelength. This is made possible by APPLE-II (advanced planar polarized radiation light emitter-II) type elliptically polarized undulator (EPU). An APPLE-II undulator consists of four arrays of movable magnets placed diagonally opposite to each other.[147–149] The parallel longitudinal motion of two diagonal rows of magnets produce horizontal or vertical and elliptically polarized light. In this configuration a phase difference of 90° is introduced between the horizontal and vertical component of the magnetic field and projection on the x-y plane is an ellipse with a principal axis parallel to the x and y axes. The linearly polarized light between the inclined angles +90° and −90° is obtained by moving two diagonal rows in opposite directions (Figure 2.1a) where horizontal and vertical fields are in phase in this case.[149]

There are two possible ways to generate circularly polarized light using undulators. First, symmetric and synchronised motion of the diagonally opposite, A1, A4 and A2, A3

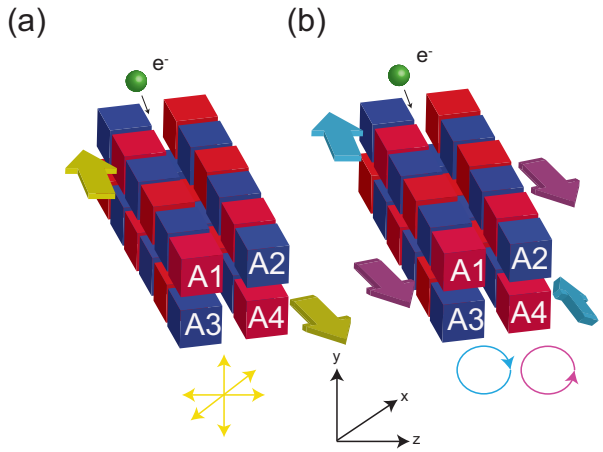

Figure 2.1: Schematics of different configurations of APPLE-II EPU: (a) Linearly polarized light covering all inclination angles between $+90°$ and $-90°$ by moving row A1 and A4 in opposite directions producing trajectory projection in a straight line in the midplane. (b) Circularly polarized light obtained by symmetric synchronised motion of A1, A4 and A2, A3 arrays. Elliptically polarized light is obtained by moving A1, A4 in one direction and A3, A2 in the opposite direction (not shown).

magnetic arrays. Second, all four arrays moving together in an antisymmetric mode.[147] The schematics of obtaining circularly polarized light is shown in Figure 2.1b.

2.4.3 Data Collection Modes

XAFS spectra can be recorded in various modes: transmission mode, fluorescence and total electron yield mode.

Detection by Transmission Mode

This is one of the most widely used modes of detecting the absorption from the sample. In this mode, intensity of the beam is measured before (I_0) and after (I) it is passing through the sample. This method follows the Beer-Lambert law and absorption coefficient, $\mu(E)x = \ln({}^{I_0}/_{I})$.

Detection by Fluorescence Mode

Intensity of fluorescence is directly proportional to the number of holes created in a core level, and hence to the absorption coefficient. When one must study a very diluted element in a transparent matrix, the absorption mode will lead to a too low absorption edge and intensity, which can be enhanced in fluorescence detection mode. Typically, fluorescence detector is placed 90° to the incident beam in the horizontal plane, with the sample at an angle (usually 45°) with respect to beam.

Total Electron Yield Method

It was demonstrated theoretically[150] and experimentally[151] that the total flux of photoelectrons is a function proportional to the absorption coefficient of the given element. Furthermore, sample depth that can be probed is of several hundreds to thousands of Angstroms depending on the energy of the relaxation process of a core hole (Auger emission). This type of detection allows the user to eliminate difficulties with sample thickness since the photon is not required to cross the sample in order to be detected. Even if this technique, leads to a smaller signal/noise ratio, compared to absorption, it is the best technique to study any thin (or thick) layer deposited onto a dense substrate.

2.4.4 XANES Theory

XAS involves the interaction of electromagnetic radiation with matter, intrinsically quantum mechanical. In XANES, the core electron is excited to the final state induced by X-rays and can be explained with time dependent perturbation theory.[152] The rate of transition can be approximated within the first order time dependent perturbation theory, and is proportional to the square modulus of the transition element matrix, or Fermi's golden rule,[153]

$$\frac{2\pi}{\hbar} \left|\langle \psi_f \left| H' \right| \psi_i \rangle\right|^2 \rho \tag{2.1}$$

where $|\psi_i\rangle$ and $|\psi_f\rangle$ are the initial and final states of the electron with energy E_i and E_f respectively, ρ is the density of states of the electrons, and H' is interaction Hamiltonian between an electron and electromagnetic field. The perturbed Hamiltonian H' in the presence of an electromagnetic field is,[152]

$$H' = \frac{1}{2m}\left(\vec{p} - \frac{e}{c}\vec{A}\right)^2 - e\Phi + V(r) \tag{2.2}$$

where, $\vec{A}$ is the vector potential of the electromagnetic wave and $\vec{p}$ is the vector momentum of electrons. Solving the above eq 2.2 within the Coulomb gauge approximation and commutation relations, the interaction Hamiltonian can be written as,[146]

$$\mu \propto \left| \langle \psi_f \left| \hat{\epsilon} \cdot \vec{r} e^{i\vec{k}\cdot\vec{r}} \right| \psi_i \rangle \right|^2 \rho(E_f - E_i - \hbar\omega) \tag{2.3}$$

where, $\hat{\epsilon}$, $\hbar\vec{k}$ and $\hbar\omega$ are the electric polarization vector, momentum vector and energy of the photon, respectively.

2.4.5 Dipole Approximation

The exponential term in eq 2.3 can be expanded as,

$$\langle \psi_f \left| \hat{\epsilon} \cdot \vec{r} e^{i\vec{k}\cdot\vec{r}} \right| \psi_i \rangle \approx \langle \psi_f \left| \hat{\epsilon} \cdot \vec{r} \right| \psi_i \rangle + i \langle \psi_f | (\hat{\epsilon} \cdot \vec{r})(\vec{k} \cdot \vec{r}) | \psi_i \rangle + ... \tag{2.4}$$

The first term in eq 2.4 corresponds to the dipole term and the second term corresponds to quadrapole term. The ratio of quadrapole to dipole terms is on the order of $\langle kr \rangle$ is $\left(Z_{eff}/137\right)^2$ times the electric dipole, and it is concluded that the dipole approximation holds well when neglecting the quadrapole term. However, the quadrapole term cannot be ignored and is useful in the pre-edge region of transition metal complexes.[146] The estimation is that the quadrapole/dipole ratio increases quadratically with Z and is useful to consider for heavier elements. The terms higher than quadrapole have negligible effect on X-ray spectra and can be omitted. The final form of the X-ray absorption cross section for non-magnetic samples, choosing only the real part of the initial and final state wave function in eq 2.4 is,[154]

$$\mu(\omega) = 4\pi^2 \alpha \hbar\omega \sum_{i,f} \left(\frac{1}{d_i} \right) |\langle \psi_f | \hat{\epsilon} \cdot \vec{r} | \psi_i \rangle|^2 \delta(E_f - E_i - \hbar\omega) \tag{2.5}$$

where, α is the fine structure constant, which gives the strength of the electromagnetic radiation and d_i is degeneracy of the ground state. The above approximations made in eq 2.5 holds well for most of the experimental circumstances tested so far.[146]

XANES is a unique tool compared to other optical spectroscopy methods as electrons are excited from a core level or bound state ($1s$ in K-edge, $2s$ or $2p$ states for L-edges) and it probes the continuum states above the absorption edge. The initial states are well localized around the central absorbing atom and fine structures are observed. The well localized structure is useful in determining the point symmetry, hybridization and electronic structure of the absorbing atom.[146]

2.4.6 Selection Rules

XAS involves exciting core level bound electrons and has dominant interactions with nuclei and electrons of the central absorbing atom. Therefore, the initial state of an electron can be approximated with its angular momentum quantum numbers l and m. The final state wave function $\langle\psi_f|$ can be written as a linear combination of specific l and m (i.e., a linear combination of $Y_{l,m}$ spherical harmonics with $m = -1, 0, +1$) and is eigenfunction of angular momentum operators L^2 and L_Z.[155] Due to the orthogonality of spherical harmonics, transition will only occur to final states with appropriate symmetry. By this argument, one can state the electric dipole approximation as $\Delta\lambda = \lambda' - \lambda = \pm 1$, where λ and λ' are the angular momentum of core level $|\psi_i\rangle$ and final state $|\psi_f\rangle$, respectively.[154]

As mentioned, the core level is a combination of electronic and nuclear potentials with a spherical symmetry and with well defined orbital quantum numbers. The final state is complicated, but can always be expressed as a set of spherical harmonics. The electric dipole approximation implies that, for the K-edge, the allowed transition or the final state consists of p ($\lambda' = 1$) symmetry, the $L_{2,3}$-edge probes the d ($\lambda' = 2$) or s ($\lambda' = 0$) empty states, and $M_{4,5}$ edges probe the f ($\lambda' = 3$) symmetry.[156]

2.5 Orientation Dependent XANES

The X-rays obtained from synchrotron radiation is already plane polarized or else can be tuned by the undulators. Linearly polarized light is utilized to study anisotropy in bonding and charge distribution which involve relative orientation of atomic orbitals. This technique has been widely used to understand orientation of the molecular nanomaterials. In order to obtain linear dichroism, the X-ray polarization vector has to satisfy the equation $3\cos^2\theta^* = 1$, where θ^* is the angle between the sample normal and the X-ray polarization vector, which is called the magic angle ($\theta^* \approx 54.7°$).[157]

The transition matrix element in eq 2.5 within the dipolar approximation transforms into a second rank tensor,[157]

$$\mu(\omega) = 4\pi^2\alpha\hbar\omega \sum_{i,f} \left(\frac{1}{d_i}\right) |\langle\psi_f|\hat{\epsilon}\cdot\vec{r}|\psi_i\rangle|^2 \delta(E_f - E_i - \hbar\omega) = \sum_{j,k} \hat{\epsilon}_j \hat{\epsilon}_k M_{jk} \qquad (2.6)$$

where, $\hat{\epsilon} = (\sin\theta\cos\phi, \sin\theta\sin\phi, \cos\theta)$ is the X-ray polarization vector expressed in spherical polar coordinates θ, ϕ, and M is the absorption tensor. One can obtain the following

expression by expanding the above eq 2.6,

$$M_{11}\sin^2\theta\cos^2\phi + M_{22}\sin^2\theta\sin^2\phi + M_{33}\cos^2\theta + 2(M_{12}\sin^2\theta\sin\phi\cos\phi + M_{31}\sin\theta\cos\theta\cos\phi + M_{23}\sin\theta\cos\theta\sin\phi) \quad (2.7)$$

and the eq 2.7 assumes that $M_{jk} = M_{kj}$, satisfies the symmetric condition. M can be diagonalized by choosing the appropriate coordinate system. Rotating the tensor through an angle $^{2\pi}/_{N}$ and equating to a non-rotated tensor confirms that for $N > 2$, the tensor element will become diagonal, and $M_{11} = M_{22}$.[146] Therefore the absorption cross-section,

$$\mu(\omega) \propto M_{11}(\sin^2\theta) + M_{33}(2\cos^2\theta) \quad (2.8)$$

and the eq 2.8 becomes independent of ϕ. Also, a two-fold rotation axis satisfies symmetric conditions $M_{23} = M_{32} = 0, M_{13} = M_{31} = 0$. If the sample has cubic symmetry, absorption is isotropic and independent of orientation.

For K-edges, eq 2.8 will be reduced to $\cos^2\theta$, and $\sin^2\theta$ dependency diminishes at energies above the edge, as predicted by calculations. However, $\sin^2\theta$ plays a role in L-edge XANES.[146,157]

2.6 X-ray Magnetic Circular Dichroism Spectroscopy

The magnetic properties in transition metal elements arise from partially filled $3d$ states. Therefore, it is beneficial to probe the d states by exciting the $2p$ core electrons. According to selection rules, the L-edge XAS involves both $p \rightarrow d$ and $p \rightarrow s$ transitions, out of which $p \rightarrow d$ dominates by a factor greater than 20.[154] From the orbital picture, a p orbital is two-fold degenerate, therefore two prominent peaks, $p_{3/2}$ (L_3) and $p_{1/2}$ (L_2), are observed and their intensity is directly proportional to the number of d holes. The magnetic properties in d-block elements arise from the decreasing number of holes (N) as we go from Ni-Fe. The spin magnetic moment is due to the exchange interaction between the number of spin-up and spin-down holes, $m_s = -\frac{2\mu_B}{\hbar}\langle S_z\rangle$. The orbital moment is $m_o = -\frac{\mu_B}{\hbar}\langle L_z\rangle$ and it originates from the spin-orbit coupling, which is significantly smaller compared to the exchange interaction.[158,159]

The magnetic properties of solids arise from angular momentum of electrons (spin and orbital) and can be probed using circularly polarized light. The use of undulators enable the production of X-rays with different polarizations, and use of X-rays in magnetic studies has several advantages. The XMCD technique is element specific and quantitative in

determination of spin and orbital momentum and their anisotropies, which is not possible by traditional magnetic techniques. The physics behind XMCD technique can be understood through the following two steps.

The right and left circularly polarized light have angular momentum, $+\hbar$ and $-\hbar$ respectively. The first step is transfer of photon angular momentum to an excited photoelectron of an element in the sample. The photon momentum can be transferred to an excited photoelectron, if it has both spin and orbital angular momentum (spin-orbit coupling), as spin does not interact directly with the electric field of incoming photons. The right circularly polarized (RCP) light transfers angular momentum to spin of one orientation, whereas left circularly polarized (LCP) light transfers to spin of the opposite orientation. As mentioned above, a p-orbital is two fold degenerate with opposite spin-orbit coupling, $(l + s)$ $(p_{3/2})$ and $(l - s)$ $(p_{1/2})$, respectively. Hence, this results in two white lines with differing intensity ("dichroism"). Spin-up or Spin-down are defined with respect to photon helicity.

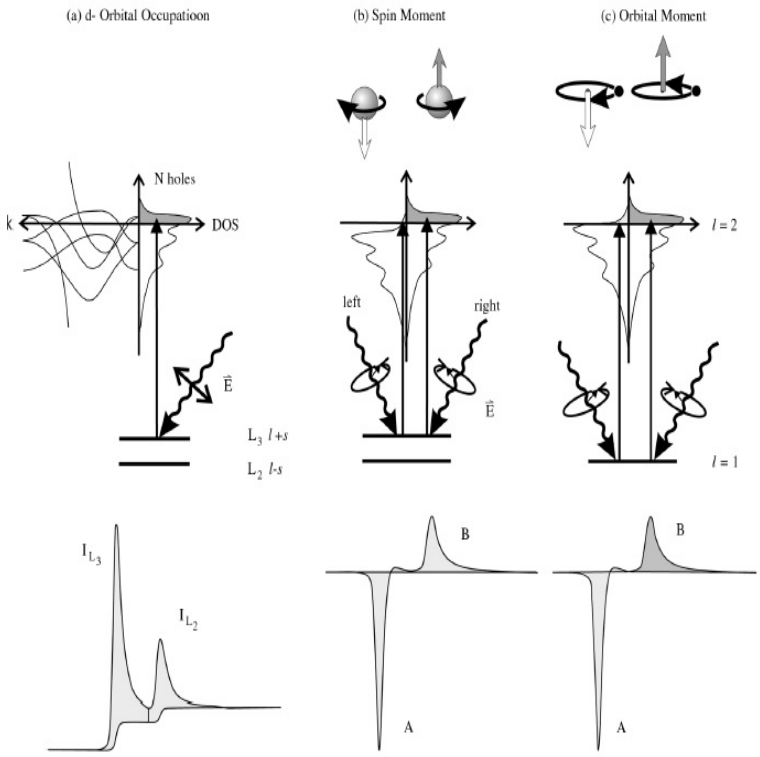

Figure 2.2: Schematics of XMCD for a one electron system. (a) Electronic structure of the L-edge transition levels in XAS. (b) and (c) XMCD effect originating from the spin and orbital moment of the electron respectively. XMCD intensity is directly proportional to the number of d holes. The spin and orbital momentum can be extracted from the area under the curve as explained in the text.[158†]

Secondly, maximum XMCD intensity is observed when the photon spin angular momentum is collinear with the magnetization direction of the sample. The spin-split empty valence states act as a spin detector for the excited photoelectrons. Due to imbalance in spin-up and spin-down DOS in magnetic materials, $L_{2,3}$ XANES for LCP and RCP give variation in intensity and the difference is the measured XMCD. As depicted in Figure 2.2b, the XMCD signal has main peaks A and B with opposite signs; this is the indication of opposite spin-orbit coupling in $p_{3/2}$ and $p_{1/2}$ levels. d-electrons also possess orbital angular momentum, hence valence states acts as orbital momentum detectors for the excited electron

†Reprinted from J. Magn. Magn. Mater., Vol. 200, J. Stöhr, Exploring the microscopic origin of magnetic anisotropies with X-ray magnetic circular dichroism (XMCD) spectroscopy, pp. 470-497, Copyright (1999), with permission from Elsevier.

(Figure 2.2c).[158,159] The quantification of spin and angular momentum is obtained separately using the famous XMCD sum rules.

The electric dipole approximation used to obtain the absorption cross section in eq 2.5 does not contain any spin dependent terms, and if the sample has net magnetic moment, the initial and final state wave functions in eq 2.5 is no longer invariant upon time reversal and depends on the magnetization direction. In an XMCD experiment, a magnetic field is applied parallel to the photon direction and collinear with the magnetization axis of the sample; cross section does not depend on $\boldsymbol{k}$-vector of photons. The electric field vector for the LCP is $\epsilon_L = \sqrt{2}\,(1/2, i/2, 0)$ and the complex conjugate of LCP is the electric field vector for RCP.[154] The absorption cross section considering magnetic effect is,

$$\mu_{L,R}(\omega) = 4\pi^2\alpha\hbar\omega \sum_{i,f} \left(\frac{1}{d_i}\right) |\langle\psi_f|\hat{\epsilon}_{L,R}\cdot\vec{r}|\psi_i\rangle|^2 \delta(E_f - E_i - \hbar\omega) \tag{2.9}$$

The difference $\mu_R(\omega) - \mu_L(\omega)$ is a measure of the XMCD effect and it is non-zero if the sample has a net magnetic moment.

XMCD sum rules. One of the main strengths of XMCD is that spin and orbital moment can be quantitatively obtained; extraction of orbital moment is useful in predicting magnetocrystalline anisotropy. Thole *et al.*[160] derived magneto-optical sum rules for XMCD to estimate orbital and spin magnetic moment from XANES and XMCD spectra.[161]

The effective orbital and spin moment can be obtained using the following equations:[162]

$$m_o = -\frac{4\int_{L_3+L_2}(\mu_+ - \mu_-)\,d\omega}{3\int_{L_3+L_2}(\mu_+ + \mu_-)\,d\omega}\,(10 - n_{3d}) \tag{2.10}$$

$$m_s = -\frac{6\int_{L_3}(\mu_+ - \mu_-)\,d\omega - 4\int_{L_3+L_2}(\mu_+ - \mu_-)\,d\omega}{\int_{L_3+L_2}(\mu_+ + \mu_-)\,d\omega} \times (10 - n_{3d})\left(1 + \frac{7\,\langle T_z\rangle}{2\,\langle S_z\rangle}\right)^{-1} \tag{2.11}$$

where m_o and m_s are orbital and spin magnetic moment in units of μ_B/atom, respectively. The n_{3d} is the $3d$ electron occupation number for the specific TM atom. L_3 and L_2 are the integration range. $\langle T_z\rangle$ is the expectation value of magnetic dipole operator, which is usually neglected during calculations. However, it plays an important role in calculating anisotropic spin density. $\langle S_z\rangle$ is equal to half of m_s in Hartree atomic units. The denominator in both eq 2.10 and eq 2.11 is approximated from the isotropic spectrum $(\mu_R + \mu_L + \mu_0)/3$ by neglecting the contribution from linear polarization μ_0.[154]

2.7 STXM Imaging

The scanning transmission X-ray microscopy (STXM) measurements were conducted at the Soft X-ray Spectromicroscopy (SM) beamline (10ID-1), at the Canadian Light Source Inc. (CLS). STXM allows for X-ray imaging of the specimen with 30 nm spatial resolution. The details of the instrument configuration have been described elsewhere.[163] Third generation synchrotron light was obtained using an APPLE-II elliptically polarized undulator (EPU).

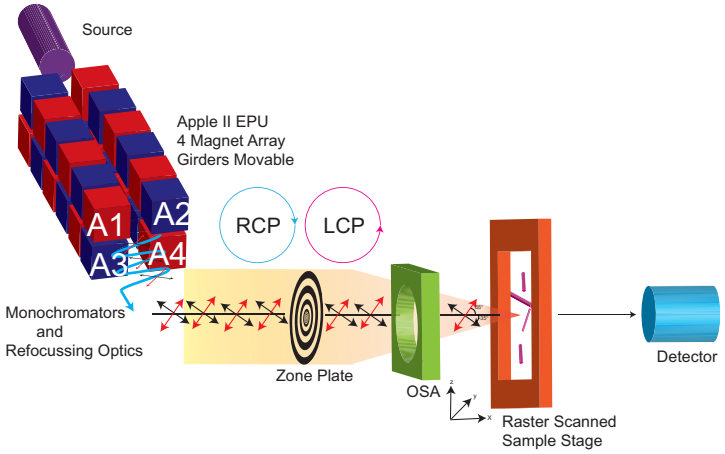

Figure 2.3: Schematic of the STXM set up. The circular and linear polarized X-rays were obtained by setting the proper undulators. The polarized X-rays were passed through a zone plate and an order sorting aperture (OSA) and then focused on the sample plane. The raster scanned images were obtained at each energy point and an image stack was generated.

A monochromatic X-ray beam was focussed to a small X-ray spot using a zone plate and the focal spot size is set by the width of the outer most zones in the zone plate. An order sorting aperture (OSA) is used in conjunction with a thick central zone to block zero and higher order radiation. The raster scanned image was obtained from the sample at each energy point and the image stack was generated. The measurement was done in transmission mode. The schematic of the STXM instrument is shown in Figure 2.3.

2.7.1 XMCD Measurements

Mn $L_{2,3}$-edge XANES in $Ga_{1-x}Mn_xN$ NWs

For XAS measurements in the STXM mode, the NWs were deposited on a silicon nitride window from a dilute suspension in ethanol. Image stacks were collected for different energies from 633-660 eV (Mn $L_{2,3}$-edge) at room temperature (300 K). The circularly polarized light from the undulators were obtained by symmetric and synchronised motion of the diagonally opposite magnetic arrays. For XMCD measurements, the NWs were well dispersed in methanol by sonicating about 3-5 s and deposited on a TEM grid. The grid was sliced into equal parts under optical microscope and a part of the sliced grid was fixed on the non-magnetic rod using epoxy, and mounted between the poles of a small permanent magnet having the magnetic field strength of approximately ∼0.1 T. This set up was inserted in the STXM chamber, and the sample stage was rotated 30° relative to the sample plane, which allows a fraction of magnetic field to be parallel to the incoming X-ray beam. The STXM image was collected at each energy point, switching undulators alternatively in order to generate the left and right circularly polarized light, and the image stack was generated. The data was collected in transmission mode.

2.7.2 Linear Polarization Measurements

Ga L-edge and O K-edge XANES in Ga_2O_3 NWs

APPLE-II EPU can produce 100% linearly polarized light and was obtained by moving magnetic arrays A1 and A4 in opposite direction. The polarization angle of the electric field vector (E) can be continuously rotated from -90° to +90°. For these measurements, NW samples were dispersed in methanol by sonication, and then deposited on the silicon nitride window using a micropipette. The X-ray image was collected at each energy point. The magic angle was obtained to satisfy the $3\cos^2\theta^* = 1$ relation by subtracting $180 - \theta^*$, where θ^* is the angle between sample normal and incident X-ray polarization vector.

2.7.3 Data Analysis

The data analysis was done using Axis-2000 software. The image stack from the STXM was aligned using Jacobson analysis software. The optical density (OD) of the aligned stack was obtained using the expression $\ln(I/I_0)$, where I is the transmitted intensity from the

image area containing the specimen of interest, and I_0 is the intensity corresponding to the area that contains no specimen. The final NW spectra were obtained from the masked image analysis, which is useful in quantifying the absorption intensity in an area of interest.

2.8 Simulation of XANES Spectra

2.8.1 Multiplet Calculations for Mn L-edge

The single particle approximation to explain XAS holds well for explaining K-edges, but it gives poor agreement in the case of metal $L_{2,3}$-edges. The reason for such a discrepancy is due to the strong overlap of the core wave function with the final state wave function. In order to derive the spectra from a strongly correlated electron system, the first step is to consider the case of an isolated atom, without any interatomic effects. The Hamiltonian can be written by considering the electron-electron repulsive term, and the electron-nucleus Coulomb attractive term along with spin-orbit coupling,[164,165]

$$H = \sum_N \frac{p_i^2}{2m} + \sum_N \frac{-Ze^2}{r_i} + \sum_{pairs} \frac{e^2}{r_{ij}} + \sum_N \zeta(r_i) l_i \cdot s_i \tag{2.12}$$

The first two terms define the average energy (H_{av}), which is same for all electrons in a given atomic configuration. The last two terms electron-electron repulsion (H_{ee}) and spin-orbit interaction (H_{ls}) determine the different terms within the atomic configuration.

Term Symbols

The orbital momentum L, spin momentum S and total angular momentum J are called term symbols for a given configuration. The L and S are $(2L+1)$ and $(2S+1)$ fold degenerate, respectively. Both L and S have the same energy in the absence of spin-orbit interactions. If there is a spin-orbit coupling L and S have different energies and split depending on the J value. J can have a value between $|L-S| \leq J \leq L+S$ with a degeneracy $2J+1$. A term symbol is represented as ${}^{2S+1}X_J$, where X = S, P, D, F for $L = 0, 1, 2, 3$, respectively. For example, ${}^2S_{1/2}$ corresponds to a single s electron with spin 1/2. For a single p-electron it will be ${}^2P_{1/2}$ and ${}^2S_{3/2}$ configurations.

The outermost electronic configuration of a TM element is $3d^N$ and in the final state it will be $3d^N + 1$ along with a $2s$ or a $3p$ core hole.[165,166] In the case of a d-orbital with electron occupancy 2 ($3d^2$), Pauli's exclusion principle forbids electrons to have same

quantum numbers and 45 combinations are possible. Similarly, the ($3d^2$) configuration has 120 different states. Therefore, a general formula for the degeneracy for $3d^N$ configuration is,

$$\binom{10}{N} = \frac{10!}{(10-N)!N!}$$

The $L_{2,3}$-edge involve $2p \rightarrow 3d$ transitions, therefore it is essential to understand the term symbols for the $2p^6 3d^N$ electronic configuration. It can be determined by multiplying configurations of $3d^N$ with ^2P term symbol. The total degeneracy of the $2p^6 3d^N$ is six times the degeneracy of $3d^N$ configuration.[165]

The term symbol deals with only symmetry elements of $3d^N$, and does not give any information about relative energy of the system. Relative energies of the different terms can be described through matrix elements considering the electron-electron repulsion H_{ee} and spin-orbit interaction H_{ls}. The angular and radial part of the direct Coulomb repulsion and exchange interaction can be explained through Slater-Condon parameters F_k and G_k, respectively. The matrix element for the electron-electron interaction is,

$$\left\langle {}^{2S+1}L_J \left| \frac{e^2}{r_{12}} \right| {}^{2S+1}L_J \right\rangle = \sum_k (c_{ik}F_k + d_{ik}G_k) \tag{2.13}$$

The $3d^N$ configuration contains c_0, c_2, and c_4 Slater-Condon parameters. The final state $2p^5 3d^{N+1}$ configuration contains c_0, c_2, c_4, g_1, and g_3 Slater-Condon parameters.[165,167]

XAS Equation for Multiplets

As mentioned, L-edge XANES involves probing the partially filled $3d$ states. The energies of the final states are affected by the $2p$-$3d$ Slater-Condon parameters. The empty $3d$ shell transition is described as $2p^6 3d^0 \rightarrow 2p^5 3d^1$. The ground state has $^1S_0$ symmetry and the final state symmetries are, $^1P_1$, $^1D_2$, $^1F_3$, $^3P_{012}$, $^3D_{123}$ and $^3F_{234}$. The X-ray absorption intensity is,

$$I_{XAS} \propto \left\langle 3d^0_{[^1S_0]} \left| \vec{r}_{[^1P_1]} \right| 2p^5 3d^1_{[^{1,3}PDF]} \right\rangle^2 \tag{2.14}$$

There are 12 term symbols or final states and transition is forbidden if they have the same J value. Only dipole allowed transitions are possible $\Delta J = 0, \pm 1$, also within spin-orbit coupling $\Delta S = 0$ and $\Delta L = 1$. Therefore, the dipole selection rule reduces the number of final states.[164–167]

Crystal Field Effect

As an atomic multiplet spectrum arises due to the dipole allowed transition between the initial state multiplet and all final states (term symbols), there will be a significant core-hole wave function overlap, leading to spectral broadening. One of the most important effects that significantly changes the final spectral shape is the crystal field effect, which arises due to the central atom interacting with surrounding ligands. This interaction reduces spherical symmetry of the system, thereby lifting degeneracy of the d-orbitals.[168] This effect is successful in explaining the origin of peaks in optical spectra, electron paramagnetic resonance (EPR) and X-ray absorption spectra. In most crystal systems, the TM atom is surrounded by six neighbouring atoms, and this is called octahedral (O_h) or quasi-octahedral symmetry.

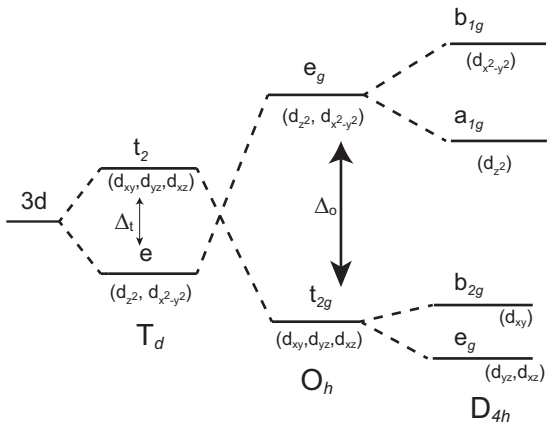

Figure 2.4: Illustration of $3d$-orbital splitting in various site symmetries. $3d$-orbital in spherical symmetry with no splitting, followed by $3d$-orbital splitting in tetrahedral (T_d), octahedral (O_h) and tetragonal (D_{4h}) symmetry. The splitting will cause various energy arrangements of the $3d$-orbitals.

The metal-ligand electrostatic interaction will cause splitting of $3d$-orbitals into triply degenerate t_{2g} (lower energy) and doubly degenerate e_g (higher energy) configurations. The extent of splitting between t_{2g} and e_g is denoted by splitting energy Δ. The e_g orbitals are directed towards the anions, raising their energies, whereas the t_{2g} orbitals are delocalized over the three metal ligand planes and thus their energies are reduced. More branching or splitting arises as the symmetry is reduced and magnitude of the crystal field splitting depends on electronic state, coordination number and point group of the TM, and nature

of the coordinating anions. Figure 2.4 illustrates the splitting of $3d$-orbitals in different site symmetry. The splitting of d-orbital in tetrahedral symmetry (T_d) gives rise to t_2 and e levels and have less crystal field strength compared to O_h symmetry. Similarly, for tetragonal distortion (D_{4h}) one can see more splitting. In general, these terms can be obtained from the optical spectroscopy measurements.[164,165,168]

In this work, Mn $L_{2,3}$-edge multiplet calculations in $Ga_{1-x}Mn_xN$ NWs were done using the CTM4XAS-5.5 package,[169] including the spin-orbit coupling term, crystal field splitting (10 Dq), and Slater integral reduction terms (F_{dd}, F_{pd} and G_{pd}) at 300 K, as input parameters. The default values of the spin-orbit and Slater integral reduction parameters were used. The calculations were performed for a 10 Dq value of 0.5 eV and same value was used for both Mn^{2+} and Mn^{3+} oxidation states in T_d symmetry.[170] The front panel of CTM4XAS is shown in Appendix C (Figure C.1).

2.8.2 Multiple Scattering Theory for O K-edge XANES

Theoretical calculations were performed in the framework of the multiple scattering (MS) theory using FDMNES code.[171] This approach makes use of the Green function formalism with a muffin-tin (MT) potential, and allowed the caculation of XANES spectra for the O K-edge and the corresponding angular momentum projected density of states (PDOS) for specific orbitals.

The final state $\langle\psi(f)|$ in eq 2.5 is obtained by considering all elastic scattering paths of the emitted electron with nearest neighbors before coming back to the initial absorbing atom, as the basis for the multiple scattering theory.[156] The atomic scattering centers are provided by the MT potential,[156,171] and it consists of a central absorbing atom surrounded by a set of N number of atoms (Figure 2.5).

The MT approximation assumes that an aggregation of atoms is isolated from its environment. In order to calculate the final state wave function, building the global potential is essential in the first approximation. The universally accepted MT potential, where the region-III is made up of spherical potentials, is constantly varying, while region-II (inter atomic) and region-I (outer potential) are constant. The contribution from region-II and region-I have negligible effect as they add only a constant shift to the final energy of the absorption structures, and have tiny potential difference. Region-III is spherically symmetric and provides atomic scattering centres that are described by atomic phase shifts, which are calculated by assuming spherically symmetric potentials inside the MT. The Green function propagators are used to connect these scattering centers.

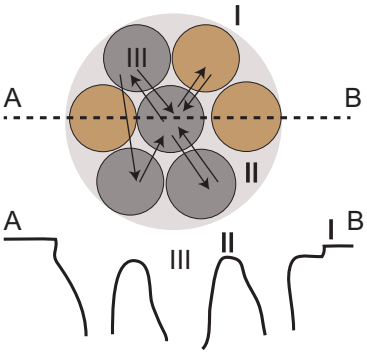

Figure 2.5: Muffin tin (MT) potential for the isolated aggregate of atoms. Region-III is the spherical potential. Region-II (inter atomic region) and I (outer region) with constant potential. Below is the variation of potential along the AB-line. The full wave multiple scattering accounts for the final X-ray spectrum arising from all the scattering paths (black arrows) for the photoelectron, starting and terminating at the central atom.

The X-ray absorption cross-section μ in eq 2.5 derived from Fermi's golden rule can be written in the form of projected photoelectron density of the final states or is equivalent to the imaginary part of the one particle Green function, $G = (E - H + i\Gamma)^{-1}$. The Green function incorporates inelastic losses and other quasiparticle effects and avoids any further explicit approximations to the final state wave function. These approximations in the Green function make it useful to formulate XAFS theory. The spectral representation of the Green function in position space is,[156]

$$G(r, r'; E) = \sum_f \frac{\psi_f(r')\psi_f^*(r')}{(E - E_f + i\Gamma)} \tag{2.15}$$

where ψ_f are the effective final state wave functions with energies E_f with a one-particle Hamiltonian H including appropriately screened core hole potential, and Γ is a net life time of the core hole. The modified general expression for the absorption cross-section including the Green function formalism is given by,[156,172]

$$\rho(\omega) = 4\pi^2 N_0 \hbar\omega \left[(l+1)M_{l,l+1}^2 X_{l+1} + lM_{l,l-1}^2 X_{l-1}\right] \tag{2.16}$$

where N_0 is the free electron density of state, l and $l \pm 1$ are the angular momentum of the initial and final state, respectively, obeying the dipole selection rule. The transition matrix element M links the initial and final state of the ejected electron, $M_{l,l+1} = \int r^3 dr R_{l+1}\phi_i(r)$, and can be renormalized by $\sin^2 \delta_l^0$, which corresponds to the imaginary part of the phase

shift induced during multiple scattering events. The X term contains the Green function propagator given by,

$$X_l = \frac{1}{2l+1}\frac{1}{\sin^2\delta_l^0}\sum Im\left[(I + T_a \cdot G)^{-1} \cdot T_a\right]^{0,0}_{lm,lm} \tag{2.17}$$

where T_a is the matrix that describes the scattering by atomic scattering centers and I is the unit matrix. Im is the imaginary part of the matrix element summed over l and m. Inversion of the matrix element in eq 2.17 indicates XANES spectra can be calculated in the extended X-ray absorption fine structure (EXAFS) region. Another advantage of MS formalism is, the imaginary part of G is the density matrix, and the absorption in eq 2.17 of the final states given in the form of angular momentum l. It implies that the absorption cross-section can be directly correlated to angular momentum projected density of states of the $\rho'_l(E)$ of the final state. However, the interpretation of XANES spectra based on the PDOS must be done carefully as final states are affected by core-hole effects, lifetime broadening or energy shifts.[156]

The transition matrix element in eq 2.3 $\left|\left\langle \phi(f)\left|\hat{E}\cdot\hat{r}\right|\phi(i)\right\rangle\right|^2$ can be reduced to $\cos^2\theta$ (detailed derivation explained in Sec. 2.5), where θ is the angle between the electric field vector E and a reference direction (in this study the long axis of the NWs).

As the first step in the calculation, optimal MT radii were found by increasing the number of atoms in the cluster using Norman procedure. The MT sphere overlap was set to 10%, and the real Hedin-Lundquist exchange correlation potential was used. The details of the FDMNES code and corresponding keywords are explained in Appendix H. The spectral broadening, which depends on the core level and final state widths, was calculated by convoluting the arctangent function (Γ),[173] commonly used to account for energy-dependent broadening,

$$\Gamma = \Gamma_{hole} + \Gamma_m\left(\frac{1}{2} + \frac{1}{\pi}\arctan\left(\frac{\pi}{3}\frac{\Gamma_m}{E_{Larg}}\left(e - \frac{1}{e^2}\right)\right)\right) \tag{2.18}$$

where Γ_{hole} and Γ_m are core-level width and maximum width of the final state, respectively. The term e is defined as $e = {}^{E-E_F}/_{E_{cent}}$, where E_{cent} is the center of the arctangent function.[173] The depth at the center of the arctangent is given as ${}^{\Gamma_m}/_{E_{Larg}}$ where E_{Larg} is the width of the function. For O K-edge, $\Gamma_{hole} = 0.16$, $\Gamma_m = 30$, $E_{cent} = 60$, and $E_{Larg} = 30$ eV were used to convolute the raw spectra.

2.9 Fabrication of $Ga_{0.95}Mn_{0.05}N$ Nanowires

The Mn doped GaN NWs were transferred by gently pressing the nanowire substrate to the device substrate (SiO_2/Si). The schematic of the nanowire device is shown in Figure 2.6. The electrical contacts on the transferred wire were defined using electron beam lithography technique. The patterned substrate was dipped inside hydrofluoric acid for 5 s to remove any native oxide. Finally metal contacts Ti/Au (30/50 nm) was deposited through electron beam evaporation. The magneto-conductance measurements on the single $Ga_{0.95}Mn_{0.05}N$ NWs were performed in a four-probe configuration using lock-in amplifier. A bias voltage (V_B) of 2 mV was applied between the metal contacts and magnetic field (B) was applied perpendicular to the nanowire long axis.

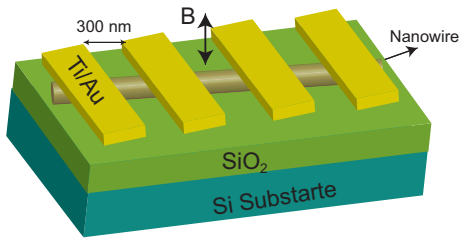

Figure 2.6: Schematic of the nanowire device. $Ga_{0.95}Mn_{0.05}N$ NWs were transferred to the device substrate by dry pressing. The contacts were defined using electron beam lithography and Ti/Au electrodes were deposited using electron beam evaporation. The distance between electrodes is 300 nm. The magnetic field was applied perpendicular to NW long axis. A bias voltage of 2 mV was applied across the electrodes. The conductance was measured as a function of magnetic field in a four-probe configuration using lock-in amplifiers.

Chapter 3

Structural Characterization and Electronic Structure of Mn Doped GaN Nanowires

This chapter deals with growth and characterization of Mn doped GaN NWs, which were synthesised using CVD. The effect of Mn dopant incorporation on growth of individual GaN NWs was studied in detail at the atomic structure level by the use of high-angle annular dark-field (HAADF) scanning transmission electron microscopy (STEM). The oxidation state and electronic structure of Mn in GaN at the single NW level was studied using STXM. The experimental results in combination with calculations enabled this work to quantitatively estimate the Mn speciation in individual NWs, which is essential to understanding the carrier mediated ferromagnetism in DMS materials.

3.1 Structural Characterization

3.1.1 Crystal Structure and Morphology

GaN has a wurtzite crystal structure with a space group $P6_3mc$ with lattice parameters, $a = b = 3.1937\,\text{Å}, c = 5.207\,\text{Å}, \alpha = \beta = 90°$, and $\gamma = 120°$ (Figure 3.1).[174] In wurtzite undoped GaN lattice even without Jahn-Teller effect, Ga atoms reside in distorted tetrahedrally (T_d) coordinated with N atoms. In ideal wurtzite lattice ligands have C_{3v} symmetry within the tetrahedron. Doping with Mn will replace the Ga sites (substitutional doping).

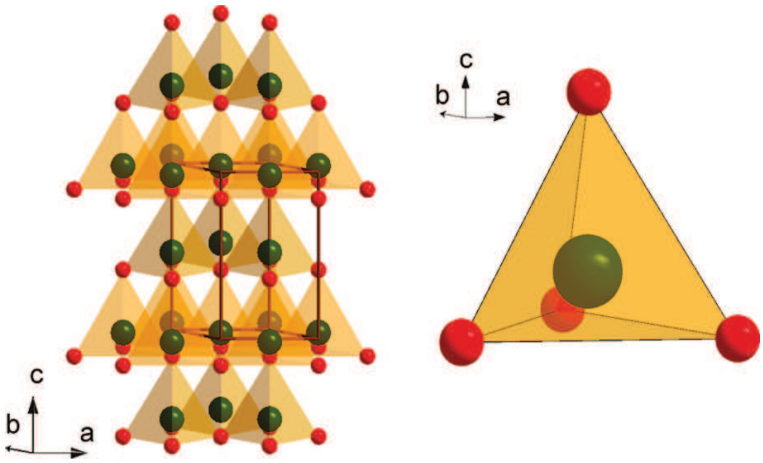

Figure 3.1: Crystal structure of wurtzite GaN showing a unit cell (left) and the coordination of a gallium ion site (right). Ga atoms are shown as green and N as red spheres. The orientation of the unit cell is shown with respect to crystal coordinate system.

Manganese-doped GaN NWs were synthesized by chemical vapor deposition (CVD), using Mn starting concentration of 10 atom % ([Mn]/[Ga] $\approx$ 0.10). Figures 3.2a and 3.2b show the XRD pattern and SEM image of GaN NWs synthesized at 950 °C, respectively. The nanowires were obtained in a relatively high yield on the growth substarte, and the XRD pattern is readily indexed to wurtzite GaN. The analogous data for Mn doped GaN NWs, using Mn starting concentration of 10 atom % are shown in Figures 3.2c and 3.2d. The doped NWs retained the wurtzite crystal structure; however, compared to undoped NWs, they were produced in a lower yield, which can be attributed to the inhibition of NW growth due to adsorption of dopant ions on NW surfaces and edges. Figure 3.2e is the high resolution TEM image of the single nanowire, confirm the high crystallinity of the NW and the growth direction along the $\langle 10\bar{1}0 \rangle$. The lattice spacing of 2.74 Å (Figure 3.2e) corresponds to wurtzite lattice as confirmed from the previous studies.[113,175]

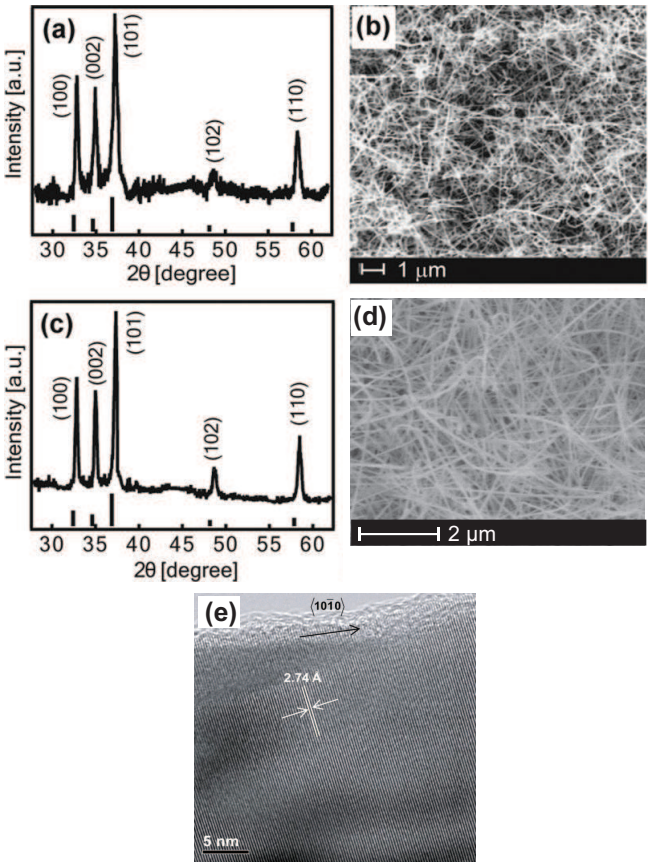

Figure 3.2: (a) and (b) XRD pattern and SEM image of undoped GaN NWs. (c) and (d) XRD pattern and SEM image of Mn doped GaN Nws. The vertical lines in (a) and (c) indicate XRD pattern of bulk wurtzite GaN. (e) HRTEM image of triangular cross section of the single NW with lattice spacing and growth direction.

3.1.2 Atomic-level Structure of Mn Dopants in GaN Nanowires

The structure and growth direction of individual NWs was further studied by HAADF-STEM imaging and it confirm NWs grew along $\langle 10\bar{1}0 \rangle$ direction (Figure 3.3a), as reported in previous studies.[175] The HAADF-STEM technique is sensitive to changes in the atomic number (Z) within the specimen and is often referred to as Z-contrast imaging. Due to a significantly higher Z value of Ga with respect to N, only Ga sites are directly observed. Horizontally elongated spots in the image correspond to two Ga^{3+} sites separated by 0.6 Å (Figure 3.3b). This dumbbell structure characteristic for wurtzite GaN remains intact upon

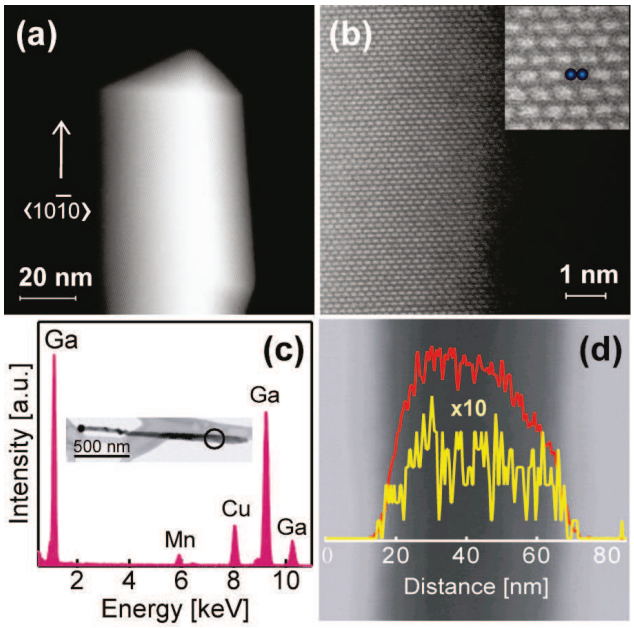

Figure 3.3: (a) STEM image of $Ga_{0.95}Mn_{0.05}N$ nanowire showing triangular cross section. (b) HAADF-STEM image of $Ga_{0.95}Mn_{0.05}N$ nanowire from part (a). Inset: magnified section of the image showing characteristic dumbbell structure consisting of pairs of Ga atoms separated by 0.6 Å. The positions of Ga atoms are indicated with blue spheres. (c) EDS spectrum of a typical $Ga_{0.95}Mn_{0.05}N$ nanowire. The nanowire region corresponding to the spectrum is designated with a circle in the inset. Mn doping concentration is determined to be $4.5 \pm 0.3\%$. (d) EDS elemental line scan profile of the nanowire in (c), indicating very similar Mn (yellow) and Ga (red) profiles. The line profiles are overlapped on the nanowire image. Mn profile is multiplied by a factor of 10 for clarity.

Mn incorporation. Importantly, careful inspection of HAADF STEM images convincingly demonstrates the absence of secondary phases in these NWs. The average doping concentration was determined by EDS analysis to be 4.5 ± 0.3 atom % (Figure 3.3c). EDS elemental line scan profile of the same NW recorded perpendicular to the growth direction is shown in Figure 3.3d. The line scan profile of Mn is in good agreement with that of Ga, indicating largely random distribution of Mn across the NW.[175] Although $Ga_{0.95}Mn_{0.05}N$ NWs obtained by the CVD method under the given conditions can practically be considered homogeneously doped, note that, at some places along the NW, Mn profile may be slightly lower in the middle of the NW relative to Ga. This is occasionally observed close to the NW tips and is associated with the doping mechanism involving binding of Mn intermediates to

the NW surfaces (vapor-solid rather than vapor-liquid-solid doping mechanism).[114,175]

3.2 Electronic Structure of Mn Doped GaN Nanowires

3.2.1 Ga L-edge and N K-edge XANES

Figure 3.4a and 3.4b shows the XANES spectra of Ga L_3-edge and N K-edge, respectively, from a single $Ga_{0.95}Mn_{0.05}N$ NW. Ga L_3-edge XANES probes the empty d and s orbital-derived states. Ga L_3 edge XANES spectra do not show any significant photon incident angle dependence, which indicates that conduction band is predominantly made up of s-like orbitals.[176,177]

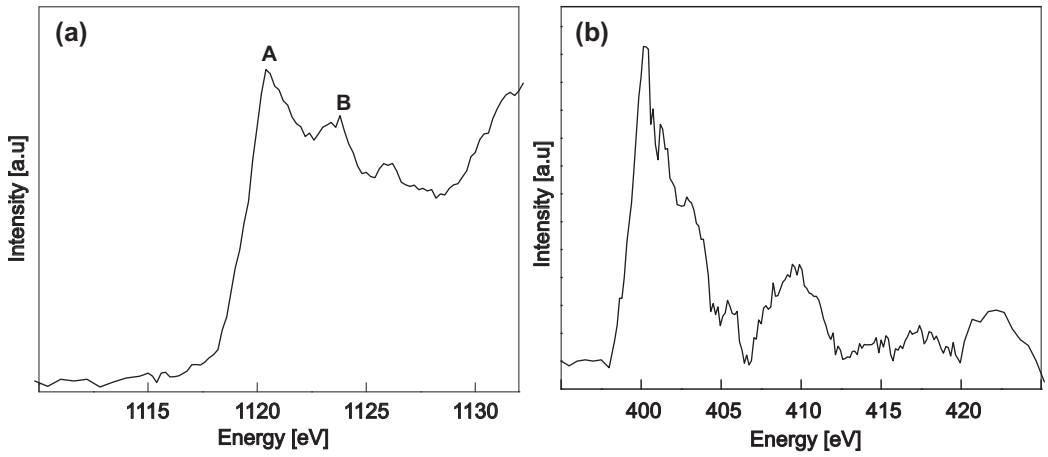

Figure 3.4: (a) Ga L_3-edge and (b) N K-edge spectra of individual $Ga_{0.95}Mn_0.05N$ NWs, confirming their wurtzite crystal structure.

The linear muffin tin orbital (LMTO) density functional theory calculations further reveal that the conduction band minima do not have much contribution from the Ga d orbitals.[178] The conduction band is made up of a majority of Ga $4s$ and $4p$ states, while the valance band contains a small fraction of Ga $4s$ and $4p$ orbitals. The peaks labeled A and B in the Ga L_3-edge spectrum (Figure 3.4a) are characteristic for Ga^{3+} in the wurtzite GaN.[176] Feature A is mainly due to Ga $4s$ orbitals. The band B arises from the mixture of Ga $4s$ state and higher energy s or d orbital containing states projected on the Ga^{3+} ion.[177]

Further insights into the electronic structure of the conduction band could be provided by complementary Ga K-edge spectra. Similarly, nitrogen K-edge spectrum (Figure 3.4b) also coincides with the spectrum reported for the GaN wurtzite lattice.[179,180] Both Ga L_3-edge and N-K edge spectra of individual NWs in Figure 3.4 confirm that the wurtzite lattice remains intact upon Mn doping.

3.2.2 Mn $L_{2,3}$-edge XANES

Figure 3.5a (inset) shows a STXM image of typical NWs, collected using 633 eV X-ray beam. The absorption spectrum of a particular sample area at a given element edge is reconstructed from the stack of images by monitoring the transmitted intensities for different photon energies. Mn $L_{2,3}$-edge spectra corresponding to the selected NW areas are shown with analogous colors in Figure 3.5a. The structured asymmetric peak centered at approximately 640 eV can be assigned to L_3-edge (predominantly $p \rightarrow d$ in character) and the lower intensity feature centered at ~651 eV to L_2-edge absorption. Both spectra are very similar, indicating high wire-to-wire uniformity in Mn ion speciation (see Appendix D, Figure D.1). Theoretical modeling of the Mn K-edge X-ray absorption spectra has suggested that the substitutional model with Mn dopants on Ga^{3+} sites best simulates the experimental data.[181] This finding is consistent with the extensive density functional theory calculations,[37] which have predicted that the formation energy of the substitutional Mn in GaN is significantly smaller (by 5-7 eV) than the formation energies of interstitial octahedral (O_h) or tetrahedral (T_d) Mn species.

Furthermore, the L-edge spectra corresponding to interstitial Mn in GaN are expected to be significantly different from substitutional (simple or neighboring N split interstitial) sites.[182] Therefore in $Ga_{1-x}Mn_xN$ NWs substitutional sites as the most likely form of Mn incorporation. To further understand the nature of the doping sites and the Mn oxidation state, the STXM L-edge data was analysed with respect to the theoretical spectra for Mn^{2+} and Mn^{3+} in T_d coordination calculated by configuration-interaction (CI) cluster-model method.[183] The red and purple traces in Figure 3.5b represent the $L_{2,3}$-edge spectra of T_d Mn^{2+} and Mn^{3+}, respectively. While the general features of these two spectra are similar, there is a significant structural difference, particularly in the L_2 region, which has a multiplet structure for Mn^{3+}.[183]

The similarity between the Mn $L_{2,3}$-edge spectra of single $Ga_{0.95}Mn_{0.05}N$ NWs and the simulated spectra indicates that Mn ions are present in T_d coordination in GaN NWs. Careful examination of the experimental data (Figure 3.5b, black trace) indicates that both Mn^{2+} and Mn^{3+} contribute to the observed spectrum, although Mn^{2+} is the dominant form.

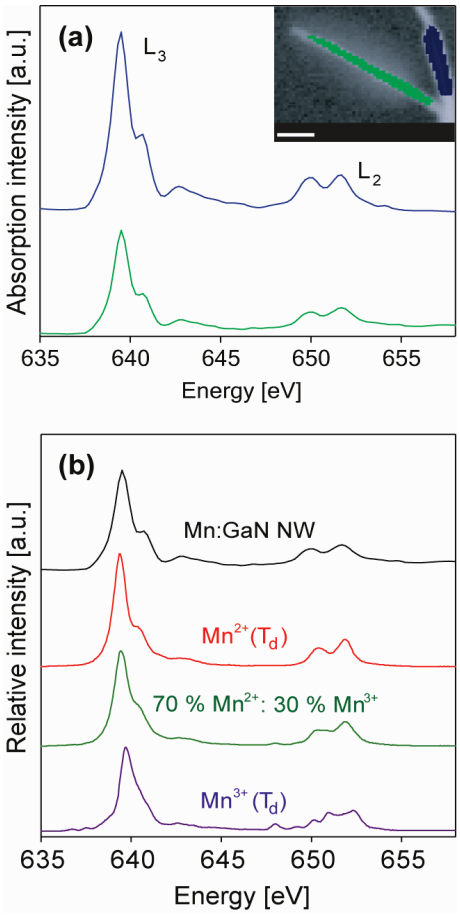

Figure 3.5: Mn $L_{2,3}$-edge comparison of experiment and theory. (a) Mn L-edge spectra collected from the individual NWs (shaded region). (b) Linear combination analysis to quantify Mn^{2+}/Mn^{3+} oxidation state using CI cluster-model in tetrahedral coordination. The linear combination analysis confirmed that 70% Mn^{2+} and 30% Mn^{3+}in individual $Ga_{0.95}Mn_{0.05}N$ NWs.

To analyze more quantitatively the oxidation states of Mn in single $Ga_{0.95}Mn_{0.05}N$ NWs, linear combination analysis was performed using the calculated spectra of Mn^{2+} and Mn^{3+}. The best fit of the experimental data is obtained for approximately 70% Mn^{2+} and 30% Mn^{3+} (Figure 3.5b, green trace).[184]

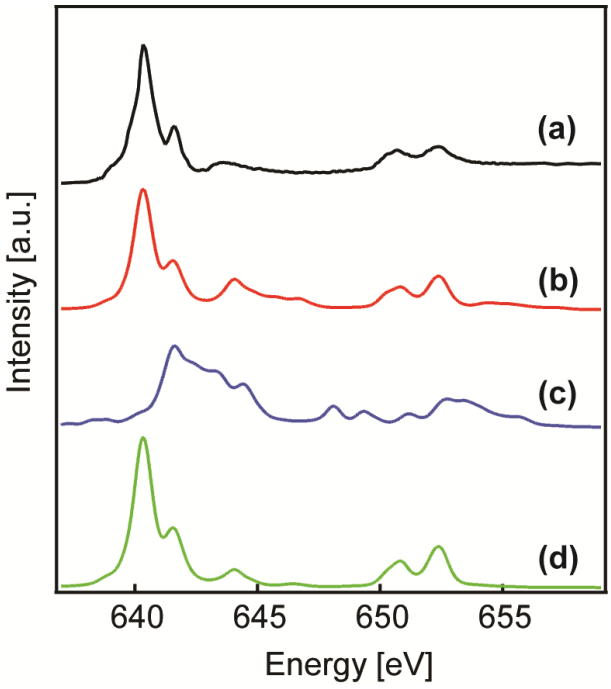

Figure 3.6: Comparison between experimental and calculated Mn $L_{2,3}$-edge spectra. (a) Mn $L_{2,3}$-edge spectrum of a single $Ga_{0.95}Mn_{0.05}N$ NW. (b) Linear combination of calculated Mn $L_{2,3}$-edge spectra (80% Mn^{2+} and 20% Mn^{3+}) based on crystal field multiplet structure model. (c,d) Calculated Mn $L_{2,3}$-edge spectra for Mn^{3+} (c) and Mn^{2+} (d) in tetrahedral coordination (10Dq = −0.5 eV).

The quantification of Mn speciation in individual NWs using CI cluster-model was overly estimated Mn^{3+} in $Ga_{0.95}Mn_{0.05}N$ NWs, as compared to previous reports.[185] Therefore, analysis was repeated and Mn L-edge simulations was performed using CTM4XAS-5.5 package (Figure 3.6).[169] It can reproduce the Mn L-edge atomic multiplets, based on the crystal field theory. These calculations further confirm the mixed oxidation state observed in the experimentally measured spectra. To quantify Mn^{2+}/Mn^{3+} linear combination analysis was performed based on calculated spectra for Mn^{2+} and Mn^{3+} in T_d coordination (Figure 3.6c and 3.6d), respectively. Using this approach, as synthesised $Ga_{0.95}Mn_{0.05}N$

NWs Mn dopants exists in 80% Mn^{2+} and 20% Mn^{3+} (Figure 3.6b) oxidation states.[186] Furthermore, half-height analysis of Mn K pre-edge analysis confirm the mixed oxidation states in $Ga_{0.95}Mn_{0.05}N$ NWs (see Appendix E, Figure E.1).[187] The presence of Mn^{3+} in bulk GaN has recently been suggested both theoretically[33,188] and experimentally.[189,190] On the theoretical perspective, recent improved *ab-initio* studies of bulk $Ga_{1-x}Mn_xN$ based on density functional theory have indicated a distortion of Mn coordination ("Jahn-Teller effect") and a localized hole state introduced by Mn, indicating dominant Mn^{3+} (d^4) character of the dopant ions.[33] These theoretical results have been supported by increasing experimental evidence for Mn^{3+} in $Ga_{1-x}Mn_xN$. Unlike Mn^{3+}, the partial stabilization of Mn^{2+} in GaN NWs favors the itinerant hole formation, offering the possibility of using $Ga_{1-x}Mn_xN$ NWs for spintronic devices.

Chapter 4

Magnetization Studies in Mn Doped GaN Nanowires

This chapter will concentrate on the study of the microscopic origin of magnetic ordering in a single Mn doped GaN nanowire using STXM. The XMCD can directly probe angular momentum of the electron, from which the magnetic properties originate, using circularly polarized X-rays. The XMCD technique is unique in determining spin and angular momentum quantitatively using sum rules, and can be correlated to crystalline anisotropy. The understanding of magnetocrystalline anisotropy at the single nanowire level through the use of state of the art technique like STXM is of fundamental significance in building nanowire based spintronic devices.

4.1 Magnetic Properties of Single Mn Doped GaN Nanowire

To understand magnetic properties of the individual $Ga_{0.95}Mn_0.05N$ NWs, XMCD measurements were performed using STXM. XMCD measures the difference between the absorption of left circularly polarized (LCP, μ^-) and right circularly polarized (RCP, μ^+) light in the presence of an external magnetic field applied parallel to the incoming X-ray beam [158] (Figure 4.1b) using a tiny magnet (Figure 4.1a) of field strength $\sim$0.1 T, and allows for element specific determination of magnetic properties (see for details Sec. 2.6). The spin imbalanced density of $3d$ states of Mn provides net magnetic moment in the host lattice,

which can be probed by exciting the $2p$ core electrons to partially filled $3d$ states (Figure 4.1c).[158] The angular momenta of circularly polarized light couples with the Mn dopant spin via spin-orbit coupling, thereby giving the XMCD signal with nanometer scale spatial resolution. Figure 4.1d shows the absorption spectra for μ^+ and μ^- and the corresponding XMCD spectrum of a typical NW in the region parallel to the magnetic field direction (orange area in the inset of Figure 4.1d). The observed XMCD spectrum attests to the room temperature magnetization arising from substitutional Mn dopant ions in the nanowire.

The orbital and spin moment of Mn dopants was estimated using XMCD sum rules (eq 2.10 and 2.11, respectively), neglecting the expectation value of the magnetic dipole operator $\langle T_z \rangle$.[160] On the basis of the ratio of Mn ions with +2 and +3 oxidation states, n_{3d} value of 5.3 was used for this calculation. The maximum spin and orbital momenta determined from the integrated XMCD intensity are 0.27 μ_B/Mn and -0.03 μ_B/Mn, respectively. A detailed analysis of XMCD sum rule is beyond the scope of this work because of the small separation between the L_3 and L_2 edges caused by significant quantum-mechanical j-j mixing in the case of light transition metals such as manganese and chromium. This effect will reduce the total magnetic moment by a factor of two.[191] A relatively large contribution of m_o (10%) having the opposite sign of m_s indicates a significant spin-orbit interaction in GaN NWs, and that m_s and m_o are coupled antiparallel. The determined net magnetic moment is estimated to be at least an order of magnitude larger than the magnetization of paramagnetic $Ga_{1-x}Mn_xN$ crystals,[50] suggesting a long-range ordering of Mn dopants in GaN NWs. It should be emphasized that this magnetization is detected at subsaturation effective magnetic field strength (<0.1 T). Therefore, it is notable that this dilute intrinsic magnetic ordering can be observed and quantitatively determined at room temperature in individual NWs using a miniature device-size magnet.

Although these data indicate intrinsic ferromagnetism arising from Mn dopants, the mechanism of magnetic ordering may still be open to debate.[106,182,192] The substitution of Mn^{2+} for Ga^{3+} leads to hole formation in GaN NWs, which can mediate magnetic ordering, although possibly by a mechanism[192] different from that initially proposed by Dietl *et al.*[14] The defects[182] and surfaces[106] may also have a significant impact on ferromagnetic interactions in one-dimensional DMSs. Unlike the XMCD spectrum of the NW section oriented parallel to the direction of the magnetic field, the spectrum of the NW area oriented 37° with respect to the magnetic field direction (Figure 4.1e) shows much lower intensity of the magnetic moment for nearly identical average absorption intensity.

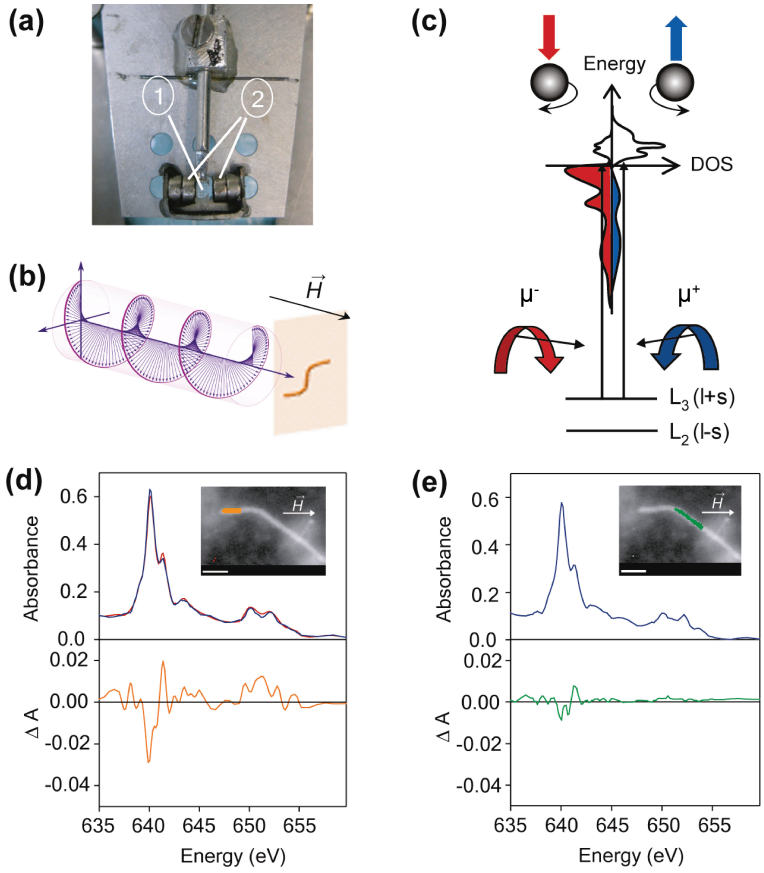

Figure 4.1: XMCD measurement at single $Ga_{0.95}Mn_{0.05}N$ NW. (a) Photograph of the experimental setup for XMCD measurements by STXM. A fraction of a TEM grid with deposited NWs (1) is placed between the poles of the device-size magnet (2). (b) Configuration of XMCD microscopy measurements. The setup shown in (a) is placed in the beam path 30° with respect to the normal incidence, which allows a component of the applied magnetic field (<0.1 T) to be oriented parallel to the propagation of the circularly polarized photons. The spectra were obtained by alternate imaging with LCP and RCP photons. (c) Schematic representation of the density of states (DOS) of Mn doped GaN NWs indicating the spin orientations (blue and red arrows). The XMCD transitions occur from the spin-orbit split $2p$ shell to empty $3d$ states of Mn dopants (black arrows). (d,e) Mn $L_{2,3}$-edge XMCD spectra collected at 300 K of a nanowire in the region parallel (d) and making 37° angle (e) with the magnetic field direction, obtained as a difference between μ^- (red) and μ^+ (blue). The nanowire regions corresponding to XMCD spectra are shown in the insets (scale bars, 0.8 µm).

4.2 Origin of Magnetocrystalline Anisotropy in Mn Doped GaN Nanowires

The dependence of the spin magnetic moment on the NW orientation suggests anisotropy effect on the magnetic exchange interactions. For dilute magnetization, it is unlikely that the orientation dependence comes from the shape anisotropy.[193] The strength of the shape anisotropy in cylindrical wire is $^1/_2(E_\perp - E_\parallel)M_s^2 = \pi M_s^2$, where, $E_\perp$ and $E_\parallel$ are the anisotropy energy along the perpendicular and parallel to the NW long axis, and M_s is the saturation magnetization. For wires to exhibit pure shape anisotropy, an external field of at least $2\pi M_s$ ($\sim$0.6 T) is required,[194] and in this study XMCD measurements on the single NW were performed at a field strength of $\sim$0.1 T. Therefore, shape anisotropy is unlikely at this subsaturation magnetic field. Instead, in this work it is hypothesized that crystalline anisotropy is responsible for the observed difference in magnetization for the two investigated areas of the NW. To establish the origin of the dependence of Mn exchange interactions on the NW orientation by plotting the maximum L_3-edge XMCD intensities, corresponding to the equivalent average absorption spectra, as a function of the angle θ between the NW orientation and the magnetic field direction (Figure 4.2a, red squares). The effective magnetic moment of Mn decreases with increasing θ, becoming nondetectable for $\theta = 90°$. Spontaneous magnetization in different crystallographic directions is characterized by the magnetocrystalline anisotropy energy (E_{an}), which has the minimum value for the easy axis of magnetization. The anisotropy energy for uniaxial crystals is described by a series expansion, which can be reduced to,

$$E_{an} = K_0 + K_1 sin^2\theta \tag{4.1}$$

where K_0 and K_1 are anisotropy constants. Calculations of the anisotropy energy have shown that the Mn magnetic moment is oriented preferentially along the $\langle 10\bar{1}0\rangle$ direction in GaN,[106] which is the dominant NW growth direction in this study. The results of this work are therefore in agreement with the theoretical predictions.[106] Other contributions to magnetic anisotropy include the anisotropy of the local potential experienced by the bound hole[195] or possibly the contribution arising from Mn^{3+}. The difference in energy of magnetization per unit volume of material for magnetic moments parallel and perpendicular to the easy axis is $E_\perp - E_\parallel$. Therefore, E_{an} should be inversely correlated with magnetization and increase symmetrically to a decrease in XMCD intensity, obeying $sin^2\theta$ dependence (Figure 4.2a, green spheres). Conversely, XMCD intensity itself follows $cos^2\theta$ dependence (Figure 4.2a, red line). The measured variation of XMCD intensity attests to the magnetocrystalline anisotropy as the origin of the magnetization dependence on the NW orientation. These results demonstrate tunability of dilute spin-exchange interactions in DMS NWs at room

temperature through NW orientation. This orientation dependence was confirmed by the analysis of at least 10 different NWs that we were able to investigate during the given experimental time, demonstrating the reproducibility of the effect within the sample.

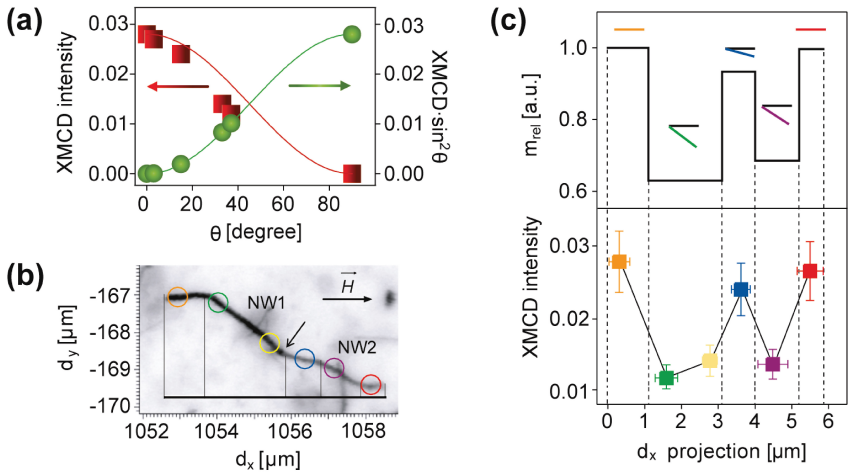

Figure 4.2: Orientation tunable spin interactions in single $Ga_{0.95}Mn_{0.05}N$ NWs. (a) XMCD intensity measured at 640 eV (at 300 K) vs angle θ between the nanowire long axis and the magnetic field direction (red squares). This relation is opposite from $XMCD \cdot \sin^2\theta$ dependence on θ (green spheres), indicating crystalline anisotropy origin of the change in XMCD intensity with nanowire orientation. Red and green lines are simulated $\cos^2\theta$ and $\sin^2\theta$ dependencies, respectively. (b) STXM image (at 633 eV) of two joined nanowires (the point of junction is indicated by the black arrow). The circled areas indicate the regions on the NWs probed by XMCD. The direction of the magnetic field is parallel to d_x. (c) Simulated relative change in magnetic moment based on the change in crystalline anisotropy energy along d_x (upper part). The colored lines above the graph indicate the NW orientation with respect to the magnetic field direction (black lines). Measured XMCD intensities in the regions circled in part (b) are shown with analogous colors in the lower part as a function of d_x. Error bars indicate standard uncertainty in XMCD measurements (y-axis) and d_x range for the NW regions from which XMCD was extracted (x-axis).

The orientation dependence can, in principle, be exploited to design nanowire-based network structures that could be used for quantum information processing. One such example, shown in Figure 4.2b, is a simple motif of alternate NW orientations, which can be formed by selecting the NWs based either on their longitudinal morphology or simple van der Waals bonding of different NWs. Both examples are demonstrated in Figure 4.2b, in

which two bent NWs are joined together forming a recurring motif. The expected XMCD intensity for the magnetic field direction shown in Figure 4.2b should change with the NW orientation according to $\cos^2\theta$ dependence. The simulated relative change in magnetic moment as a function of the NW projection distance along the magnetic field direction (d_x) is shown in Figure 4.2c (upper part). Experimentally measured Mn L_3-edge XMCD maxima corresponding to normalized absorption spectra recorded along the NW assembly show very good agreement with the predicted magnetization behavior (Figure 4.2c, colored squares), demonstrating the potential to reproducibly tune the magnitude of Mn dopant exchange interactions by NW orientation.[184]

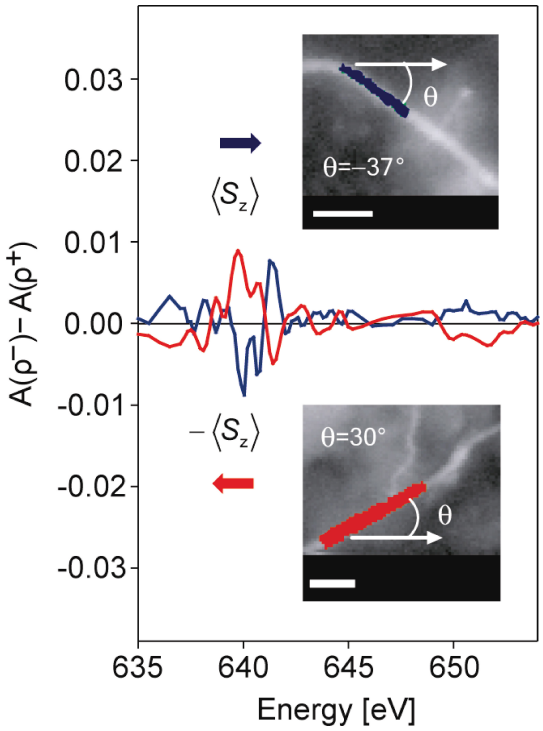

Figure 4.3: XMCD spectra (300 K) of two NWs (shown in the insets) having the opposite orientation with respect to the magnetic field. The change in the sign of XMCD for two NW orientations attests to the reversal in spin orientation. Scale bars, 0.8 µm.

An important aspect of exploiting NW orientation for controlling spin-exchange interactions of magnetic dopants is the possibility of the reversal of spin polarization. Figure 4.3 shows XMCD spectra of two NWs (shown in the insets) making an angle of 30° with the magnetic field direction, but in the opposite directions; one clockwise the other one

counterclockwise. The opposite NW orientation is equivalent to different handedness, which can also be achieved by switching the poles of the magnetic field, or rotating the specimen 180° around the vertical axis. This difference in the rotational direction results in reversal of the signs of XMCD peaks, indicating opposite spin orientation for two different NW configurations.[184] On the basis of the orientation-dependent magnetization of NWs demonstrated in this work, it is expected that the magnetic susceptibility of as-synthesized NW samples measured by an ensemble method should be negligible.

The orientation dependence of NWs further confirmed by measuring the magnetic hysteresis loop of the NWs on the growth substrate. The PPMS magnetization data for as grown NW sample are shown in Figure 4.4. The ferromagnetism is observed at 300 K, although the saturation magnetic moment (m_{sat}) was estimated to be only 0.004 μ_B/Mn, nearly two orders of magnitude smaller than the net magnetic moment determined from single NW XMCD data. This discrepancy can be rationalized by considering the orientation dependence of NW magnetization. Random orientation of as-synthesized NWs on the growth substrate should lead to zero net magnetization due cancelation of the moments for opposite NW orientations. The observed ferromagnetism in Figure 4.4 may result from a small net orientation (i.e., non-cancelled NW magnetic moments), or the presence of co-deposited secondary phases, of which some may be ferromagnetic. Any significant magnetization measured for randomly grown NW samples would, therefore, likely to be of extrinsic origin.[187]

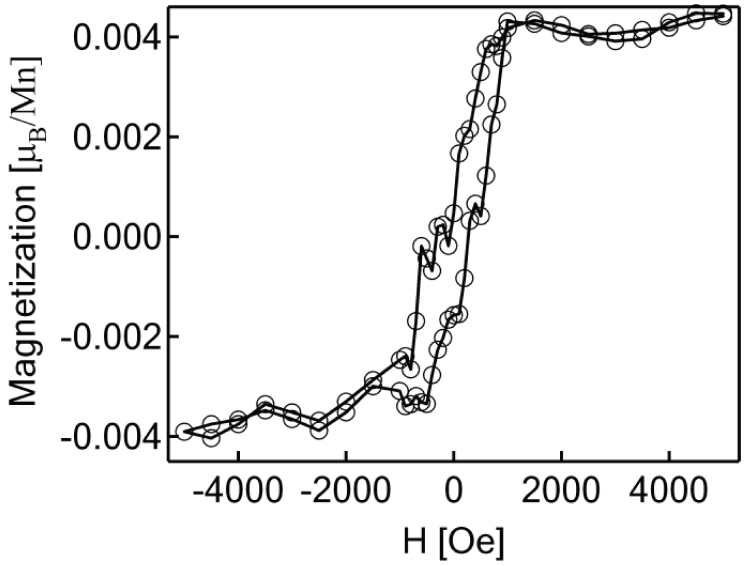

Figure 4.4: Magnetization data of as synthesized $Ga_{0.95}Mn_{0.05}N$ NWs on the growth substrate corrected for diamagnetic contribution. All data were collected at 300 K.

The comparison with ensemble measurements underscores the importance of single NW magnetization studies for truly understanding the magnetic properties of DMS NW systems. The ability to tune the magnitude and sign of the spin-exchange interactions in single NWs at room temperature using small device-size magnetic fields demonstrates the feasibility of nanowire-based spintronic circuits and opens the door for building networks for scalable spintronics devices by assembling individual NW elements.[187]

4.3 Magneto-transport Studies in $Ga_{0.95}Mn_{0.05}N$ Nanowires

Figure 4.5a shows the conductance (G) from the single NW was measured as a function of magnetic field at 10, 20, 30, 40 and 50 K, respectively. It is clearly evident from the plot that overall conductance is increasing as temperature increased from 10 to 50 K and the curve is getting flatter. In addition, the magneto-conductance is positive for all temperature range and this behaviour can be explained through weak localization theory. The expression for the weak localization correction in one-dimensional nanostructure conductance as a

function of magnetic field is,[196]

$$G(B) = G_0 - \frac{2e^2}{hL}\left(\frac{1}{L_\phi^2} + \frac{e^2B^2w^2}{3\hbar^2}\right)^{-1/2} \tag{4.2}$$

where, $L = 300\,\text{nm}$ (distance between contacts), $w = 60\,\text{nm}$ (nanowire diameter) and G_0 is the classical Drude conductance without localization correction. The two parameters G_0 and L_ϕ were used to fit the experimental conductance as a function of magnetic field (Figure 4.5a). This fitting procedure gives the value of phase coherence length at particular temperature. Figure 4.5b and 4.5c are the magneto-conductance data at 10 K and 50 K, respectively. The solid red line is the fit to the model given by eq 4.2 and it is clear that fitted curves follow the field dependent conductance at two different temperatures.

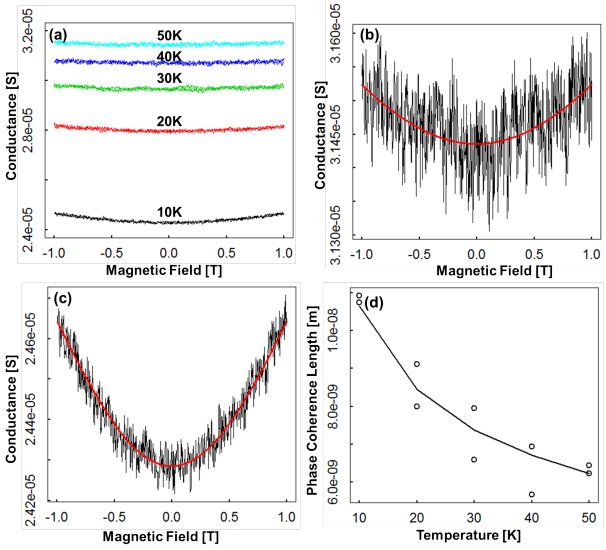

Figure 4.5: (a) Magneto-conductance measurement on the single $Ga_{0.95}Mn_{0.05}N$ NWs as a function of magnetic field. The measurement was done at temperature 10, 20, 30, 40 and 50 K by applying a bias of 2 mV. Magnetic field was applied perpendicular to the nanowire long axis. (b) and (c) Magneto-conductance data collected at temperature 10 and 50 K, respectively. The solid red line is fit to the experimental data using weak localization theory. (d) The extracted phase coherence length from the weak localization theory shows the $L_\phi \sim T^{-1/3}$ dependency (solid black line).

It is important to note that eq 4.2 is satisfied by the fitting results in Figure 4.5b and 4.5c. The phase coherence length extracted from fitting the data in Figure 4.5a plotted

as a function of temperature in Figure 4.5d. The two data points in Figure 4.5d at each temperature are due to the conductance was measured twice at same temperature. The extracted phase coherence length fitted with $L_\phi \sim T^{-1/3}$ (Figure 4.5d, solid black line) and exhibits the power law dependency. This analysis is consistent with Nyquist dephasing mechanism, which arises due to the electron-electron collision with limited amount of energy transfer. From this study the weak anti-localization effect can be ruled out as it has negative magneto-conductance and was observed in wires having width greater than 750 nm. The suppression of weak anti-localization effect can enhance the spin-orbit scattering length in narrow wires and was verified theoretically in case of $Al_xGa_{1-x}N/GaN$ nanowire heterostructure.[197] This makes $Ga_{0.95}Mn_{0.05}N$ NWs promising material for future spintronic device applications.

Chapter 5

Growth Mechanism and Origin of Valence Band Anisotropy in Gallium Oxide Nanowires*

This part of the work deals with understanding of faceted morphology in β-Ga_2O_3 NWs by changing the growth conditions based on SEM, HRTEM and atomic lattice modelling. The origin of anisotropy was studied using linearly polarized X-rays at the single nanowire level using STXM. The experimental results were further confirmed by theoretical calculations specifically for the O K-edge XANES. The different atomic orbital contributions to the linear dichroism was analyzed by calculating angular momentum projected density of states. The understanding of nanowire faceting, morphology, and anisotropy has a significant importance in building optoelectronic devices, photonics, chemical sensing and catalysis.

5.1 Crystal Structure of Ga_2O_3 and Morphology

Base-centered monoclinic β-Ga_2O_3 belongs to the space group $C2/m$ with the lattice parameters $a = 12.23$ Å, $b = 3.040$ Å, $c = 5.807$ Å, $\alpha = \gamma = 90°$ and $\beta = 103.7°$.[129,198] The unit cell is made up of 8 Ga and 12 O atoms, containing four formula units (Figure 5.1a).

*Part of this work, specifically nanowire growth mechanism extracted directly from the following paper: Reprinted from J. Cryst. Growth, Vol. 396, I. D. Hosein, M. Hegde, P. D. Jones, V. Chirmanov, P. V. Radovanovic, Evolution of the faceting, morphology and aspect ratio of gallium oxide nanowires grown by vapor-solid deposition. pp. 24-32, Copyright (2014), with permission from Elsevier.

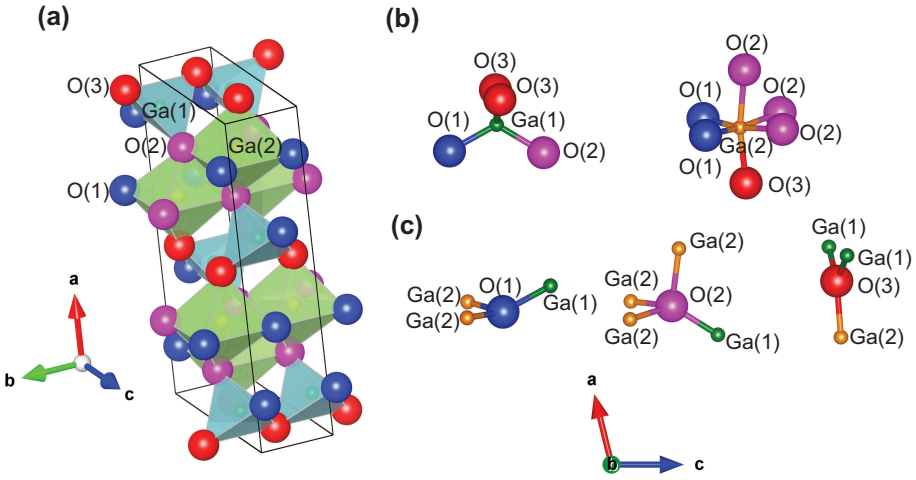

Figure 5.1: Crystal structure of β-Ga_2O_3. (a) Unit cell of monoclinic lattice showing different Ga and O sites. (b,c) Coordination of nonequivalent gallium (b) and oxygen (c) sites viewed along the crystallographic b axis. Note that the apparent orientation of the unit cell does not coincide with the NW growth direction, which is along the b axis.

One half of Ga atoms reside in tetrahedrally-coordinated sites (Ga(1)), and the other half has a distorted octahedral coordination (Ga(2)). These sites are shown in Figure 5.1b, projected along the *b*-axis. Oxygen atoms exist in three non-equivalent highly distorted sites; O(1) and O(3) being tri-coordinated and O(2) being four-coordinated.[199] Figure 5.1c shows the projection of O sites along the *b*-axis. The O(1) atom is sitting out of plane of a triangle made up of two Ga(2) and one Ga(1) atoms, O(2) is coordinated with three Ga(2) and one Ga(1) atoms in quasi-tetrahedral geometry, and O(3) is coordinated in the plane of a triangle consisting of two Ga(1) and one Ga(2) atoms. From the unit cell in Figure 5.1a it can also be seen that O(1) and O(3) are located at the edges shared by a single tetrahedral and octahedral Ga chain, while O(2) resides at edge shared by single tetrahedral and double octahedral Ga chains. The crystal structure of β-Ga_2O_3 shown in Figure 5.1 can be described as double chains of edge-sharing GaO_6 octahedra connected by single chains of vertex-sharing GaO_4 tetrahedra along the *b*-axis.[200]

The SEM image of as synthesised NWs having different aspect ratio are shown in Figure 5.2a. The careful observation of individual NWs reveals that, they evolved with simple rectangular or hexagonal cross-section (Figure 5.2b) to more complicated highly faceted morphologies (Figure 5.2e). The SEM imaging across the different regions of the substrate confirm that majority of the NWs posses morphology between these two extremes (Figure 5.2c and d). The thickness of these NWs approximately within the range

of 100-200 nm with an average thickness of 120 ± 47 nm (Figure 5.2f). The lengths of these NWs estimated to be 1.2 ± 0.5 µm (Figure 5.2g) and with a smooth surface. The thickness of NWs is within the range of reported values for β-Ga_2O_3 NWs, which were synthesise using Au-catalysed VLS mechanism.[201,202] The EDS peaks for Ga (Lα peak at ~ 1.11 keV) and O (Kα peak at ~ 0.53 keV) along with Si peak from the growth substrate at ~ 1.11 keV (Kα) without any additional peaks. This indicates high purity of as synthesised samples.

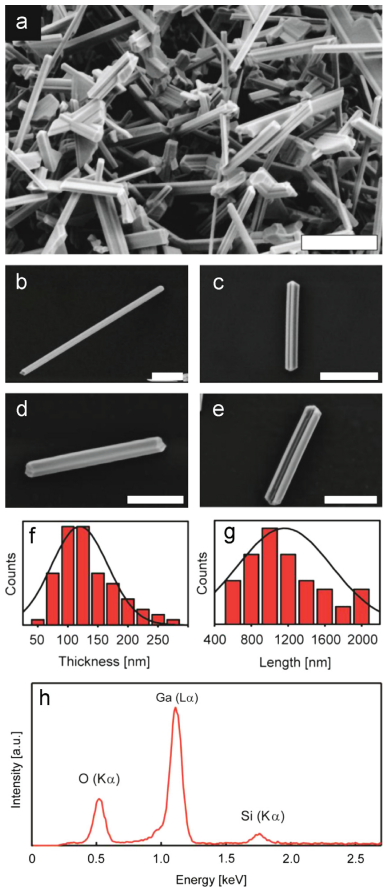

Figure 5.2: Faceted Ga_2O_3 nanowires. (a) SEM over view image of NWs. (b)-(e) SEM images of selected individual NWs showing different faceting structure. Scale bars represent 1 µm for (a) and (b), and 500 nm for (c)-(e). (f) and (g) Thickness (f) and length (g) distribution histograms for the nanowires shown in (a). (h) Typical EDS spectrum of as-synthesized gallium oxide nanostructures. The silicon peak is from the growth substrate.

The above observed morphology of Ga_2O_3 NWs also depends on reaction conditions,

especially on the growth temperature, oxygen precursor concentration, and carrier gas flow. Figure 5.3 shows SEM images of NWs at different reaction conditions.

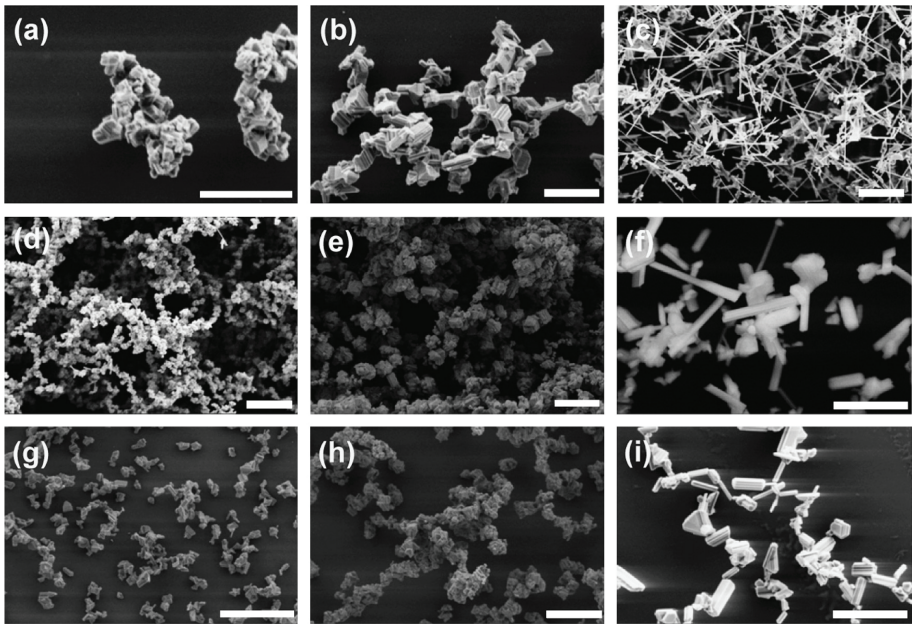

Figure 5.3: SEM images of formation different morphology of the nanowires by varying the growth parameters. (a) 800 (b) 900 and (c) 1000 °C with 1000 sccm Ar gas, 1.5 sccm of O_2 and 10 min reaction time. (c) Showing the clear morphology of one-dimensional morphology. (d) 100 (e) 200 (f) 400 sccm Ar flow at a temperature of 1000 °C, 1.5 sccm of O_2 and 10 min reaction time. (g) 6, (h) 3, (i) 1.5 sccm of O_2 at 950 °C growth temperature, with 400 sccm carrier gas flow and 10 min growth time. Scale bars are 1 µm for (a), (b), (f), and (g); all others are 2 µm.

Figure 5.3a-c illustrates formation of different nanostructure morphology ranging from poorly-defined nanoclusters to well defined one dimensional nanostructures with smooth surfaces and high aspect ratios, under different growth temperature (800-1000 °C) keeping other parameters constant. Whereas in Figure 5.3d-f similar observations were made by varying the carrier gas flow rate ranging from 100 to 400 sccm, resulting in multifaceted morphology with high aspect ratio. On the other hand by decreasing the oxygen gas flow rate by 6 to 1.5 sccm (Figure 5.3g-i) a very similar effect was observed as in Figure 5.3d-f. From this analysis it is confirmed that by varying the temperature above >950 °C with low oxygen precursor and high carrier gas (Ar) flow (400 sccm), NWs of high aspect ratio with

faceted morphology was obtained. All other conditions resulting in faceted morphology with low aspect ratios and temperature below 700 °C there was no nanowire growth occurred. Moreover, the growth parameters which were used to produce high aspect ratio faceted nanostructures does not depend on the separation distance between the precursor source and growth substrate and the yield was decreased when gallium source was moved away from growth substrate inside the quartz tube.

5.2 TEM Analysis and Atomic Lattice Modelling

The faceted morphology of NWs was further analysed using TEM. Figure 5.4a shows the TEM image of the nanowire inset is the selected area electron (SAED) diffraction pattern of the NWs. The clear diffraction pattern confirm the single-crystalline nature of the multi-faceted NWs. The streaking present in the pattern is attributed to stacking faults and micro-twins.[203] The SAED pattern with no such artifact was used for detailed crystal structure analysis (Figure 5.4b and c). The SAED pattern confirms that NWs grew along [010] direction, which is *b*-axis of the monoclinic crystal structure and lattice direction perpendicular to the growth direction corresponds to {100} planes. The calculated lattice spacing for 020, 110 (or $\bar{1}10$), and 200 Bragg spots are 0.513, 0.297, and 0.590 nm (Figure 5.4b), respectively. The measured angle between [010] and [$\bar{1}10$] plane is 104.3°, which is in good agreement with the reported values. The calculated direct lattice plane measurements 0.149, 0.296, and 0.595 nm (Figure 5.4c) agree reasonably well with those determined form SAED pattern, and also correspond to Miller indices (*hkl*) of 020, 110 (or $\bar{1}10$), and 200, respectively. The lattice parameters *a* and *b* are indicated on the HRTEM image in Figure 5.4c and their measured values are 12.01 and 2.976 Å, respectively, in good agreement with the reported values.[129,198,199]

Relative orientation of lattice planes and NWs were further understood by comparing the HRTEM images to the corresponding lattice plane models of monoclinic β-Ga_2O_3[198] oriented in the same direction as the experimental zone axis (Figure 5.5). Figure 5.5a shows the lattice resolved HRTEM image of the NW perpendicular to the growth direction [010]. It is evident from the model that arrangement and symmetry elements are well-correlated with the model crystal oriented along the [001] zone axis (Figure 5.5b, black circles). Similar analysis along the [100] direction also gives good agreement with respect to Ga atomic arrangements and symmetry (Figure 5.5c and d). These results suggest that a preferred NW lattice orientation exists, with the [010] direction parallel to the NW growth direction.

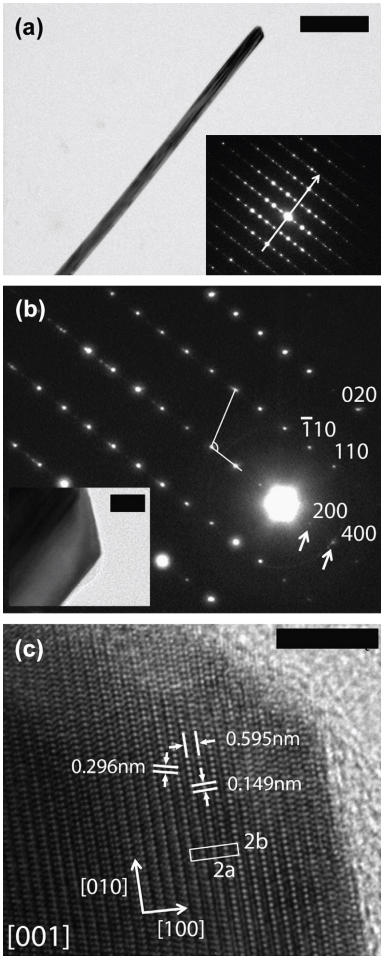

Figure 5.4: TEM analysis of faceted NWs. (a) TEM image of a nanowire under low magnification, inset is the SAED, confirm the single crystallinity of the NWs. Scale bar, 0.5 µm. (b) SAED pattern along the [001] zone axis indicating the lattice spacings and they are in good agreement with the reported values. The inset is the region from which SAED pattern was obtained. Scale bar, 20 nm. (c) Lattice-resolved TEM image of the corner of the nanowire, labelled with lattice spacings and growth directions. Scale bar, 5 nm.

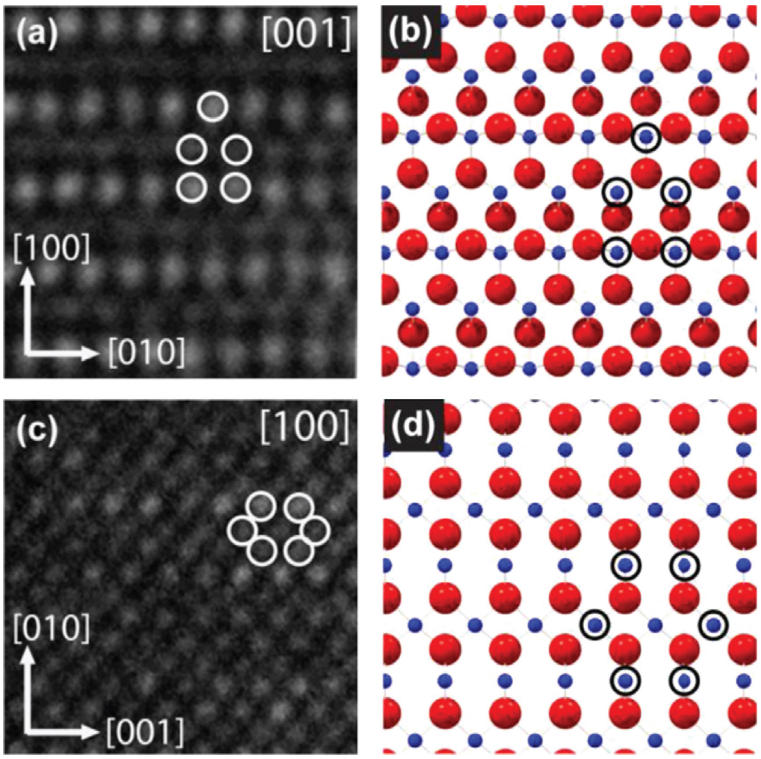

Figure 5.5: Atomic lattice modelling. (a) Close-up image of Ga_2O_3 nanowire lattice along the [001] zone axis direction. (b) Corresponding atomic model plane along the [001] direction, showing atomic positions of gallium atoms (blue) and oxygen atoms (red). The identical lattice symmetry and atomic positions in (a) and (b) confirm the zone axis and the assigned nanowire facet orientation. (c) Close up image of the atomic lattice imaged along the [100] zone axis direction. (d) Corresponding atomic model plane along the [100] direction confirms the lattice indexing. The circles in all panels indicate gallium atom arrangement motifs.

5.3 Morphology Evolution

The morphology of crystals grown from the vapor depends on the growth kinetics of different crystal facets.[204] The classical growth theories for flat crystal surfaces explain that discontinuities in the surface, such as kinks and ledges, act as sites for the incorporation of new atoms (Figure 5.6a).[205–207] These sites cause the irreversible adsorption of atoms and thus facilitate growth. As a result, the growth of a crystal surface occurs through the advancement of these steps, and the growing crystal boundary moves in the direction perpendicular to the surface. Whereas, atoms that adsorb on smooth surfaces are more likely to escape back into the vapor before diffusing over the surface to an adsorption site, especially at higher temperatures. High index crystal planes will have a higher density of these sites, and thus will grow faster than low index planes, which are more atomically smooth (i.e., fewer discontinuities). Ideally, higher index planes (i.e., higher surface energy facets) should disappear in the growth evolution with the lowest energy surfaces remaining as determined by the Wulff plot.[205,208] Therefore, the formation of high aspect ratio, faceted structures based on growth rate differences at the surface is highly dependent on the underlying crystal structure, although other mechanisms such as defect-induced growth may also be involved. These principles can be used to rationally tune the nanostructure morphology. Specifically, in this study temperatures above 950 °C produced only thin, long NWs, with simple cross section morphologies, most likely due to ease of desorption of growth adatoms from the smooth side walls corresponding to the most stable facets. A decrease in the the growth temperature produces thicker nanostructures with more complex faceted surfaces, indicating a higher probability of growth species incorporation onto the side walls. At lower temperatures, surface facets remain, yet the aspect ratio is reduced.

The control of anisotropy is also highly dependent on other growth conditions including the concentration and flow rate of NW precursors in the gas phase, as required to achieve low supersaturation conditions. At the single nanostructure level, the control of these parameters allows the local precursor concnetration to be higher than equilibrium concentration for some surfaces, but equal to or lower than that for others,[204] leading to advancement of specific NW facets. Hence, under conditions of high temperature, low precursor concentration, and high carrier gas flow, growth is concentrated at the ends of the nanostructure, resulting in NW with high aspect ratios and low degree of faceting. Whereas, low temperature, high precursor concentration, and low carrier gas flow conditions lead to moderate supersaturation which supports bulk crystal growth (i.e., generally isotropic growth with random faceted surfaces). Finely tuning the growth parameters leads to suitable conditions for the formation of NWs with high aspect ratios and side wall faceting to occur.

Notably, the pointed tip observed for typical multi-faceted NWs (Figure 5.4) indicates

that growth along the [010] direction occurs on high index crystal surfaces most likely with high growth rates. It is possible that growth at the tip occurs by (010) terrace planes growing laterally until they reach the side walls of the nanostructure, perpendicular to the long axis, as shown in Figure 5.6b. New (010) planes would continuously nucleate at the outer most edge of the pointed tip and, consequently, the high energy surfaces remain, allowing NW growth to persist in this direction. This would explain the high energy tip surfaces, and account for the advancement of the growth along the [010] concurrently with an increase in the NW thickness (and a decrease of the NW aspect ratio) under moderate-to-high supersaturation conditions, as demonstrated in Figure 5.3. The [010] NW growth direction is also consistent with free surface energies of the primary faces of the unit cell decrease in the order (010)>(001)>(100).[209] Hence, the (010) lattice plane should grow the fastest, resulting in the NW long axis along this direction.

The morphology of the NW cross-section may initially be dictated by the underlaying symmetry of the monoclinic β-Ga_2O_3 lattice along the (100) and (001) planes, resulting in the exposure of the low energy lattice planes, and a quasi-hexagonal NW morphology (Figure 5.6c, left). As the facet boundaries along the walls extend further into the surrounding precursor vapour, they will consume more precursor and, consequently, induce a net diffusion from the side walls to the NW edges. Hence, the NW boundaries will advance faster at these edges, which will inevitably begin to grow their own facets, leading to the change in the cross-section morphology and the formation of multi-faceted structures. Furthermore, it was observed that NWs with higher degrees of faceting were on average shorter than "less-faceted" NWs (5.2 and 5.3). One possible explanation for this is that the greater surface area of the side walls will consume more precursor under the favorable conditions (vide supra), creating a net flux of precursor towards the surface and rendering the tips deficient of precursor. Thus the growth may initiate from the tips, leading to the NW morphology, until sufficient side wall surface area and faceting exists. Hence, a reasonable assumption is that the sequence of images from Figure 5.2b-e are snapshots of particle morphology evolution over time. Possible facet development based on NW morphologies observed in SEM images is schematically shown in Figure 5.6c. As nucleation may occur at different times during the growth, the samples consistently show nanostructures with different degrees of evolved facets, yet with all generally having high aspect ratios.

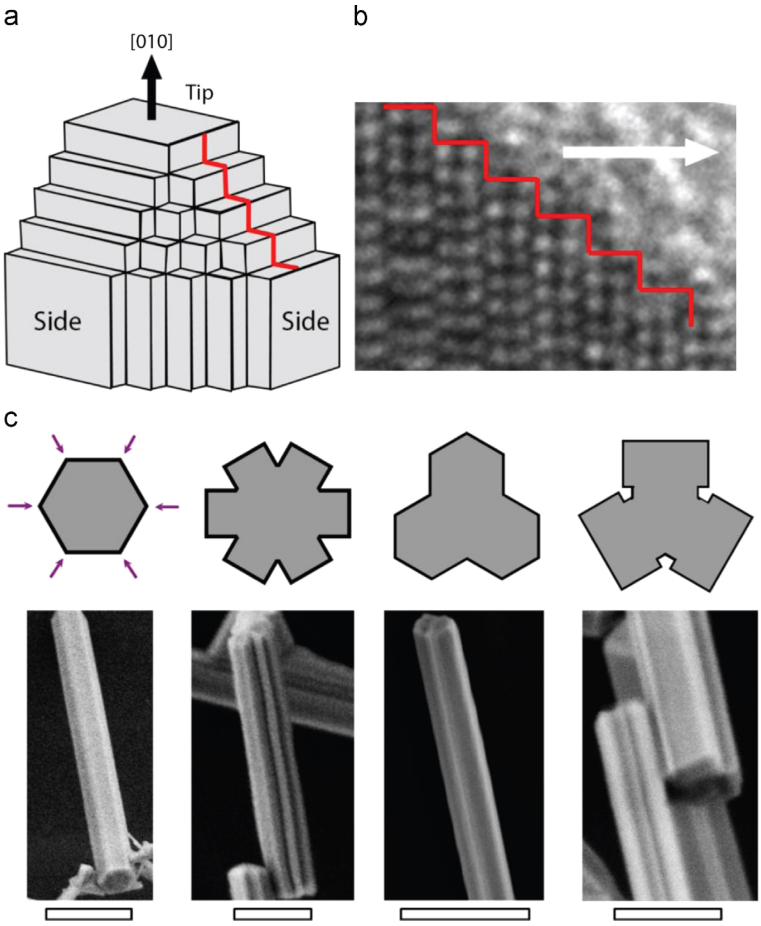

Figure 5.6: Possible evolution of nanowire faceting. (a) Schematic diagram of the nanowire growth at the tip of the nanowire. Along the red line atoms are incorporated during the growth. (b) HRTEM of the ledges located at the tip of the NW. (c) Schematics of the proposed evolution of facets along with SEM images. Scale bars are 1 µm, 200 nm, 200 nm, and 200 nm, from left to right, respectively.

5.4 Electronic Origin of Anisotropy in β-Ga_2O_3 Nanowires

The individual NWs were imaged with linearly polarized X-rays for $E \parallel b$ and $E \perp b$ using STXM, as indicated in Figure 5.7a. The unit cell corresponding to the orientation of the NW indicated in Figure. 5.7a (green shade), viewed in the ab plane, is shown in Figure. 5.7b. Ga $L_{2,3}$-edge and O K-edge XANES spectra of this NW for $E \parallel b$ (red trace) and $E \perp b$ (black trace) polarizations are shown in Figure 5.7c and 5.7d, respectively. The L-edge spectra probe the transitions from $2p$ states to empty states involving d or s orbitals above the Fermi level, while K-edge spectra probe the transitions from $1s$-based ground state to unoccupied states having p-character, based on the electric-dipole selection rule. The isotropic or average XANES spectra for both elements were calculated using the expression $[^2/_3(E \parallel b) + {}^1/_3(E \perp b)]$ (pink traces in Figure 5.7c and 5.7d), which is commonly used for measurements involving linearly polarized light.[210] These spectra are in excellent agreement with the spectra collected for an ensemble of randomly oriented NWs using linearly polarized light (green traces in Figure 5.7c and 5.7d), confirming the NW orientation-based X-ray absorption anisotropy.

Comparison of the linearly polarized XANES spectra in Figure 5.7c and d reveals that O K-edge shows much stronger linear dichroism, suggesting dominant valence band anisotropy of Ga_2O_3 NWs grown along the b-axis (vide infra). The difference in linear dichroism for Ga $L_{2,3}$-edge and O K-edge spectra can be attributed to different spatial orientation and symmetry of the atomic orbitals responsible for these transitions. The K-edge spectra contain the contribution from dumbbell-shaped $p_{x,y}$ and p_z orbitals, and the high degree of linear dichroism reflects the asymmetric nature of these orbitals.[211,212] On the other hand, s orbitals are spherical and d orbitals have more symmetric distribution in space, rendering $L_{2,3}$-edge spectra much less sensitive to the excitation polarization.[211,212] Furthermore, O K-edge XANES has higher spectral resolution owing to the significantly smaller core-hole width (0.16 eV)[213] compared to Ga $L_{2,3}$-edge (0.76 eV), which can also contribute to the observed difference in polarized X-ray absorption. Oxygen K-edge XANES can also be used to assess the character of the GaO bond, which has been a matter of debate in the case of β-Ga_2O_3. The difference in Pauling electronegativity between Ga and O is 1.6. This difference implies that a simple GaO bond is 60% ionic, and that the net charge transfer to the O atom of $1.2e$,[133] where e is the modulus of the electron charge. In purely ionic form oxygen has valence electronic configuration $2p^6$, and therefore $1s \rightarrow 2p$ transition should not be observed.[213] Increased covalency reduces the number of occupied O $2p$ states, making polarized K-edge XANES an effective probe of the anisotropy of bonding character in Ga_2O_3 NWs. In general, the crystal lattices having cation coordination number 6 were found to

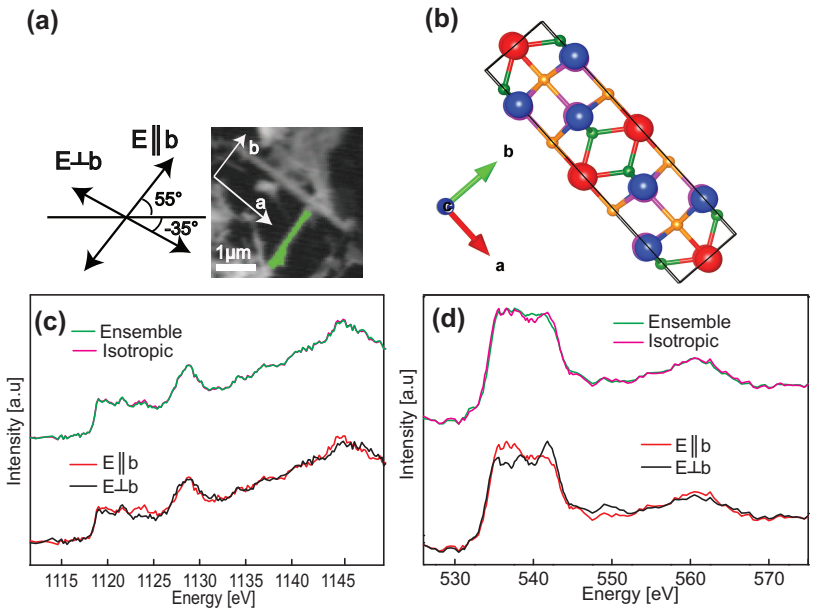

Figure 5.7: Anisotropy probed by linearly polarized X-rays. (a) STXM image of the specimen collected at 526.0 eV (right), and the polarizations of the incident X-rays used for imaging (left). The shaded area in the image indicates the analyzed NW and the inset shows the NW *b*-axis orientation relative to the X-ray polarization. (b) Unit cell orientation of the analyzed NW projected in the *ab* plane. (c,d) Ga $L_{2,3}$-edge (c) and O K-edge (d) XANES spectra of the shaded NW for parallel (red) and perpendicular (black) polarization of E relative to the NW long axis. The single NW spectra are compared to isotropic (pink) and ensemble NW spectra.

be ionic, with the degree of covalency increasing with decreasing coordination number.[213] For example, materials having rock salt crystal structure with octahedral cation sites were found to be ionic, whereas zinc blende or wurtzite lattices with tetrahedral cation sites are more covalent. β-Ga_2O_3 has both O_h and T_d gallium sites, and therefore is expected to have a mixed character.[139] Taking into account all of the above considerations, this work focuses predominantly on the analysis of the linearly polarized O K-edge XANES spectra.

In order to develop better quantitative understanding of the experimental data, monoelectronic calculations were performed based on the multiple scattering theory.[156] The net charges on O(1), O(2), and O(3) were determined to be -0.90e, -0.87e, and -0.77e, respectively. Conversely, the calculated net charge on Ga atoms is +1.4e. The signs of the calculated charges are in agreement with the electronegativity of Ga and O, although their values differ from the formal charges, presumably due in part to some covalent bond character. A deviation from the overall charge neutrality is likely due to the values of the atomic radii used for the charge calculation.[214] The electron localization function analysis based on generalized gradient approximation density functional theory (GGA-DFT) calculation has shown that the valence electrons were localized around the O atoms; however, they were deviating from the spherical symmetry indicating a certain degree of covalency.[215] In spite of some uncertainty in the obtained charge values, these results are consistent with the mixed bonding character in single β-Ga_2O_3 NWs.

As the first step in the simulation of the XANES spectra, optimized MT radii (R) were found by increasing the number of atoms in the cluster using Norman procedure. At $R = 7.8$ Å all of the XANES fine structure was well reproduced for O K-edge (Figure 5.8a). Further increase in R did not lead to significant improvement, and this value was used for polarization-dependent XANES calculations. Calculated XANES spectra for O(1), O(2), O(3), and their combination for $E \parallel b$ (red traces) and $E \perp b$ (black traces) polarizations in bc plane are compared to the experimental data in Figure 5.8b. The calculated spectra in Figure 5.8b include broadening of the raw spectra (see Appendix F, Figure F.1) due to core-level and final state widths (see eq 2.18). The experimental and overall calculated spectra are in good agreement, confirming the crystal and electronic structure anisotropy for the NWs grown along the b-axis. The peak labeled **a** is largely due to O(3), which is bonding in plane with two Ga(1) and one Ga(2) atoms, as shown in Figure 5.1c. The Ga(1) site has a higher degree of covalency than Ga(2) because of its lower coordination, leading to significant covalency associated with O(3). The threshold of the O K-edge (i.e., peak **a**) can therefore serve as a measure of covalency. The higher intensity of peak **a** for $E \parallel b$ than for $E \perp b$ suggests that there is a larger contribution of the covalent bond character along the NW growth direction, associated with the preferential orientation of O(3) bonds. This observation is also consistent with a lower net charge on O(3) relative to O(1) and

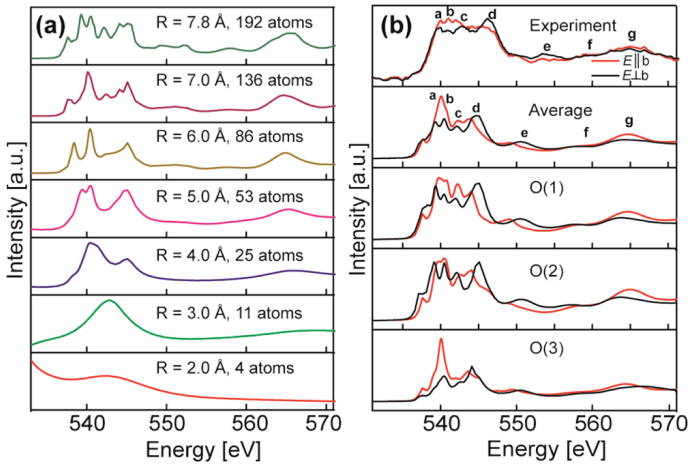

Figure 5.8: Simulations of the polarized O K-edge spectra by FDMNES. (a) Effect of increasing MT radii on the O K-edge spectrum. (b) Comparison of the polarized experimental spectra (top panel) to the calculated overall (average) spectra and the spectra corresponding to different oxygen sites O(1), O(2), and O(3) for $E \parallel b$ (red) and $E \perp b$ (black).

O(2). Other peaks largely consist of similar contributions from O(1) and O(2). The peaks for parallel polarization are slightly shifted to higher energy in both experimental and calculated spectra compared to those for perpendicular polarization, although the total area under the spectral envelope is preserved. This shift can be attributed to different bond lengths along different crystallographic directions, as Ga-O bond is shorter along the b direction due to larger Ga $4s$-O $2sp$ electron interactions compared to a or c axes (vide infra).

In the case of highly anisotropic materials the intensity of the transmitted light depends on spatial orientation of the atomic orbitals. In addition, contribution of specific orbitals to the anisotropy in bonding was estimated by calculating the PDOS using FDMNES code (Figure 5.9).[216] Previous band structure calculations using extended Hückel method[139] and GGA-DFT[215] have shown that the conduction band is predominantly made up of Ga $4s$ orbitals (60%) and that the conduction band minimum at the center of the Brillouin zone (Γ-point) is associated with the Ga(2) atoms. The top of the valence band was found to consist of O $2p$ orbitals, with a width of about 7 eV.[215] These conclusions are in agreement with the semiempirical quantum mechanical calculations,[133] which found that the higher energy region of the valence band is made up entirely of weakly interacting O $2p$ orbitals, while the lower energy part consists of Ga $4s$-O $2p$ bonding states. In contrast, the

tight-binding model-based calculations predicted that Ga $4p$ and $4s$ states spread over the entire valence band.[217] Experimental spectroscopic results supported by PDOS calculations can provide important new evidence about the origin of anisotropy in individual NWs at the molecular level. The bottom three panels of Figure 5.9 show PDOS for the orbitals of the nearest O and Ga atoms on the absorbing O atom for $E \parallel b$ (Figure 5.9a) and $E \perp b$ (Figure 5.9b). These orbital contributions are compared to the overall calculated XANES spectra for the corresponding polarizations (top panels in Figure 5.9). In β-Ga_2O_3, the three different O atoms are located at Wyckoff positions $4i$, and have a point group C_s, as confirmed from the FDMNES calculations. The irreducible representations for the C_s point group are A′ and A″, which define orbitals that can participate in hybridization based on their symmetry (e.g., $p_{x,y}$, d_{xy}, $d_{x^2-y^2}$, and d_{z^2} orbitals for A′, and p_z, d_{xz}, and d_{yz} orbitals for A″, see character table in Appendix G). The O K-edge XANES features can then be assigned for both polarizations based on the molecular orbital theory.[218]

The assignment of the calculated XANES spectrum for $E \perp b$ will be discussed in the following paragraph. Based on the overall spectral density distribution and band shapes, as well as the electric dipole orientational allowedness of the $1s \rightarrow 2p$ transitions in the lab frame,[179] it is evident that X-rays polarized perpendicular to the NW growth direction are probing almost exclusively empty O $2p_z$ orbitals (middle panel in Figure 5.9a). According to the above-mentioned site symmetry considerations, hybridization of O $2p_z$ with O $2p_{x,y}$ and Ga $4p_{x,y}$, $4d_{xy}$, $4d_{x^2-y^2}$, and $4d_{z^2}$ orbitals is symmetry forbidden, while other Ga d orbitals (d_{xz} and d_{yz}) have negligible contribution in the low energy part of the XANES spectrum. The calculated XANES spectrum for $E \parallel b$ polarization appears to have a maximum contribution from the O $2p_{x,y}$ orbitals hybridized with Ga $4p$ and $4d$ orbitals (Figure 5.9b). Given its spatial orientation, O $2p_z$ orbital cannot contribute to the spectrum for $E \parallel b$. The main XANES peaks (**a**-**d**) between -17 and -5 eV are predominantly made up of O $2p_{x,y}$ orbitals, with a contribution from Ga $4p_{x,y}$. These Ga orbitals have a particularly strong contribution to peak **e**. Mixing of O $2p$ states with the metal $4s$ and p states is essential for the covalent bonding compared to mixing with metal $3d$ orbitals,[219] confirming a high degree of covalency in this system.

Higher energy peaks or antibonding states are made up of Ga $4p_{x,y}$ orbitals hybridized with Ga $4d$ orbitals, as per the above symmetry consideration. From this analysis we conclude that stronger hybridization along the NW b direction due to the contribution from more atomic orbitals leads to larger covalent bond character and higher peak **a** and **b** intensities for $E \parallel b$ than $E \perp b$ polarization.[216] Furthermore, from the oxygen PDOS it is evident that O $2p$ orbitals mostly contribute to the XANES spectrum below E_F, suggesting the electron localization in the oxygen p band. This conclusion was further supported by insignificant changes of the simulated XANES spectra upon the inclusion of the core-hole

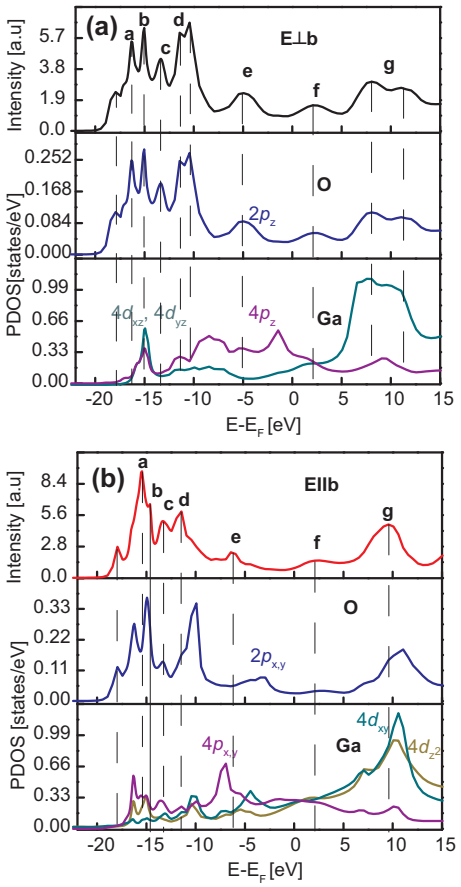

Figure 5.9: Angular momentum projected density of states (PDOS) from the nearest O (middle panels) and Ga (bottom panels) atoms to the absorbing O atom. PDOS corresponding to the symmetry-allowed orbitals are compared to the calculated XANES spectra (top panels) for the electric field vector parallel (a) and perpendicular (b) to the β-Ga_2O_3 *b*-axis. Zero energy corresponds to E_F. Cartesian coordinates x, y, and z correspond to [100], [010], and [001] directions in a monoclinic unit cell, respectively.

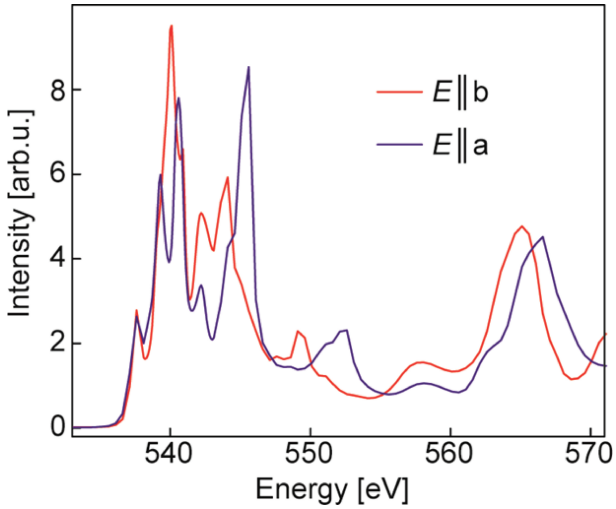

Figure 5.10: Comparison of the calculated O K-edge XANES spectra of β-Ga_2O_3 for E oriented parallel to a (blue) and b (red) crystallographic directions.

effect (see Appendix F, Figure F.2).

Finally, to demonstrate the generality of the valence band electronic structure anisotropy of β-Ga_2O_3 NWs grown along the b crystallographic direction, the O K-edge XANES spectrum for $E \parallel a$ was calculated (Figure 5.10, blue trace). This polarization can also be viewed as $E \perp b$ (in the ab plane), and is compared to the spectrum for $E \parallel b$ (red trace in Figure 5.10). The shape, position, and intensity of the spectral features are clearly different for $E \parallel a$ compared to $E \parallel b$ directions. Comparing the spectrum for $E \parallel a$ with that for $E \perp b$ in the lower energy range (533-545 eV) reveals some change in the relative peak intensity but no significant shift in peak positions (see Appendix F, Figure F.3), whereas for $E \parallel b$ there is a significant shift in peak positions. This result is a further confirmation of the differences in bond lengths along different crystallographic directions, and larger overlap of Ga $4p$ and O $2p$ orbitals along the b axis. Moreover, the XANES spectra in Figures 5.9 and 5.10 suggest that valence band anisotropy is most significant along the NW b axis.

Chapter 6

Conclusions and Future Work

6.1 XAS and XMCD Measurements on Mn Doped GaN Nanowires

The systematic investigations performed throughout the thesis ranging from understanding growth mechanism to probing anisotropic behaviour at the single nanowire level is of fundamental importance in tuning electrical and magnetic properties of one-dimensional nanostructures.

The quantification of the electronic structure and intrinsic spin and orbital magnetic moments of Mn dopants in a single GaN NW at room temperature were done using STXM imaging. Mn ions are present both as isolated dopants in NWs and in secondary phases co-deposited inhomogeneously on the growth substrate. In contrast to recent reports for bulk $Ga_{1-x}Mn_xN$, a large fraction of dopants in NWs retain Mn^{2+} character, suggesting the possibility of hole mediated ferromagnetism in $Ga_{1-x}Mn_xN$ in the nanowire form. The presence of both Mn^{2+}/Mn^{3+} species was further confirmed using atomic multiplet calculations. This work demonstrates strong anisotropy dependence of dilute magnetization in GaN NWs and allows for a control of the dopant exchange interactions within single nanowires or in nanowire assembly, based on their growth and positioning. This orientation dependence was further confirmed through bulk magnetization measurements. The magneto-transport studies in single nanowire was obeying weak-localization theory and show the longer spin coherence length, which is essential for device applications. The results of this study emphasize that in oriented systems, such as NWs, the bulk magnetic measurements can lead to erroneous conclusions regardless of the secondary phase formation. Manipulation

of dilute magnetization in individual semiconductor nanowires at room temperature offers unprecedented opportunities for future spin based device applications.

These results inspire future studies on doped nanowires at even higher spectral and spatial resolution, which may reveal new possibilities for spin manipulation in semiconductor nanostructures[220] and improve the microscopic understanding of dilute magnetic ordering in nanoscale semiconductors. As the exchange interaction depends on the impurity band within the band gap, it is therefore essential to understand the strength of the exchange interaction by tuning the band gap. Therefore, group-V nitrides could be a model system to understand the magnetic exchange interaction as the band gap varies in the order, InN<GaN<AlN. On that note, synthesis of AlN and InN NWs using the CVD method, and incorporation of magnetic dopants under suitable reaction conditions is necessary. However, there are many challenges ahead in achieving p-type carriers in both InN and AlN. In InN, native defects could be a problem in achieving p-type conductivity. Despite its widest band gap and difficulty in achieving p-type doping in AlN, there are few theoretical[31] and experimental reports[221] suggesting room temperature ferromagnetism upon TM incorporation. With the development and optimization of nanowire growth and assembly techniques, including the Langmuir-Blodgett technique[222] and superlattice nanowire pattern transfer,[223] the potential for fabrication of practical nanowire spintronic devices could become a reality.

6.2 β-Ga_2O_3 Nanowire Growth and Anisotropy

The pure monoclinic β-Ga_2O_3 nanowires with high aspect ratio and faceted morphology were produced by vapor-solid method. The HRTEM and SAED analysis confirmed that NWs grew along the [010] or b-axis. The crystal orientation and lattice arrangement were consistent with crystal plane models for the monoclinic phase. High aspect ratio and faceted morphologies were observed under high temperature, low precursor concentration, and high carrier gas flow conditions, as expected for the vapor-solid growth process.[138] These findings may be applied to other crystal systems, particularly complex metal oxides, to explore shape tuning and faceted nanowire growth.

This work demonstrated strong electronic structure anisotropy in individual β-Ga_2O_3 NWs, grown along the crystallographic b direction, using linearly polarized X-ray absorption in the STXM configuration. The O K-edge XANES spectrum shows large linear dichroism compared to Ga the L_3-edge spectrum, which is attributed to different spatial orientation and symmetry of the corresponding atomic orbitals. The theoretical calculations of the O K-edge XANES spectra for $E \parallel b$ and $E \perp b$ polarizations in the framework of multiple scattering theory are in good agreement with the experimental spectra, allowing for identification

of the contribution of different oxygen atoms to the linear dichroism. These simulations revealed the largest degree of the covalent bond character along the NW growth direction, associated with the preferential orientation of O(3) bonds. The specific orbital contributions to the electronic structure anisotropy were quantified by comparing the relevant PDOS of the nearest O and Ga atoms to the calculated O K-edge spectra. The O K-edge XANES spectrum for $E \parallel b$ polarization has a maximum contribution from the O $2p_{x,y}$ orbitals, and for $E \perp b$ polarization from O $2p_z$ orbital. The oxygen site symmetry allows for hybridization between O $2p$ and Ga $4p$ orbitals along the b-axis, which is largely responsible for the observed dichroism, and is essential for covalent bonding in these NWs.[216] The results of this work provide the key components for understanding the origin of anisotropy in single β-Ga_2O_3 NWs, and allow for the prediction of the electronic structure and ultimately physical properties for different NW growth directions. Tuning the electronic structure through the manipulation of the growth direction can influence the properties of transparent metal oxide NWs for new optoelectronic, photovoltaic and sensing applications.

In summary, this thesis provides new insight into the electronic structure and magnetization anisotropy in wide band gap semiconductor NWs, which was studied quantitatively using element specific X-ray absorption spectro-microscopy technique at a single nanowire level. This work has a fundamental significance in terms of understanding both crystalline and orbital origin of anisotropy through nanowire growth direction and dopant incorporation. Tuning of nanowire properties such as electrical and magnetic properties via controllable growth has not yet been addressed thoroughly. This is an important step in exploiting the nanowire growth for future optical and magnetic device applications.

APPENDICES

Appendix A

Formulation of Exchange Mechanisms

The interaction between a pair of electron spins $\boldsymbol{s_{ij}}$ in a many electronic system can be described using a Heisenberg Hamiltonian:

$$H_{ex} = -\sum_{ij} J_{ij} \boldsymbol{s_i} \cdot \boldsymbol{s_j} \tag{A.1}$$

The term H_{ex} is the scalar product of vector spin operators $\boldsymbol{s_i}$ and $\boldsymbol{s_j}$. Hence, the exchange term J_{ij} is positive favouring the parallel coupling of electron spins of neighbouring atoms, which lead to ferromagnetism. If J_{ij} is negative favouring the antiparallel spin coupling to form covalent bonding and leads to antiferromagnetism. In order to get the product of spin operators in eq A.1, magnetic ions should be far enough so that their electronic wave function overlapping is negligible. In addition, angular momentum of each ion consists of both spin and orbital components, therefore the exchange term in the spin Hamiltonian may depend on the absolute value of the relative spin orientations.[224]

In the case of superexchange interaction the sign of exchange term J_{ij} can be determined by the cation-anion-cation bonding and the d-electron configuration on the transition metal. The 180° angle between cation-anion-cation with both the metal orbitals either filled or empty lead to antiferromagnetism. On the other hand if it is 90°, ferromagnetic interaction will dominate.[26]

Appendix B

Magnetocrystalline Anisotropy

The mechanism by which the magnetization align itself along a certain preferred crystallographic direction is the magnetocrystalline anisotropy (MCA). The possible origin of MCA is spin-orbit coupling. The energy required to overcome from the spin-orbit coupling or to rotate domain of spin system away from the easy axis is the magnetocrystalline energy. When the spin spin system is rotated so as the orbit due to coupling between them. However, orbital has a stronger coupling to the lattice, hence resisting the rotation of spin. This is schematically illustrated in Figure B.1. The spin moments aligned vertically i.e, easy axis (Figure B.1a), along with the orbital component and they are not spherical due to the spin-orbit coupling, aligned along the long axis or horizontal axis. This is the most favorable condition of alignment of orbital moment for a given crystal system. Figure B.1b illustrate the forceful rotation of spin axis along the horizontal direction by applying external magnetic field. Also it can be seen in Figure B.1b that, orbital moment detached from the lattice and no favourable overlap.[26,193]

The symmetry of the MCA is same as that of crystal symmetry, therefore the anisotropy energy E can be formulated as series expansion of directional cosines, α_i, of the saturation magnetization relative to the crystal axis;

$$E = K_1(\alpha_1^2\alpha_1^2 + \alpha_2^2\alpha_3^2 + \alpha_3^2\alpha_1^2) + K_2(\alpha_1^2\alpha_2^2\alpha_3^2) + \cdots \tag{B.1}$$

where $K_1, K_2...$ are the anisotropy constants. The E is the anisotropy energy stored in the crystal before rotating the magnetization away from the easy axis and it is important to note that E is an even function of the direction cosines, and is invariant under interchange of the $\alpha_i s$ among themselves.[26]

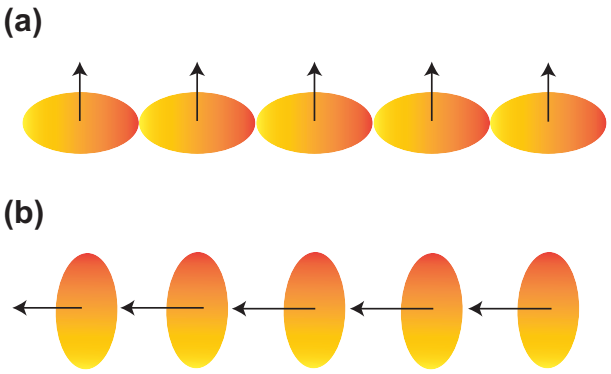

Figure B.1: The orientation of spin-orbit degrees of freedom along an easy axis and rotated away from an easy axis (b).

In case of hexagonal crystal structure, the easy axis is along the crystallographic c-axis . The crystal symmetry causes the uniaxial anisotropy energy and its angular dependence can be derived by considering the angle θ between magnetization vector and hexagonal axis (Figure B.2). Anisotropy energy in this crystal system is,

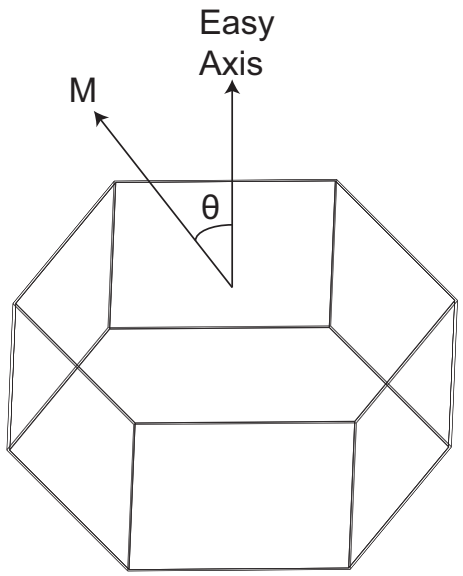

Figure B.2: The magnetocrystalline anisotropy in hexagonal crystal structure with easy axis of magnetization along c direction and θ is the angle between magnetization vector and hexagonal axis

$$E = K_1 \sin^2\theta + K_2 \sin^2\theta + ... \tag{B.2}$$

In all crystalline materials the MCA decreases as temperature increases and it tends to zero at T_C. It is also expected as there is no preferred spin orientation in paramagnetic system.

Appendix C

CTM4XAS Program

The front panel of the CTM4XAS version 5.5 consists of various sections to insert the input parameters to reproduce experimental spectra.

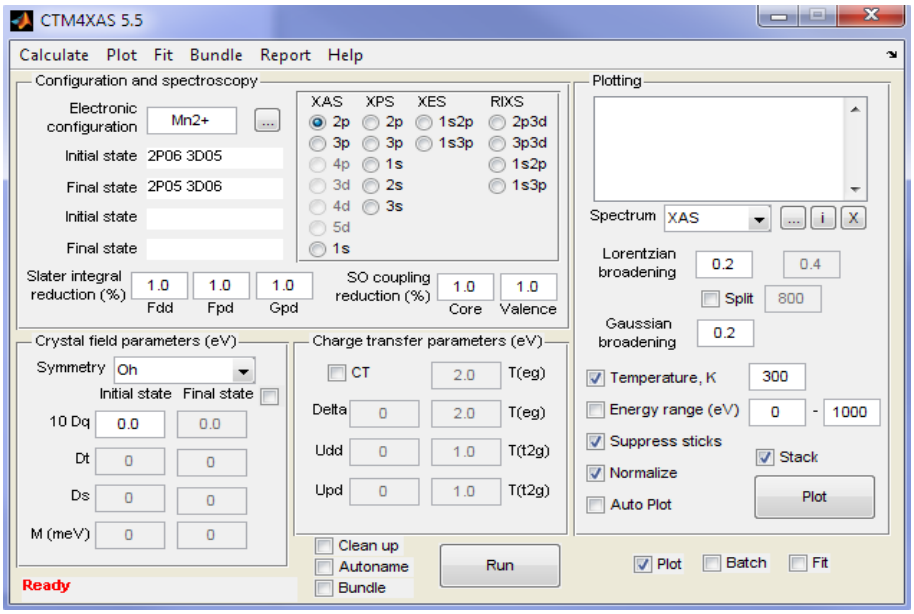

Figure C.1: CTM4XAS front panel with various parameters. The front panel is divided into four parts, the configuration and the atomic calculations at the top, the crystal field parameters (middle, left), the charge transfer parameters (middle, right) and the plotting options (bottom).

From this windows interface (Figure C.1) all the calculations can be performed and resulting spectra will be plotted and saved automatically. On the top part of the screen elements for which calculations will be done was chosen, including its oxidation state. The bottom part consists of Slater-Condon terms which involve Coulomb repulsion and exchange terms. F_{dd} is the d-d repulsive term given by Slater integrals and in Hartree-Fock units. F_{pd} is the Slater integral for the core and valence electron coupling. G_{pd} exchange Slater integrals. For all these integrals number can be chosen between 0-1.5 during the calculations. Similarly, the spin-orbit coupling term and default value of 1 is always used for simulations, as it is not screened. The middle left panel is to insert the crystal field parameters for different site symmetries such as O_h, T_d and D_{4h} and it can be determined from optical spectroscopy measurements. The bottom panel is the plotting option with various adjustable parameters to simulate the experimental conditions, such as temperature and energy range.[169]

Appendix D

Mn L-edge Analysis

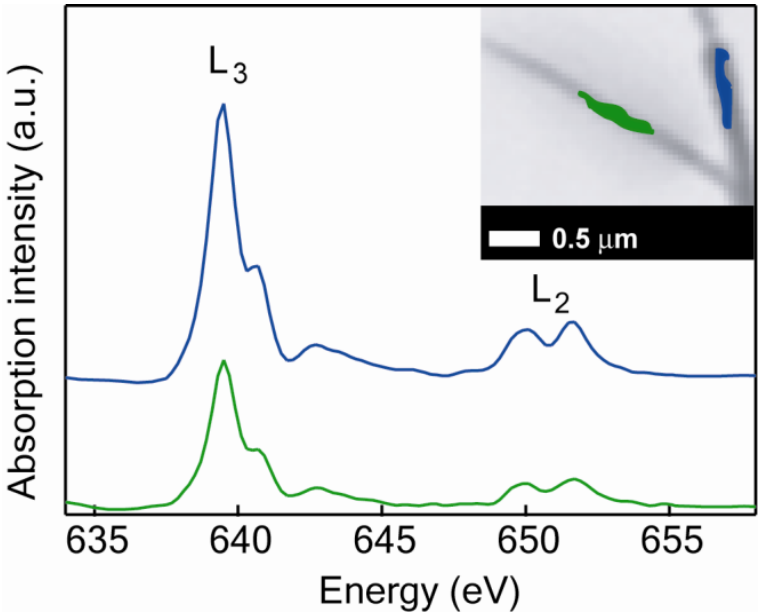

Figure D.1: Mn $L_{2,3}$-edge X-ray absorption spectra of single $Ga_{0.95}Mn_{0.05}N$ nanowires shown in the inset. The colors of the spectra correspond to the colors of arbitrarily selected areas of the nanowires in the image. The spectra are in very good agreement with those shown in Figure 3.5a for the entire nanowires, indicating homogeneous Mn speciation throughout the nanowires.[184]

Appendix E

Mn K-edge Analysis

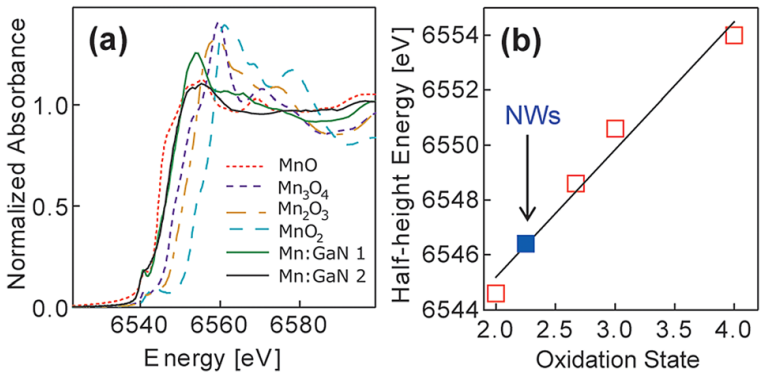

Figure E.1: Mn K-edge Analysis. (a) Mn K-edge XANES spectra of $Ga_{0.95}Mn_{0.05}N$ NWs at two different regions of the growth substrate (1 and 2), and the reference compounds (as indicated in the graph). (b) Half-height energy analysis of the average oxidation state of Mn dopants in GaN NWs.[187]

Appendix F

O K-edge Polarized XANES

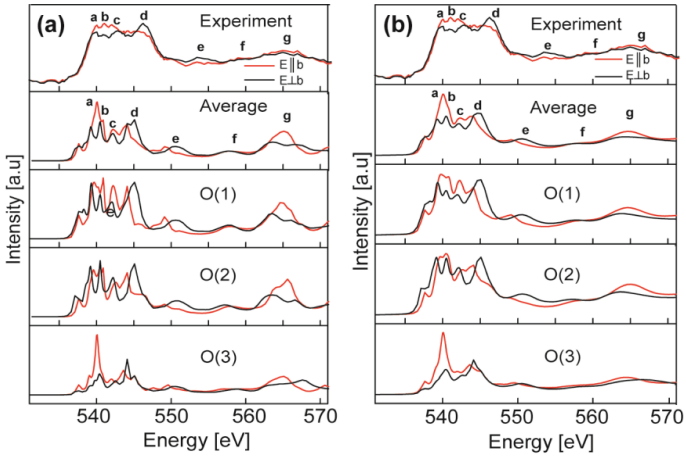

Figure F.1: (a) Comparison of the O K-edge experimental spectra of β-Ga_2O_3 (top panel) with the calculated raw spectra without the convolution of the arctangent function given by eq 2.18 in the main text (lower four panels), for E parallel (red trace) and perpendicular (black trace) to the b axis. Lower panels show the contributions of different oxygen sites O(1), O(2), and O(3) to the overall spectra labelled as Average. (b) Calculated XANES spectra obtained by convolution of the corresponding raw spectra in (a) with the arctangent function defined by eq 2.18 in the main text. The experimental spectra are shown in the top panel for comparison.[216]

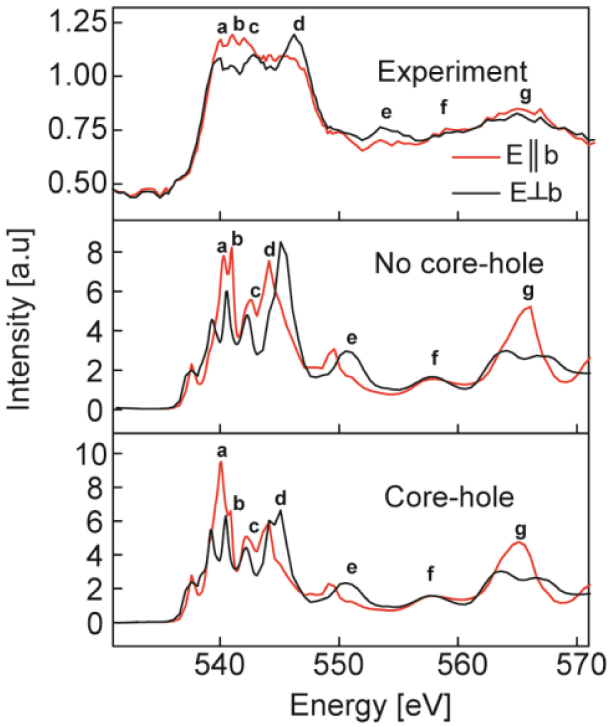

Figure F.2: Comparison of the experimental O K-edge XANES spectra of β-Ga_2O_3 (top panel) with the calculated spectra with (bottom panel) and without (middle panel) the consideration of the core-hole effect for $E \parallel b$ (red trace) and $E \perp b$ (black trace). All peaks are well reproduced without considering the core-hole effect, and we did not observe any significant changes in the peak positions and intensities. Together with the oxygen PDOS for the $2p$ orbitals below E_F, this result suggests the localization of the extra electron in the oxygen p band.[216]

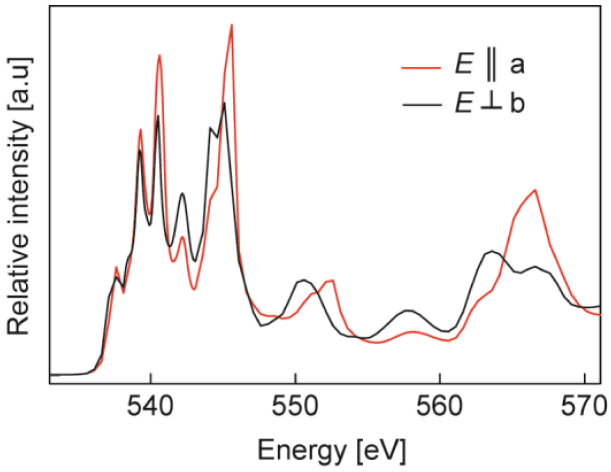

Figure F.3: Comparison between the calculated O K-edge XANES spectra of β-Ga_2O_3 for $E \parallel a$ (ab plane) and $E \perp b$ (bc plane). In the lower energy range (533 eV–545 eV) there is some change in the relative peak intensity but no significant shift in peak positions.[216]

Appendix G

C_S Point Group Symmetry Character Tables

Abelian, 2 irreducible representations

	E	σ_h	linear functions, rotations	quadratic
A′	1	1	x, y, R_z	x^2, y^2, z^2, xy
A″	1	-1	z, R_x, R_y	yz, xz

Table G.1: Character table for C_s point group

Appendix H

FDMNES Code to Calculate O K-edge XANES

! Indata file for the fdmnes program.
! Calculation of the oxygen K edge in monoclinic gallium oxide.
! Multiple scatering method.
Output file name.
Filout
xanout/test_stand/full_Ga_parallel
Energy range with step E_{min}, step, $E_{intermediate}$, step... in eV.
Range
-10. 0.5 -5. 0.1 0. 0.5 28.
MS calculations within the Green function formalism.
Green
Absorption threshold, K, L... etc.
Edge
K
Cluster or MT radius in $\mathrm{\AA}$.
Radius
7.8
Different individual polarization.
Polarize
0.0 1.0 0.0
Space group of the crystal system.

Spgroup
C12/m1
Expansion of spherical harmonics.
lmax
2
Crystal structure.
Crystal
Unit cell parameters, a, b, c, α, β, and γ.
12.214 3.0371 5.7981 90 103.7 90
First column corresponds to atomic number (Z) of the element followed by position coordinates of the atoms, x, y, and z.
31 0.0905 0.0000 0.7946
31 0.1586 0.5000 0.3140
8 0.1645 0.0000 0.1098
8 0.1733 0.0000 0.5632
8 -0.0040 0.5000 0.2566
Absorbing atom number.
Absorber
3 4 5
Calculate energy corresponds to photon energy.
energpho
DOS and its integral for any harmonics projected on the central atom.
Density
state_all
Memory_save
End

Appendix I

Cr Doped $BaTiO_3$ Nanocrystals

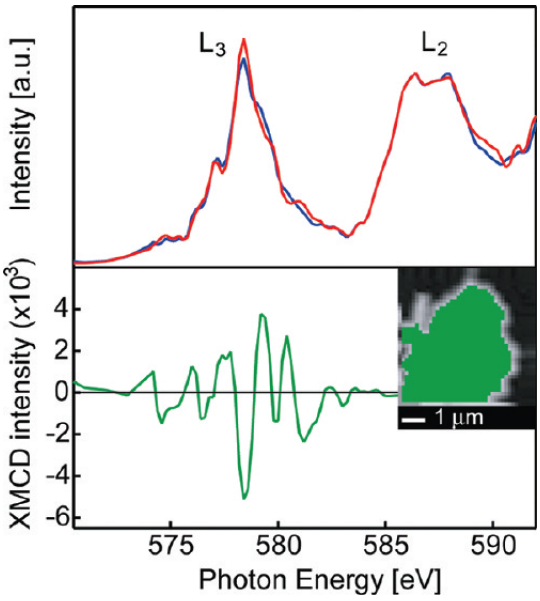

Figure I.1: Cr $L_{2,3}$-edge XANES (top) and XMCD (bottom) in Cr doped $BaTiO_3$ nanocrystals. The non-zero XMCD signal indicates that magnetic ordering comes from the Cr^{3+} dopant exchange interactions.[225]

Appendix J

Donor-acceptor Pair Recombination in γ-Ga_2O_3 Nanocrystals

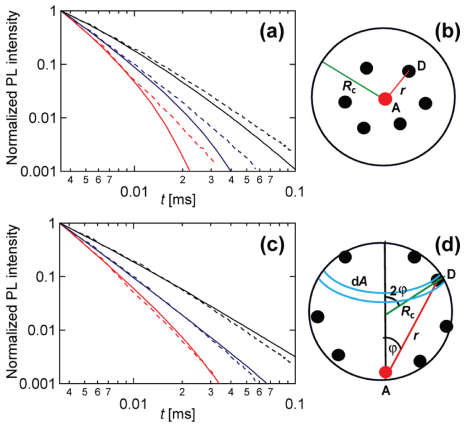

Figure J.1: Photoluminescence decay dynamics in γ-Ga_2O_3 nanocrystals. Solid red, blue and black lines correspond to experimental PL decay curves for nanocrystals of radii, R_c = 1.6, 2.1 and 3.0 nm, respectively. The dashed lines corresponds to calculated PL decay curves for 3-D (a), where donors reside inside the sphere as shown schematically in (b), and 2-D (c), where, donors on the surface of nanocrystals, as shown schematically in (d). 2-D model gives good agreement with experiment for naocrystals of all sizes.[226]

Appendix K

Cr Doped In_2O_3 Nanocrystals

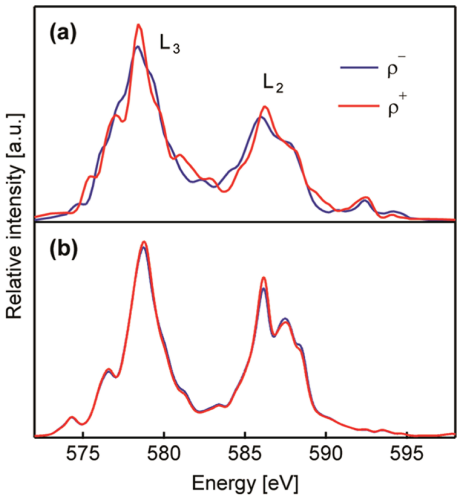

Figure K.1: (a) Cr $L_{2,3}$-edge X-ray absorption spectra of 3% Cr^{3+}:bcc-In_2O_3 nanocrystalline film collected using circularly polarized ρ^- (blue) and ρ^+ (red) photons in STXM configuration. (b) Calculated Cr $L_{2,3}$-edge circularly polarized X-ray absorption spectra (ρ^-, blue; ρ^+, red) for C_{3i} symmetry. The spectra were calculated using CTM4XAS package.[119]

Appendix L

Charge Transfer Ferromagnetism in Mn Doped In_2O_3 Nanocrystals

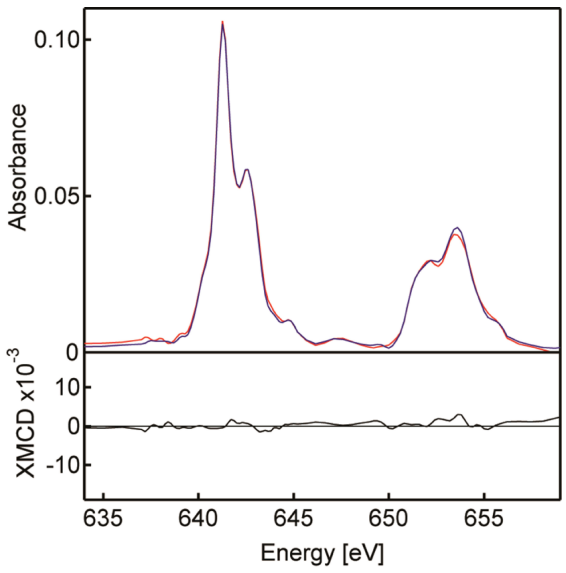

Figure L.1: Manganese $L_{2,3}$-edge X-ray absorption spectra of ferromagnetic 9.5% Mn:bcc-In_2O_3 nanocrystalline film collected by STXM using left (blue line) and right (red line) circularly polarized photons (top). The resulting XMCD spectrum (bottom) shows no distinct features.[227]

Appendix M

Eu $M_{4,5}$-edge XANES in Ga_2O_3 Nanocrystals

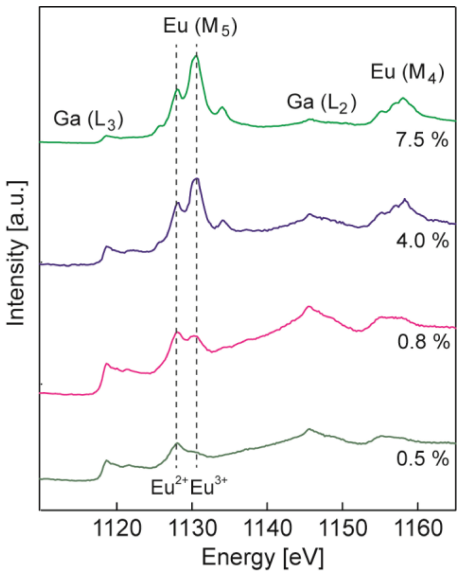

Figure M.1: Eu $M_{4,5}$-edge spectra of Eu-doped Ga_2O_3 nanocrystals synthesized at 300 °C, having different doping concentrations. The positions of M_5-edge peaks for Eu^{2+} and Eu^{3+} are indicated in the graph. An increase in the doping concentration leads to a decrease in the fraction of Eu^{2+}, consistent with Eu L_3-edge spectroscopy.[228]

References

[1] Žutić, I.; Fabian, J.; Das Sarma, S. *Rev. Mod. Phys.* **2004**, *76*, 323–410.

[2] Fert, A. *Rev. Mod. Phys.* **2008**, *80*, 1517–1530.

[3] Wolf, S.; Awschalom, D.; Buhrman, R.; Daughton, J.; Von Molnar, S.; Roukes, M.; Chtchelkanova, A. Y.; Treger, D. *Science* **2001**, *294*, 1488–1495.

[4] Ando, K. *Science* **2006**, *312*, 1883–1885.

[5] Pla, J. J.; Tan, K. Y.; Dehollain, J. P.; Lim, W. H.; Morton, J. J.; Zwanenburg, F. A.; Jamieson, D. N.; Dzurak, A. S.; Morello, A. *Nature* **2013**, *496*, 334–338.

[6] Baibich, M. N.; Broto, J. M.; Fert, A.; Van Dau, F. N.; Petroff, F.; Etienne, P.; Creuzet, G.; Friederich, A.; Chazelas, J. *Phys. Rev. Lett.* **1988**, *61*, 2472.

[7] Binasch, G.; Grünberg, P.; Saurenbach, F.; Zinn, W. *Phys. Rev. B* **1989**, *39*, 4828.

[8] Sato, K.; Bergqvist, L.; Kudrnovský, J.; Dederichs, P. H.; Eriksson, O.; Turek, I.; Sanyal, B.; Bouzerar, G.; Katayama-Yoshida, H.; Dinh, V. A.; Fukushima, T.; Kizaki, H.; Zeller, R. *Rev. Mod. Phys.* **2010**, *82*, 1633–1690.

[9] Datta, S.; Das, B. *Appl. Phys. Lett.* **1990**, *56*, 665–667.

[10] Sarma, S. D. *Amer. Sci.* **2001**, *89*, 516.

[11] Sarma, S. D. *Nat. Mater.* **2003**, *2*, 292–294.

[12] Novák, V.; Olejník, K.; Wunderlich, J.; Cukr, M.; Vỳbornỳ, K.; Rushforth, A. W.; Edmonds, K. W.; Campion, R. P.; Gallagher, B. L.; Sinova, J.; Jungwirth, T. *Phys. Rev. Lett.* **2008**, *101*, 077201.

[13] Kaminski, A.; Sarma, S. D. *Phys. Rev. Lett.* **2002**, *88*, 247202.

[14] Dietl, T.; Ohno, H.; Matsukura, F.; Cibert, J.; Ferrand, D. *Science* **2000**, *287*, 1019–1022.

[15] Sonoda, S.; Shimizu, S.; Sasaki, T.; Yamamoto, Y.; Hori, H. *J. Cryst. Growth* **2002**, *237-239*, 1358 – 1362.

[16] Ueda, K.; Tabata, H.; Kawai, T. *Appl. Phys. Lett.* **2001**, *79*, 988–990.

[17] Matsumoto, Y.; Murakami, M.; Shono, T.; Hasegawa, T.; Fukumura, T.; Kawasaki, M.; Ahmet, P.; Chikyow, T.; Koshihara, S.-Y.; Koinuma, H. *Science* **2001**, *291*, 854–856.

[18] Venkatesan, M.; Fitzgerald, C.; Coey, J. *Nature* **2004**, *430*, 630.

[19] Nakamura, S.; Chichibu, S. F. *Introduction to Nitride Semiconductor Blue Lasers and Light-Emitting Diodes*; CRC Press, 2000.

[20] Nakamura, S.; Pearton, S.; Fasol, G. *The Blue Laser Diode*; Springer Berlin, 2000.

[21] Morkoç, H.; Di Carlo, A.; Cingolani, R. *Solid-State Electron.* **2002**, *46*, 157–202.

[22] Pearton, S.; Ren, F.; Zhang, A.; Lee, K. *Mater. Sci. Eng., R.* **2000**, *30*, 55–212.

[23] Pearton, S. J.; Abernathy, C. R.; Overberg, M. E.; Thaler, G. T.; Norton, D. P.; Theodoropoulou, N.; Hebard, A. F.; Park, Y. D.; Ren, F.; Kim, J.; Boatner, L. A. *J. Appl. Phys.* **2003**, *93*, 1–13.

[24] Brandt, O.; Yang, H.; Kostial, H.; Ploog, K. H. *Appl. Phys. Lett.* **1996**, *69*, 2707–2709.

[25] Katayama-Yoshida, H.; Kato, R.; Yamamoto, T. *J. Cryst. Growth* **2001**, *231*, 428–436.

[26] Spaldin, N. A. *Magnetic Materials: Fundamentals and Applications*; Cambridge University Press, 2010.

[27] Liu, C.; Yun, F.; Morkoc, H. *J. Mater. Sci.: Mater. Electron.* **2005**, *16*, 555–597.

[28] Ruderman, M. A.; Kittel, C. *Phys. Rev.* **1954**, *96*, 99.

[29] Zener, C. *Phys. Rev.* **1951**, *81*, 440.

[30] Sato, K.; Dederichs, P. H.; Katayama-Yoshida, H.; Kudrnovský, J. *J. Phys.: Condens. Matter* **2004**, *16*, S5491.

[31] Litvinov, V. I.; Dugaev, V. K. *Phys. Rev. Lett.* **2001**, *86*, 5593.

[32] Mahadevan, P.; Zunger, A. *Appl. Phys. Lett.* **2004**, *85*, 2860–2862.

[33] Virot, F.; Hayn, R.; Boukortt, A. *J. Phys.: Condens. Matter* **2011**, *23*, 025503.

[34] Boukortt, A.; Hayn, R.; Virot, F. *Phys. Rev. B* **2012**, *85*, 033302.

[35] van Schilfgaarde, M.; Mryasov, O. *Phys. Rev. B* **2001**, *63*, 233205.

[36] Popovic, Z. S.; Satpathy, S.; Mitchel, W. *Phys. Rev. B* **2004**, *70*, 161308.

[37] Cui, X.; Delley, B.; Freeman, A.; Stampfl, C. *Phys. Rev. B* **2007**, *76*, 045201.

[38] Nishizawa, K.; Sakai, O.; Suzuki, S. *Physica B* **2000**, *281*, 468–469.

[39] Schliemann, J.; König, J.; MacDonald, A. *Phys. Rev. B* **2001**, *64*, 165201.

[40] Schliemann, J.; König, J.; Lin, H.-H.; MacDonald, A. H. *Appl. Phys. Lett.* **2001**, *78*, 1550–1552.

[41] König, J.; Lin, H.-H.; MacDonald, A. H. *Phys. Rev. Lett.* **2000**, *84*, 5628.

[42] Jungwirth, T.; Atkinson, W.; Lee, B.; MacDonald, A. *Phys. Rev. B* **1999**, *59*, 9818.

[43] Lee, B.; Jungwirth, T.; MacDonald, A. *Phys. Rev. B* **2000**, *61*, 15606.

[44] Dietl, T.; König, J.; MacDonald, A. *Phys. Rev. B* **2001**, *64*, 241201.

[45] Abolfath, M.; Jungwirth, T.; Brum, J.; MacDonald, A. *Phys. Rev. B* **2001**, *63*, 054418.

[46] König, J.; Jungwirth, T.; MacDonald, A. *Phys. Rev. B* **2001**, *64*, 184423.

[47] Graf, T.; Gjukic, M.; Brandt, M. S.; Stutzmann, M.; Ambacher, O. *Appl. Phys. Lett.* **2002**, *81*, 5159–5161.

[48] Gebicki, W.; Strzeszewski, J.; Kamler, G.; Szyszko, T.; Podsiadlo, S. *Appl. Phys. Lett.* **2000**, *76*, 3870.

[49] Zajac, M.; Doradzinski, R.; Gosk, J.; Szczytko, J.; Lefeld-Sosnowska, M.; Kaminska, M.; Twardowski, A.; Palczewska, M.; Grzanka, E.; Gebicki, W. *Appl. Phys. Lett.* **2001**, *78*, 1276.

[50] Zając, M.; Gosk, J.; Kamińska, M.; Twardowski, A.; Szyszko, T.; Podsiadło, S. *Appl. Phys. Lett.* **2001**, *79*, 2432–2434.

[51] Soo, Y.; Kioseoglou, G.; Kim, S.; Huang, S.; Kao, Y.; Kuwabara, S.; Owa, S.; Kondo, T.; Munekata, H. *Appl. Phys. Lett.* **2001**, *79*, 3926–3928.

[52] Kuwabara, S.; Kondo, T.; Chikyow, T.; Ahmet, P.; Munekata, H. *Jpn. J. Appl. Phys., Part 2* **2001**, *40*, L724.

[53] Thaler, G. T.; Overberg, M. E.; Gila, B.; Frazier, R.; Abernathy, C. R.; Pearton, S. J.; Lee, J. S.; Lee, S. Y.; Park, Y. D.; Khim, Z. G.; Kim, J.; Ren, F. *Appl. Phys. Lett.* **2002**, *80*, 3964–3966.

[54] Overberg, M. E.; Abernathy, C. R.; Pearton, S. J.; Theodoropoulou, N. A.; McCarthy, K. T.; Hebard, A. F. *Appl. Phys. Lett.* **2001**, *79*, 1312–1314.

[55] Chitta, V.; Coaquira, J.; Fernandez, J.; Duarte, C.; Leite, J.; Schikora, D.; As, D.; Lischka, K.; Abramof, E. *Appl. Phys. Lett.* **2004**, *85*, 3777–3779.

[56] Overberg, M.; Gila, B. P.; Thaler, G. T.; Abernathy, C. R.; Pearton, S. J.; Theodoropoulou, N. A.; McCarthy, K. T.; Arnason, S. B.; Hebard, A. F.; Chu, S. N. G.; Wilson, R. G.; Zavada, J. M.; Park, Y. D. *J. Vac. Sci. Technol. B* **2002**, *20*, 969–973.

[57] Zajac, M.; Gosk, J.; Grzanka, E.; Kaminska, M.; Twardowski, A.; Strojek, B.; Szyszko, T.; Podsiadlo, S. *J. Appl. Phys.* **2003**, *93*, 4715–4717.

[58] Edmonds, K. W.; Farley, N. R. S.; Johal, T. K.; Campion, R. P.; Gallagher, B. L.; Foxon, C. T.; van der Laan, G. *J. Appl. Phys.* **2004**, *95*, 7166–7168.

[59] Zhong, Z.; Fang, Y.; Lu, W.; Lieber, C. M. *Nano Lett.* **2005**, *5*, 1143–1146.

[60] Yang, C.; Zhong, Z.; Lieber, C. M. *Science* **2005**, *310*, 1304–1307.

[61] Thelander, C.; Agarwal, P.; Brongersma, S.; Eymery, J.; Feiner, L. F.; Forchel, A.; Scheffler, M.; Riess, W.; Ohlsson, B. J.; Gösele, U.; Samuelson, L. *Mater. Today* **2006**, *9*, 28–35.

[62] Thelander, C.; Mrtensson, T.; Bjork, M. T.; Ohlsson, B. J.; Larsson, M. W.; Wallenberg, L. R.; Samuelson, L. *Appl. Phys. Lett.* **2003**, *83*, 2052–2054.

[63] Lu, W.; Xie, P.; Lieber, C. M. *IEEE Trans. Electron Devices* **2008**, *55*, 2859–2876.

[64] Lu, W.; Xiang, J.; Timko, B. P.; Wu, Y.; Lieber, C. M. *Proc. Natl. Acad. Sci. U. S. A.* **2005**, *102*, 10046–10051.

[65] Lu, W.; Lieber, C. M. *Nat. Mater.* **2007**, *6*, 841–850.

[66] Goldberger, J.; Hochbaum, A. I.; Fan, R.; Yang, P. *Nano Lett.* **2006**, *6*, 973–977.

[67] Cui, Y.; Zhong, Z.; Wang, D.; Wang, W. U.; Lieber, C. M. *Nano Lett.* **2003**, *3*, 149–152.

[68] Bryllert, T.; Wernersson, L.-E.; Löwgren, T.; Samuelson, L. *Nanotechnology* **2006**, *17*, S227.

[69] Fasth, C.; Fuhrer, A.; Björk, M. T.; Samuelson, L. *Nano Lett.* **2005**, *5*, 1487–1490.

[70] Haraguchi, K.; Katsuyama, T.; Hiruma, K. *J. Appl. Phys.* **1994**, *75*, 4220–4225.

[71] Huang, M. H.; Mao, S.; Feick, H.; Yan, H.; Wu, Y.; Kind, H.; Weber, E.; Russo, R.; Yang, P. *Science* **2001**, *292*, 1897–1899.

[72] Wang, J.; Gudiksen, M. S.; Duan, X.; Cui, Y.; Lieber, C. M. *Science* **2001**, *293*, 1455–1457.

[73] Duan, X.; Huang, Y.; Cui, Y.; Wang, J.; Lieber, C. M. *Nature* **2001**, *409*, 66–69.

[74] Gudiksen, M. S.; Lauhon, L. J.; Wang, J.; Smith, D. C.; Lieber, C. M. *Nature* **2002**, *415*, 617–620.

[75] Johnson, J. C.; Choi, H.-J.; Knutsen, K. P.; Schaller, R. D.; Yang, P.; Saykally, R. J. *Nat. Mater.* **2002**, *1*, 106–110.

[76] Duan, X.; Huang, Y.; Agarwal, R.; Lieber, C. M. *Nature* **2003**, *421*, 241–245.

[77] Johnson, J. C.; Yan, H.; Yang, P.; Saykally, R. J. *J. Phys. Chem. B* **2003**, *107*, 8816–8828.

[78] Law, M.; Sirbuly, D. J.; Johnson, J. C.; Goldberger, J.; Saykally, R. J.; Yang, P. *Science* **2004**, *305*, 1269–1273.

[79] Hayden, O.; Agarwal, R.; Lieber, C. M. *Nat. Mater.* **2006**, *5*, 352–356.

[80] Nakayama, Y.; Pauzauskie, P. J.; Radenovic, A.; Onorato, R. M.; Saykally, R. J.; Liphardt, J.; Yang, P. *Nature* **2007**, *447*, 1098–1101.

[81] Qian, F.; Li, Y.; Gradečak, S.; Park, H.-G.; Dong, Y.; Ding, Y.; Wang, Z. L.; Lieber, C. M. *Nat. Mater.* **2008**, *7*, 701–706.

[82] Yan, R.; Gargas, D.; Yang, P. *Nat. Photonics* **2009**, *3*, 569–576.

[83] Garnett, E. C.; Brongersma, M. L.; Cui, Y.; McGehee, M. D. *Annu. Rev. Mater. Res.* **2011**, *41*, 269–295.

[84] Law, M.; Greene, L. E.; Johnson, J. C.; Saykally, R.; Yang, P. *Nat. Mater.* **2005**, *4*, 455–459.

[85] Kempa, T. J.; Tian, B.; Kim, D. R.; Hu, J.; Zheng, X.; Lieber, C. M. *Nano Lett.* **2008**, *8*, 3456–3460.

[86] Garnett, E. C.; Yang, P. *J. Am. Chem. Soc.* **2008**, *130*, 9224–9225.

[87] Baxter, J. B.; Aydil, E. S. *Appl. Phys. Lett.* **2005**, *86*, 053114.

[88] Li, Y.; Tan, B.; Wu, Y. *Nano Lett.* **2008**, *8*, 265–270.

[89] Kim, H.; Cho, J. *Nano Lett.* **2008**, *8*, 3688–3691.

[90] Huang, J. Y.; Zhong, L.; Wang, C. M.; Sullivan, J. P.; Xu, W.; Zhang, L. Q.; Mao, S. X.; Hudak, N. S.; Liu, X. H.; Subramanian, A.; Fan, H.; Qi, L.; Kushima, A.; Li, J. *Science* **2010**, *330*, 1515–1520.

[91] Chan, C. K.; Zhang, X. F.; Cui, Y. *Nano Lett.* **2008**, *8*, 307–309.

[92] Cui, L.-F.; Ruffo, R.; Chan, C. K.; Peng, H.; Cui, Y. *Nano Lett.* **2008**, *9*, 491–495.

[93] Wang, X.; Song, J.; Liu, J.; Wang, Z. L. *Science* **2007**, *316*, 102–105.

[94] Wang, Z. L.; Song, J. *Science* **2006**, *312*, 242–246.

[95] Wan, Q.; Wang, T. H. *Chem. Commun.* **2005**, 3841–3843.

[96] Tian, B.; Cohen-Karni, T.; Qing, Q.; Duan, X.; Xie, P.; Lieber, C. M. *Science* **2010**, *329*, 830–834.

[97] Qing, Q.; Jiang, Z.; Xu, L.; Gao, R.; Mai, L.; Lieber, C. M. *Nat. Nanotechnol.* **2014**, *9*, 142–147.

[98] Patolsky, F.; Lieber, C. M. *Mater. Today* **2005**, *8*, 20–28.

[99] Kolmakov, A.; Moskovits, M. *Annu. Rev. Mater. Res.* **2004**, *34*, 151–180.

[100] Kim, A.; Ah, C. S.; Yu, H. Y.; Yang, J.-H.; Baek, I.-B.; Ahn, C.-G.; Park, C. W.; Jun, M. S.; Lee, S. *Appl. Phys. Lett.* **2007**, *91*, 3901.

[101] Jiang, Z.; Qing, Q.; Xie, P.; Gao, R.; Lieber, C. M. *Nano Lett.* **2012**, *12*, 1711–1716.

[102] Cui, Y.; Wei, Q.; Park, H.; Lieber, C. M. *Science* **2001**, *293*, 1289–1292.

[103] Law, M.; Goldberger, J.; Yang, P. *Annu. Rev. Mater. Res.* **2004**, *34*, 83–122.

[104] Chen, L.; Lu, W.; Lieber, C. M. *Semiconductor Nanowires: From Next-Generation Electronics to Sustainable Energy*; The Royal Society of Chemistry, 2015; pp 1–53.

[105] Li, Y.; Qian, F.; Xiang, J.; Lieber, C. M. *Mater. Today* **2006**, *9*, 18–27.

[106] Wang, Q.; Sun, Q.; Jena, P. *Phys. Rev. Lett.* **2005**, *95*, 167202.

[107] Choi, H.-J.; Seong, H.-K.; Chang, J.; Lee, K.-I.; Park, Y.-J.; Kim, J.-J.; Lee, S.-K.; He, R.; Kuykendall, T.; Yang, P. *Adv. Mater.* **2005**, *17*, 1351–1356.

[108] Wagner, R. S.; Ellis, W. C. *Appl. Phys. Lett.* **1964**, 89–90.

[109] Morales, A. M.; Lieber, C. M. *Science* **1998**, *279*, 208–211.

[110] Lu, W.; Lieber, C. M. *J. Phys. D: Appl. Phys.* **2006**, *39*, R387.

[111] Radovanovic, P. V. *Nat. Nanotechnol.* **2009**, *4*, 282–283.

[112] Tutuc, E.; Chu, J. O.; Ott, J. A.; Guha, S. *Appl. Phys. Lett.* **2006**, *89*, 3101.

[113] Stamplecoskie, K. G.; Ju, L.; Farvid, S. S.; Radovanovic, P. V. *Nano Lett.* **2008**, *8*, 2674–2681.

[114] Perea, D. E.; Hemesath, E. R.; Schwalbach, E. J.; Lensch-Falk, J. L.; Voorhees, P. W.; Lauhon, L. J. *Nat. Nanotechnol.* **2009**, *4*, 315–319.

[115] Perea, D. E.; Allen, J. E.; May, S. J.; Wessels, B. W.; Seidman, D. N.; Lauhon, L. J. *Nano Lett.* **2006**, *6*, 181–185.

[116] Perea, D.; Wijaya, E.; Lensch-Falk, J.; Hemesath, E.; Lauhon, L. *J. Solid State Chem.* **2008**, *181*, 1642 – 1649.

[117] Zhang, H.; F. Banfield, J. *J. Mater. Chem.* **1998**, *8*, 2073–2076.

[118] Farvid, S. S.; Dave, N.; Radovanovic, P. V. *Chem. Mater.* **2009**, *22*, 9–11.

[119] Farvid, S. S.; Hegde, M.; Radovanovic, P. V. *Chem. Mater.* **2013**, *25*, 233–244.

[120] Wang, T.; Radovanovic, P. V. *J. Phys. Chem. C* **2010**, *115*, 406–413.

[121] Hamberg, I.; Granqvist, C. G. *J. Appl. Phys.* **1986**, *60*, R123–R160.

[122] Rothenberger, G.; Fitzmaurice, D.; Grätzel, M. *J. Phys. Chem.* **1992**, *96*, 5983–5986.

[123] Wang, T.; Farvid, S. S.; Abulikemu, M.; Radovanovic, P. V. *J. Am. Chem. Soc.* **2010**, *132*, 9250–9252.

[124] Wang, T.; Radovanovic, P. V. *J. Phys. Chem. C* **2011**, *115*, 18473–18478.

[125] Nomura, K.; Ohta, H.; Takagi, A.; Kamiya, T.; Hirano, M.; Hosono, H. *Nature* **2004**, *432*, 488–492.

[126] Shim, Y.-S.; Moon, H. G.; Kim, D. H.; Jang, H. W.; Kang, C.-Y.; Yoon, Y. S.; Yoon, S.-J. *Sensor. Actuat. B-Chem.* **2011**, *160*, 357–363.

[127] Barsan, N.; Koziej, D.; Weimar, U. *Sensor. Actuat. B-Chem.* **2007**, *121*, 18–35.

[128] Grätzel, M. *Inorg. Chem.* **2005**, *44*, 6841–6851.

[129] Geller, S. *J. Chem. Phys.* **1960**, *33*, 676–684.

[130] Tippins, H. H. *Phys. Rev.* **1965**, *140*, A316.

[131] Binet, L.; Gourier, D. *J. Phys. Chem. Solids* **1998**, *59*, 1241 – 1249.

[132] Lorenz, M. R.; Woods, J. F.; Gambino, R. J. *J. Phys. Chem. Solids* **1967**, *28*, 403–404.

[133] Hajnal, Z.; Miró, J.; Kiss, G.; Réti, F.; Deák, P.; Herndon, R. C.; Kuperberg, J. M. *J. Appl. Phys.* **1999**, *86*, 3792–3796.

[134] Song, Y. P.; Zhang, H. Z.; Lin, C.; Zhu, Y. W.; Li, G. H.; Yang, F. H.; Yu, D. P. *Phys. Rev.B* **2004**, *69*, 075304.

[135] Harwig, T.; Kellendonk, F.; Slappendel, S. *J. Phys. Chem. Solids* **1978**, *39*, 675–680.

[136] Vanithakumari, S. C.; Nanda, K. K. *Adv. Mater.* **2009**, *21*, 3581–3584.

[137] Maximenko, S.; Mazeina, L.; Picard, Y.; Freitas Jr, J.; Bermudez, V.; Prokes, S. *Nano Lett* **2009**, *9*, 3245–3251.

[138] Hosein, I. D.; Hegde, M.; Jones, P. D.; Chirmanov, V.; Radovanovic, P. V. *J. Cryst. Growth* **2014**, *396*, 24–32.

[139] Binet, L.; Gourier, D.; Minot, C. *J. Solid State Chem.* **1994**, *113*, 420–433.

[140] Ueda, N.; Hosono, H.; Waseda, R.; Kawazoe, H. *Appl. Phys. Lett.* **1997**, *71*, 933–935.

[141] Zhou, X. T.; Heigl, F.; Ko, J. Y. P.; Murphy, M. W.; Zhou, J. G.; Regier, T.; Blyth, R. I. R.; Sham, T. K. *Phys. Rev. B* **2007**, *75*, 125303.

[142] Hwang, S. O.; Kim, H. S.; Park, S.-H.; Park, J.; Bae, S. Y.; Kim, B.; Park, J. Y.; Lee, G. *J. Phys. Chem. C* **2008**, *112*, 2934–2942.

[143] Deepak, F. L.; Vanitha, P. V.; Govindaraj, A.; Rao, C. N. R. *Chem. Phys. Lett.* **2003**, *374*, 314–318.

[144] Seong, H.-K.; Kim, U.; Kim, M.-H.; Lee, H.-H.; Lee, D.-R.; Kim, J.-Y.; Choi, H.-J. *J. Nanosci. Nanotechnol.* **2009**, *9*, 6772–6776.

[145] Radovanovic, P. V.; Barrelet, C. J.; Gradecak, S.; Qian, F.; Lieber, C. M. *Nano Lett.* **2005**, *5*, 1407–1411.

[146] Bunker, G. *Introduction to XAFS: A Practical Guide to X-ray Absorption Fine Structure Spectroscopy*; Cambridge University Press, 2010.

[147] Attwood, D. *Soft X-ray and Extreme Ultraviolet Radiation: Principles and Applications*; Cambridge University Press, 1999.

[148] Onuki, H.; Saito, N.; Saito, T. *Appl. Phys. Lett.* **1988**, *52*, 173–175.

[149] Bahrdt, J.; Wüstefeld, G. *Phys. Rev. ST Accel. Beams* **2011**, *14*, 040703.

[150] Stöhr, J.; Noguera, C.; Kendelewicz, T. *Phys. Rev. B* **1984**, *30*, 5571.

[151] Erbil, A.; Cargill III, G. S.; Frahm, R.; Boehme, R. F. *Phys. Rev. B* **1988**, *37*, 2450.

[152] Dirac, P. A. M. *The Principles of Quantum Mechanics, Fourth Edition*; Oxford at the Clarendon Press, 1981.

[153] Fermi, E. *Nuclear Physics: A Course Given by Enrico Fermi at the University of Chicago*; University of Chicago Press, 1974.

[154] Cornia, A.; Mannini, M.; Sainctavit, P.; Sessoli, R. *Chem. Soc. Rev.* **2011**, *40*, 3076–3091.

[155] Atkins, P. W.; Friedman, R. S. *Molecular Quantum Mechanics, Third Edition*; Oxford University Press, 1997.

[156] Rehr, J. J.; Albers, R. C. *Rev. Mod. Phys.* **2000**, *72*, 621.

[157] Brouder, C. *J. Phys.: Condens. Matter* **1990**, *2*, 701.

[158] Stöhr, J. *J. Magn. Magn. Mater.* **1999**, *200*, 470–497.

[159] Stöhr, J. *J. Electron Spectrosc. Relat. Phenom.* **1995**, *75*, 253–272.

[160] Thole, B.; Carra, P.; Sette, F.; van der Laan, G. *Phys. Rev. Lett.* **1992**, *68*, 1943.

[161] Carra, P.; Thole, B.; Altarelli, M.; Wang, X. *Phys. Rev. Lett.* **1993**, *70*, 694.

[162] Chen, C. T.; Idzerda, Y. U.; Lin, H.-J.; Smith, N. V.; Meigs, G.; Chaban, E.; Ho, G. H.; Pellegrin, E.; Sette, F. *Phys. Rev. Lett.* **1995**, *75*, 152.

[163] Kilcoyne, A. L. D.; Tyliszczak, T.; Steele, W. F.; Fakra, S.; Hitchcock, P.; Franck, K.; Anderson, E.; Harteneck, B.; Rightor, E. G.; Mitchell, G. E.; Hitchcock, A. P.; Yang, L.; Warwick, T.; Ade, H. *J. Synchrotron Rad.* **2003**, *10*, 125–136.

[164] de Groot, F. M. F.; Fuggle, J. C.; Thole, B. T.; Sawatzky, G. A. *Phys. Rev. B* **1990**, *41*, 928.

[165] de Groot, F. M. F. *Coord. Chem. Rev.* **2005**, *249*, 31–63.

[166] de Groot, F. M. F.; Fuggle, J. C.; Thole, B. T.; Sawatzky, G. A. *Phys. Rev. B* **1990**, *42*, 5459.

[167] de Groot, F. M. F. *J. Electron Spectrosc. Relat. Phenom.* **1994**, *67*, 529–622.

[168] Garvie, L. A. J.; Craven, A. J. *Phys. Chem. Miner.* **1994**, *21*, 191–206.

[169] Stavitski, E.; de Groot, F. M. F. *Micron* **2010**, *41*, 687–694.

[170] Hwang, J. I.; Osafune, Y.; Kobayashi, M.; Ebata, K.; Ooki, Y.; Ishida, Y.; Fujimori, A.; Takeda, Y.; Okane, T.; Saitoh, Y.; Kobayashi, K.; Tanaka, A. *J. Appl. Phys.* **2007**, *101*, 103709.

[171] Joly, Y. *Phys. Rev. B* **2001**, *63*, 125120.

[172] Natoli, C. R.; Benfatto, M.; Doniach, S. *Phys. Rev. A* **1986**, *34*, 4682.

[173] Joly, Y. FDMNES User's Guide: Institut Neel, Grenoble. 2011; p 45.

[174] Kaminski, M.; Podsiadlo, S.; Wozniak, K.; Dobrzycki, L.; Jakiela, R.; Barcz, A.; Psoda, M.; Mizera, J. *J. Cryst. Growth* **2007**, *303*, 395–399.

[175] Radovanovic, P. V.; Stamplecoskie, K. G.; Pautler, B. G. *J. Am. Chem. Soc.* **2007**, *129*, 10980–10981.

[176] Chiou, J. W.; Jan, J. C.; Tsai, H. M.; Pong, W. F.; Tsai, M.-H.; Hong, I.-H.; Klauser, R.; Lee, J. F.; Hsu, C. W.; Lin, H. M.; Chen, C. C.; Shen, C. H.; Chen, L. C.; Chen, K. H. *Appl. Phys. Lett.* **2003**, *82*, 3949–3951.

[177] Chiou, J. W.; Mookerjee, S.; Rao, K. V. R.; Jan, J. C.; Tsai, H. M.; Asokan, K.; Pong, W. F.; Chien, F. Z.; Tsai, M. H.; Chang, Y. K.; Chen, Y. Y.; Lee, J. F.; Lee, C. C.; Chi, G. C. *Appl. Phys. Lett.* **2002**,

[178] Lawniczak-Jablonska, K.; Suski, T.; Gorczyca, I.; Christensen, N. E.; Attenkofer, K. E.; Perera, R. C. C.; Gullikson, E. M.; Underwood, J. H.; Ederer, D. L.; Weber, Z. L. *Phys. Rev. B* **2000**, *61*, 16623.

[179] Lawniczak-Jablonska, K.; Suski, T.; Liliental-Weber, Z.; Gullikson, E. M.; Underwood, J. H.; Perera, R. C. C.; Drummond, T. J. *Appl. Phys. Lett.* **1997**, *70*, 2711–2713.

[180] Lawniczak-Jablonska, K.; Iwanowski, R. J.; Demchenko, I. N.; Boettcher, T.; Einfeldt, S.; Hommel, D.; Cortes, R.; Perera, R. C. C. *J. Alloys Compd.* **2001**, *328*, 77–83.

[181] Bacewicz, R.; Filipowicz, J.; Podsiadło, S.; Szyszko, T.; Kamiński, M. *J. Phys. Chem. Solids* **2003**, *64*, 1469–1472.

[182] Keavney, D. J.; Cheung, S. H.; King, S. T.; Weinert, M.; Li, L. *Phys. Rev. Lett.* **2005**, *95*, 257201.

[183] Hwang, J. I.; Kobayashi, M.; Song, G. S.; Fujimori, A.; Tanaka, A.; Yang, Z. S.; Lin, H. J.; Huang, D. J.; Chen, C. T.; Jeon, H. C.; Kang, T. W. *Appl. Phys. Lett.* **2007**, *91*, –.

[184] Hegde, M.; Farvid, S. S.; Hosein, I. D.; Radovanovic, P. V. *ACS Nano* **2011**, *5*, 6365–6373.

[185] Matsukura, F.; Ohno, H.; Dietl, T. In *Handbook of Magnetic Materials*; Buschow, K. H. J., Ed.; Elsevier, Amsterdam, 2002; pp 1–87.

[186] Hegde, M.; Hosein, I. D.; Sabergharesou, T.; Farvid, S. S.; Radovanovic, P. V. Introducing and manipulating magnetic dopant exchange interactions in semiconductor nanowires. SPIE NanoScience+ Engineering. 2013; pp 88132S–88132S.

[187] Farvid, S. S.; Hegde, M.; Hosein, I. D.; Radovanovic, P. V. *Appl. Phys. Lett.* **2011**, *99*, 222504.

[188] Stroppa, A.; Kresse, G. *Phys. Rev. B* **2009**, *79*, 201201.

[189] Stefanowicz, W.; Sztenkiel, D.; Faina, B.; Grois, A.; Rovezzi, M.; Devillers, T.; dAcapito, F.; Navarro-Quezada, A.; Li, T.; Jakieła, R.; Sawicki, M.; Dietl, T.; Bonanni, A. *Phys. Rev. B* **2010**, *81*, 235210.

[190] Smolentsev, N.; Smolentsev, G.; Wei, S.; Soldatov, A. V. *Physica B: Condensed Matter* **2011**, *406*, 2843–2846.

[191] Goering, E. *Philos. Mag.* **2005**, *85*, 2895–2911.

[192] Feng, Y.; Badaeva, E.; Gamelin, D. R.; Li, X. *J. Phys. Chem. Lett.* **2010**, *1*, 1927–1931.

[193] McCurrie, R. A. *Ferromagnetic Materials : Structure and Properties*; Academic Press: London, 1994.

[194] Henry, Y.; Ounadjela, K.; Piraux, L.; Dubois, S.; George, J.-M.; Duvail, J.-L. *Eur. Phys. J. B* **2001**, *20*, 35–54.

[195] Krebs, O.; Benjamin, E.; Lemaitre, A. *Phys. Rev. B* **2009**, *80*, 165315.

[196] Liang, D.; Sakr, M. R.; Gao, X. P. A. *Nano Lett.* **2009**, *9*, 1709–1712.

[197] Lehnen, P.; Schäpers, T.; Kaluza, N.; Thillosen, N.; Hardtdegen, H. *Phys. Rev. B* **2007**, *76*, 205307.

[198] Yoshioka, S.; Hayashi, H.; Kuwabara, A.; Oba, F.; Matsunaga, K.; Tanaka, I. *J. Phys.: Condens. Matter* **2007**, *19*, 346211.

[199] Martin, M.; Dronskowski, R.; Janek, J.; Becker, K.-D.; Roehrens, D.; Brendt, J.; Lumey, M. W.; Nagarajan, L.; Valov, I.; Börger, A. *Prog. Solid State Chem.* **2009**, *37*, 132–152.

[200] Yamaga, M.; Víllora, E. G.; Shimamura, K.; Ichinose, N.; Honda, M. *Phys. Rev. B* **2003**, *68*, 155207.

[201] Kumar, S.; Tessarek, C.; Christiansen, S.; Singh, R. *J. Alloys Compd.* **2014**, *587*, 812–818.

[202] Kumar, S.; Kumar, V.; Singh, T.; Hähnel, A.; Singh, R. *J. Nanopart. Res.* **2014**, *16*, 1–9.

[203] Wang, G.; Park, J.; Kong, X.; Wilson, P. R.; Chen, Z.; Ahn, J.-h. *Cryst. Growth Des.* **2008**, *8*, 1940–1944.

[204] Cao, G. *Nanostructures and Nanomaterials: Synthesis, Properties and Applications*; Imperial College Press, London, 2004.

[205] Hartman, P. *Nanostructures and Nanomaterials: Synthesis, Properties and Applications*; Amsterdam, North Holland, 1973.

[206] Hartman, P. *Geol. Mijnbouw.* **1982**, *61*, 313–320.

[207] Hartman, P.; Heijnen, W. M. M.; Woensdregt, C. F. *Fortschr. Mineral.* **1983**, *61*, 79–80.

[208] Mullins, W. W. *Metal Surfaces: Structure, Energetics and Kinetics*; The American Society of Metals, Metals Park, OH, 1962.

[209] Bermudez, V. *Chem. Phys.* **2006**, *323*, 193–203.

[210] Weller, D.; Stöhr, J.; Nakajima, R.; Carl, A.; Samant, M. G.; Chappert, C.; Mégy, R.; Beauvillain, P.; Veillet, P.; Held, G. A. *Phys. Rev. Lett.* **1995**, *75*, 3752.

[211] Demchenko, I. N.; Chernyshova, M.; Piskorska-Hommel, E.; Minikayev, R.; Domagala, J. Z.; Yamaguchi, T.; Stolte, W. C.; Lawniczak-Jablonska, K. *J. Alloys Compd.* **2011**, *509*, 9528–9535.

[212] Mizoguchi, T.; Tanaka, I.; Yoshioka, S.; Kunisu, M.; Yamamoto, T.; Ching, W. Y. *Phys. Rev. B* **2004**, *70*, 045103.

[213] Demchenko, I. N.; Denlinger, J. D.; Chernyshova, M.; Yu, K. M.; Speaks, D.; Olalde-Velasco, P.; Hemmers, O.; Walukiewicz, W.; Derkachova, A.; Lawniczak-Jablonska, K. *Phys. Rev. B* **2010**, *82*, 075107.

[214] Bunău, O.; Joly, Y. *J. Phys.: Condens. Matter* **2009**, *21*, 345501.

[215] He, H.; Blanco, M. A.; Pandey, R. *Appl. Phys. Lett.* **2006**, *88*, 261904.

[216] Hegde, M.; Hosein, I. D.; Radovanovic, P. V. *J. Phys. Chem. C* **2015**,

[217] Albanesi, E. A.; Sferco, S. J.; Lefebvre, I.; Allan, G.; Hollinger, G. *Phys. Rev. B* **1992**, *46*, 13260.

[218] Stöhr, J. *NEXAFS Spectroscopy*; Springer-Verlag: Berlin, 1996.

[219] Pedio, M.; Fuggle, J.; Somers, J.; Umbach, E.; Haase, J.; Lindner, T.; Höfer, U.; Grioni, M.; de Groot, F. M. F.; Hillert, B.; Robinson, A. *Phys. Rev. B* **1989**, *40*, 7924.

[220] Oszwałdowski, R.; Žutić, I.; Petukhov, A. G. *Phys. Rev. Lett* **2011**, *106*, 177201.

[221] Yang, Y.; Zhao, Q.; Zhang, X. Z.; Liu, Z. G.; Zou, C. X.; Shen, B.; Yu, D. P. *Appl. Phys. Lett.* **2007**, *90*, 092118.

[222] Whang, D.; Jin, S.; Wu, Y.; Lieber, C. M. *Nano Lett.* **2003**, *3*, 1255–1259.

[223] Melosh, N. A.; Boukai, A.; Diana, F.; Gerardot, B.; Badolato, A.; Petroff, P. M.; Heath, J. R. *Science* **2003**, *300*, 112–115.

[224] Ashcroft, N. W.; Mermin, N. D. *Solid State Physics*; Saunders College, 1976.

[225] Ju, L.; Sabergharesou, T.; Stamplecoskie, K. G.; Hegde, M.; Wang, T.; Combe, N. A.; Wu, H.; Radovanovic, P. V. *J. Am. Chem. Soc.* **2011**, *134*, 1136–1146.

[226] Hegde, M.; Wang, T.; Miskovic, Z. L.; Radovanovic, P. V. *Appl. Phys. Lett.* **2012**, *100*, 141903.

[227] Farvid, S. S.; Sabergharesou, T.; Hutfluss, L. N.; Hegde, M.; Prouzet, E.; Radovanovic, P. V. *J. Am. Chem. Soc.* **2014**, *136*, 7669–7679.

[228] Layek, A.; Yildirim, B.; Ghodsi, V.; Hutfluss, L. N.; Hegde, M.; Wang, T.; Radovanovic, P. V. *Chem. Mater.* **2015**,